ELSEVIER

Computational aeroacoustics: progress on nonlinear problems of sound generation

Tim Colonius[a,*], Sanjiva K. Lele[b]

[a]*Department of Mechanical Engineering, California Institute of Technology, Mail Code 104-44 Pasadena, CA 91125, USA*
[b]*Department of Aeronautics and Astronautics and Department of Mechanical Engineering, Stanford University, Stanford, CA 94305-4035, USA*

Abstract

Computational approaches are being developed to study a range of problems in aeroacoustics. These aeroacoustic problems may be classified based on the physical processes responsible for the sound radiation, and range from linear problems of radiation, refraction, and scattering in known base flows or by solid bodies, to sound generation by turbulence. In this article, we focus mainly on the challenges and successes associated with numerically simulating sound generation by turbulent flows.

We discuss a hierarchy of computational approaches that range from semi-empirical schemes that estimate the noise sources using mean-flow and turbulence statistics, to high-fidelity unsteady flow simulations that resolve the sound generation process by direct application of the fundamental conservation principles. We stress that high-fidelity methods such as Direct Numerical Simulation (DNS) and Large Eddy Simulation (LES) have their merits in helping to unravel the flow physics and the mechanisms of sound generation. They also provide rich databases for modeling activities that will ultimately be needed to improve existing predictive capabilities.

Spatial and temporal discretization schemes that are well-suited for aeroacoustic calculations are analyzed, including the effects of artificial dispersion and dissipation on uniform and nonuniform grids. We stress the importance of the resolving power of the discretization as well as computational efficiency of the overall scheme. Boundary conditions to treat the flow of disturbances in and out of the computational domain, as well as methods to mimic anechoic domain extension are discussed. Test cases on some benchmark problems are included to provide a realistic assessment of several boundary condition treatments.

Finally, highlights of recent progress are given using selected model problems. These include subsonic cavity noise and jet noise. In the end, the current challenges in aeroacoustic modeling and in simulation algorithms are revisited with a look toward the future developments.
© 2004 Elsevier Ltd. All rights reserved.

*Corresponding author. Tel.: +1 626 395 4021; fax: +1 626 568 2719.
E-mail address: colonius@caltech.edu (T. Colonius).

Nomenclature

Roman characters

A	amplitude function
a	finite-difference coefficients, Section 4.1
a	speed of sound
C	airfoil chord
c	wave speed
c_g	group velocity
c_p	phase speed
C_p, C_s, C_T	LES model coefficients
D	(jet) diameter
E	three-dimensional energy spectrum
E_1	total energy density
f	frequency
h	grid spacing
K	modified wavenumber
k	wavenumber
L	turbulence integral scale
M	Mach number
m_i	subgrid mass flux vector
n	order of accuracy
p	pressure
q_i	heat flux vector
r_{ij}	subgrid momentum flux tensor
Re	Reynolds number
S_{ij}	symmetric strain rate tensor
St	Strouhal number
T	temperature
T_{ij}	Lighthill stress tensor
U	velocity (usually reference value)
u	velocity
U_c	convective velocity
w	window function
$\mathbf{q}$	vector of dependent variables
q_{si}	subgrid energy flux vector

Greek characters

α	finite-difference coefficients, Section 4.1
α	shear layer spreading rate
α_j	apparent velocity, Section 4.1
Δ	LES filter width, or difference
δ	shock thickness
$\delta^\star$	displacement thickness
δ_ω	vorticity thickness
ε	turbulence dissipation
η	Kolmogorov scale
γ	ratio of specific heats
λ_1	Taylor microscale
μ	viscosity
ρ	density
σ	damping coefficient

τ	eddy turnover time
τ_{ij}	viscous stress tensor
θ	momentum thickness
θ	phase function, Section 4.1

Subscripts

∞	free-stream or far-field value
c	centerline
j	jet value at nozzle lip
p	peak
t	turbulent

Superscripts and constructs

$\langle()\rangle$	ensemble or time averaged
$\overline{()}$	LES filtered
$\widehat{()}$	LES test-filtered or Fourier transformed
$\check{()}$	windowed
$'$	fluctuating quantity or derivative

Abbreviations

BC	boundary condition
CAA	computational aeroacoustics
CFD	computational fluid dynamics
CFL	Courant–Friedrichs–Levy
DNS	direct numerical simulation
DRP	dispersion-relation-preserving
ENO	essentially non-oscillatory
FCT	flux-corrected transport
FD	finite difference
Ff–H	Ffowcs Williams–Hawkings
IC	initial condition
LDD	low dissipation and dispersion
LEE	Linearized Euler equations
LES	large eddy simulation
LM	linear multi-step
NPSE	nonlinear Parabolized Stability equations
OASPL	overall sound pressure level
PML	perfectly matched layer
PSE	Parabolized Stability equations
RANS	Reynolds-averaged Navier–Stokes
RK	Runge–Kutta
SAT	simultaneous approximation term
SBP	summation-by-parts
SGS	sub-grid stress
SPL	sound pressure level
TKE	turbulent kinetic energy
TVD	total variation diminishing
URANS	unsteady Reynolds-averaged Navier–Stokes
WENO	weighted essentially non-oscillatory

Contents

1. Introduction

The aerodynamic noise of airplanes at take-off and in the landing configuration continues to be a critical factor in the future development of aviation. Community noise concerns at busy airports constrain the design of new airplanes, subsonic or supersonic, and of rotorcraft. The current operational fleet is also subject to new increasingly stringent noise regulations. Aviation technology with dramatically lower community noise footprint, for example one that limits the noise footprint to the airport perimeter, is envisioned in NASA's ambitious long term plan for the next 20 years. Such long term targets and specific near-term noise reduction goals are driving active research in aeroacoustics. As an example, jet noise has traditionally been reduced by increasing the bypass ratio of turbofan engines. However, this trend cannot be continued indefinitely without significant changes to the traditional airframe configuration and engine cycles, and more subtle technologies, such as serrated nozzles or tabs, are being considered. These modifications are for the most part outside of the design space for which noise can be effectively predicted, and new theoretical and computational approaches are therefore needed if optimal designs are to be found.

Even for the "terrifyingly loud" noises, such as those from early turbo-jets with a noise level of (say) 114 dB at the sideline point of certification, the radiated pressure fluctuation is less than 10^{-4} of the ambient pressure. Typical aviation noises are considerably weaker, thus the radiated sound field is typically linear. A significant exception is the sonic boom of a supersonic airplane or of supersonically moving turbulent eddies. However, the flows that generate the undesired noise are usually nonlinear, unsteady and turbulent. Typically the unsteady flow region contains significant vortical, eddying motions that also have associated near-field pressure disturbances. The radiated noise is far smaller than these near-field pressure fluctuations. The radiation from slowly changing turbulence is typically inefficient, but sharp geometrical changes, or other rapid variations in boundary conditions, flow properties or structural properties can result in a transfer of disturbance energy from the otherwise non-radiating convected modes to those that radiate. This type of generalized scattering is often the physical phenomena responsible for noise radiation.

Since the flows that are ultimately responsible for the unwanted noise are usually complex it is necessary to make some pragmatic simplification. The first step is a classification of the problem according to the dominant mechanism of sound generation. Such a classification is presented in Section 2. The next step is a careful synthesis of a computational problem that incorporates the required details of the sound generation process. In a general flow it is not possible to unambiguously separate the 'flow' from the 'sound'. However, when the flow Mach number is small it is advantageous to separate the task of predicting the unsteady vortical motion, i.e. *flow* prediction, from that of *noise* prediction. To help gain a perspective on this issue two specific model problems of trailing-edge noise and jet-noise are presented in Section 2.3.

Predicting the noise radiation associated with unsteady flows is the central theme of aeroacoustics. A variety of approaches are available which use flow data to estimate the radiated noise. The unsteady flow can be represented at different levels of detail or idealization. Different noise prediction approaches taken together with flow representations at different fidelity define a hierarchy of noise prediction methods. These are discussed in Section 3.

Once the computational problem to be addressed has been elucidated in this way, accurate numerical solution techniques can be developed. In problems of nonlinear sound generation, there is significant overlap with techniques used generally for Direct Numerical Simulation (DNS) and Large Eddy Simulation (LES) of turbulent flow, since the flow is governed by the unsteady compressible Navier–Stokes equations. For propagation problems, there is overlap with numerical methods used in (linear) acoustics. In developing numerical methods for sound generation and propagation problems, it is natural to try to adapt methods used generally in CFD. To reliably do so, however, we must first examine those characteristics of sound generation and propagation problems that are likely to pose a challenge to traditional methods:

1. The generation of acoustic waves by fluid motion is, by its nature, an unsteady process; steady flows generate no sound. Turbulence modeling, leading to RANS, unsteady RANS, and LES, filters small spatial and high frequency fluctuations from the solution; the impact of such filtering on sound generation has not yet been characterized in any systematic way. Most computational results for sound generation, therefore, have used DNS, where

all relevant scales of motion are resolved. Use of LES for aeroacoustics is under active development.

2. Acoustic waves may propagate coherently, with very low attenuation due to viscous effects, over long distances in the flow. Artificial dissipation and dispersion at a level that may be tolerable for hydrodynamic fluctuations can lead to unacceptable attenuation of acoustic waves.

3. As previously mentioned, even loud flows radiate a very small fraction of their total energy as sound. That is, acoustic (radiation) efficiency is invariably very low. At low Mach number, acoustic inefficiency can be viewed as the result of a delicate cancellation process of equal but nearly opposite sources (e.g. dipole, quadrupole, etc.). Numerical errors that may upset this delicate balance can therefore lead to serious overestimates of sound generation. This issue was recognized early on by Crighton [1]. For example, truncation of a computational domain with artificial boundary conditions is a primary cause of such errors.

As will be discussed in Section 4, one route to efficient and accurate solution to these difficulties is the use of high-order and optimized finite difference (FD) schemes. It should be kept in mind that even with high-order (or indeed spectral) methods, LES and DNS at low to moderate Reynolds numbers requires large numbers of computational nodes (10^6 and up). Furthermore, it is surprisingly difficult to maintain high accuracy and computational efficiency for flows in complex geometry (i.e. with unstructured or overlapping body-fitted coordinates). Thus complex geometry codes can only obtain good accuracy by increasing the resolution (hopefully adaptively). Complex geometry calculations are then typically limited to either linearized flow or unsteady RANS calculations, such that the computational resources required are not too large. These do not provide an unambiguous estimate of the sound sources or the radiated field, and engineering judgment must then dictate how useful data can be extracted for a given problem. In either case (DNS or modeled equations), one must proceed cautiously, always keeping in mind errors and uncertainties associated with the results.

In Section 5 we review some recent progress in nonlinear simulations of sound generation. The aim is to show how computational approaches can provide a database through which models of the sound sources can be tested, provide physical insight on the mechanisms of sound generation by turbulence, and, optimistically, provide a means to develop strategies for open- and closed-loop control of acoustic radiation. The paper ends by recalling the physical and numerical challenges that lie ahead if such goals are to be met.

2. Classification of aeroacoustic problems

Diverse problems of aeroacoustics can be classified on the basis of the physical phenomena that are expected to play a central role. Specialized solution methods are available for particular problem types. The main classification is between the *linear* and *nonlinear* problems, each of which can be subdivided into several groups. An important issue here is the *basic state* about which the flow is linearized. A careful choice of the basic state allows for wider possibilities within the so-called grouping of *linear* problems of aeroacoustics. Some examples are included but without any attempt to review the specific sub-fields. The noise from a physical system may involve a combination of multiple sub-problems from the categories below.

2.1. Linear problems of propagation and generalized scattering

This includes the classical boundary value problems of linear acoustics, sound propagation in a uniform media in presence of reflecting surfaces, barriers, absorbing walls, and ducts, and also the propagation and scattering of sound in a prescribed non-uniform medium. Specific examples include radiation from a duct opening or engine-inlet due to a specified source or a specified duct-mode disturbance, and radiation from a specified source across a finite barrier/sound-wall with an absorbing treatment. Sound propagation in a specified non-uniform time-dependent medium including refraction/scattering in steady and unsteady vortical flows, sound propagation in ducts with non-uniform flows including the interaction with geometrical changes, liner impedance[1] and mean-flow variations are considered as linear problems of scattering. Additionally problems involving scattering of non-acoustic disturbances into sound such as scattering of a vortical disturbance into sound (at leading/trailing edges), scattering of entropic disturbance into sound (in a nozzle or at a shock), modal scattering in a turbomachinery blade row, and scattering of structural vibration into sound are also included as *generalized* scattering.

2.2. Nonlinear problems of flow acoustics or aeroacoustics

This includes problems of nonlinear propagation, such as nonlinear steepening and decay, focusing, viscous effects in intense sound beams (acoustic near field of high-speed jets), and sonic boom propagation

---

[1] The detailed physics of acoustic damping due to a liner, i.e. vortex shedding or turbulence generation in response to the incident sound is non-linear. Its approximate representation as an impedance boundary condition is linear.

through atmospheric turbulence, sound propagation in complex fluids and multi-phase systems (such as in lithotripsy), and internal flows of thermo-acoustic cooling systems. Also included in this category are problems of scattering of nonlinear disturbances into sound, such as airframe noise (slat noise, flap side-edge noise) and rotorcraft noise (blade–vortex interaction, high-speed impulsive noise). Nonlinear problems of sound generation include noise from transition and turbulence in boundary layers, noise from separated boundary layers and massive flow separation (i.e. landing gear noise), turbulent jet mixing noise, noise from instability wave-packets, noise of internal forced mixing (e.g. for lobed mixers), noise from flow obstructions, broadband fan noise, and self-noise from blading. Yet another subcategory here involves acoustic-induced instabilities and resonances, such as jet screech, cavity and edge tones, and combustion instabilities.

2.3. Illustrative examples

We consider two examples that illustrate the physical and computational issues that must be considered in order to develop tractable computational models. These specific illustrations also motivate the need for a hierarchy of CAA simulation methods. Approximate models of the unsteady flow at various levels of flow detail are combined with different methodologies for obtaining the far-field noise in such a hierarchy. These are outlined in Section 3.

2.3.1. Airfoil/hydrofoil trailing-edge noise at low speed

The importance of the noise originating from the interaction of unsteady disturbances with leading- and trailing-edges of a wing, fan and compressor blades is well recognized [2,3]. This physical problem has motivated numerous studies of idealized model problems in unsteady aerodynamics dating back to the work by Theodorsen, Kussner, von Karman, and Sears; these early studies were motivated by forced-vibration problems. In hydroacoustics, the noise from turbulence passing over the trailing edge of a hydrofoil is of particular interest [4]. Recently Wang and Moin [5] have carefully developed LES of turbulent flow over a hydrofoil and its acoustic radiation. Other groups have also developed CAA methods in the context of airframe noise of a landing configuration [6–8]. A physical discussion the noise generation in the context of turbomachinery flows is given by Kerschen and collaborators [9,10] who emphasize analytical methods. A review of the different analytical approaches is given by Howe [11,12].

The schematic in Fig. 1 shows the different length scales associated with an unsteady flow over a low speed airfoil. The airfoil chord is C, its maximum thickness is
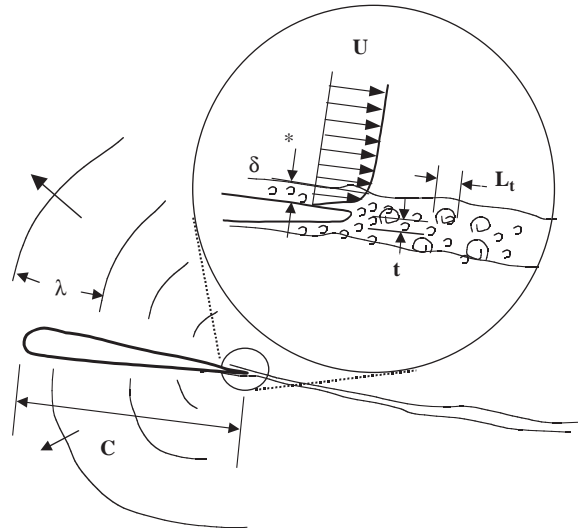

Fig. 1. A schematic of the broadband trailing-edge scattering problem.

h, and the boundary layer displacement thickness near the trailing-edge is $\delta_t^\star$. Some estimates based on the experimental data, for example Brooks and Hodgson [13], allow an appreciation of the relative magnitudes. In this experiment the trailing-edge noise from a NACA 0012 airfoil was measured. The airfoil chord $C = 0.61$ m, and a wind tunnel speed U_∞ up to 62 m/s giving $M_\infty \approx 0.2$ were used. At the highest flow speed the chord based Reynolds number is about 3×10^6. The boundary layers were tripped, near $x/C = 0.15$, to achieve a spanwise-uniform development of the turbulent boundary layers. At the trailing edge $\delta_t^\star \approx 0.3$ cm. or $Re_{\delta\star} \approx 2 \times 10^4$. The same airfoil with blunted trailing-edges with bluntness $t/\delta^\star$ ranging over 0–0.6 were also tested. Blunt edges were found to radiate an additional *vortex-shedding* noise. Since the frequency f (in Hz) of the energetic fluctuations in the boundary layer approaching the trailing-edge scale as $f\delta^\star/U_\infty \sim 0.06 - 0.08$, the trailing-edge noise peaks in this range. However the broad range of temporal frequencies in the boundary layer gives rise to broadband radiated noise; the noise spectrum decays only slowly for frequencies higher than the peak.

The acoustic wavelength corresponding to the peak noise scales as $\lambda_p/C \sim \alpha\frac{\delta^\star/C}{M_\infty}$, with the constant α in the range 13–18. For the highest speed condition in [13] this gives λ_p/C in the range 0.4–0.6. Evidently, for the peak of the trailing-edge noise the airfoil represents an acoustically non-compact body. In hydroacoustic problems at lower M_∞, the noise peak occurs at $\lambda_p/C > 1$ but higher frequencies correspond to a non-compact body. In turbomachinery flows M_∞ is larger and non-compactness is the norm. As explained by Wang and

Moin [5], the noise radiation problem sketched in Fig. 1 involves frequency ranges with very different physics. At low frequencies the acoustic wavelength is much larger than the body size, i.e. $\lambda \gg C$, and the airfoil is acoustically compact. At intermediate frequencies with $\lambda/C \sim O(1)$, there is significant interaction between the scattering from the leading- and trailing-edges. Finally, at higher frequencies with $\lambda \ll C$, leading- and trailing-edge scattering are relatively independent. The noise prediction method can be made more efficient by exploiting the physics relevant to the specific regime.

The energetic turbulent fluctuations in the boundary layer approaching the trailing-edge and in its near-wake, which contribute to the peak noise radiation are of small spatial scale relative to the airfoil chord or its maximum thickness (Fig. 1). The spatial wavenumber of turbulence, $k_t = 2\pi/L_t$, is approximately related to the frequency $\omega = k_t U_c$, where the convection-velocity U_c scales with the hydrodynamic variables. Thus at low Mach numbers, $\lambda/L_t \sim 1/M_c$, which gives an extreme spatial contrast between the hydrodynamic and acoustic length scales. It is quite impractical to directly capture both scales in a low Mach number unsteady flow. Wang and Moin devise an attractive strategy to overcome this difficulty. The radiated noise is treated as a small by-product of the flow that is not altered by it. This assumption is central to Lighthill's formulation of aerodynamic sound generation and is used by Wang and Moin to relate the flow unsteadiness to the radiated noise. This is an example of a hybrid approach to noise prediction. The dynamics of unsteady turbulent disturbances in the noise-producing region is simulated assuming that the flow is strictly incompressible. Fig. 2 illustrates the instantaneous and mean flow near the trailing-edge computed using LES. Fig. 3 shows that the predicted flow (and turbulence not shown here) are in
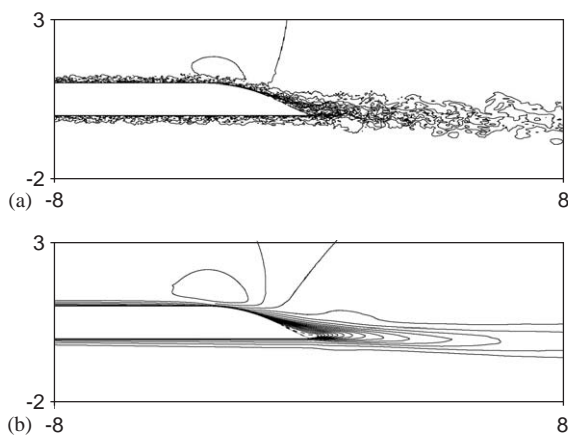

Fig. 3. Mean velocity profiles $\overline{U/U_\infty}$ computed with LES by Wang and Moin (2000). Solid line: LES results; Symbols: Experimental data of Blake.
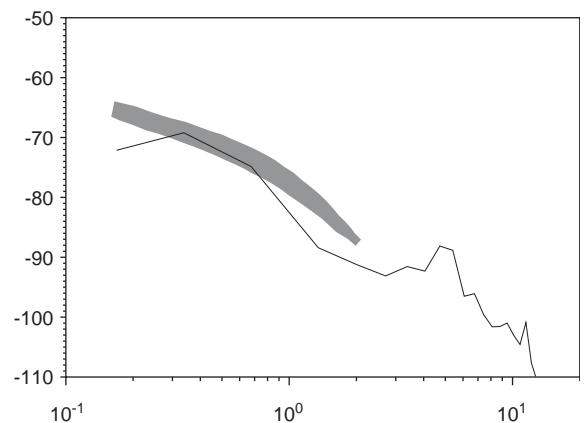
Fig. 4. Normalized spectrum of the radiated noise predicted using LES-acoustic analogy hybrid by Wang and Moin (2000). The normalization is given in [5]. Solid curve: Noise prediction; Shaded area: Experimental data of Blake.

good agreement with the experimental data. The noise radiation is then based on *post-processing* of the flow data. This post-processing uses Lighthill's form of *noise source-terms* and a Green's function well suited for the trailing-edge radiation [14]. An example of the predicted noise spectra is shown in Fig. 4. Different methodologies can be used for simulating the unsteady flow (in the noise producing region), and a variety of *post-processing* methodologies are available. Different combinations provide various hybrid noise prediction methods. They are discussed more completely in Section 3. The reader may recall that trailing-edge scattering was classified above as a nonlinear problem. While scattering small amplitude non-acoustic disturbances into sound at the trailing-edge (i.e. the sudden change in the boundary condition), is a linear process, the vortical flow disturbance environment (turbulence) near the trailing-edge is itself nonlinear. The implied split into the vortical

Fig. 2. Velocity fields computed using LES by Wang and Moin (2000). (a) Instantaneous streamwise velocity u_1/U_∞ at a given spanwise station, (b) Mean streamwise velocity U_1/U_∞.
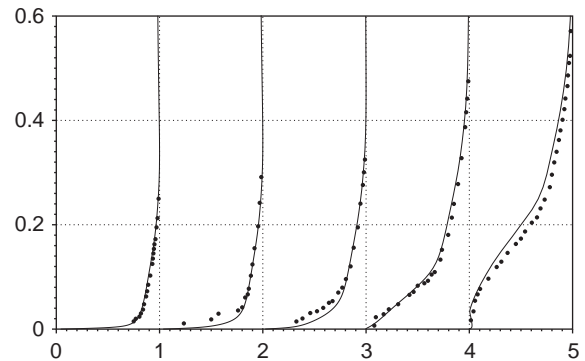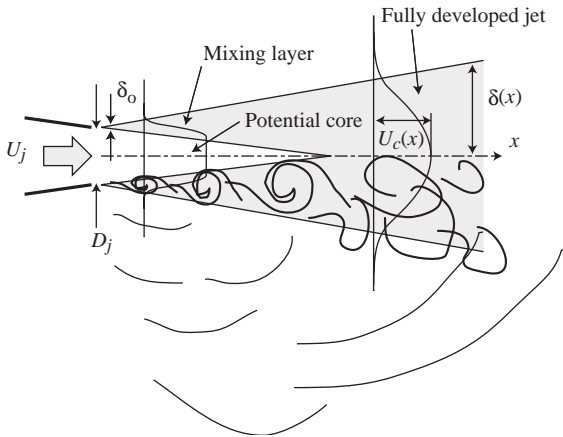
Fig. 5. Schematic of a turbulent jet.

flow disturbances and the sound is not always unambiguous, specially in higher speed flows, and represents a conceptual barrier for a comprehensive theory of aerodynamic sound generation.

2.3.2. High speed jet noise

Consider a high-speed jet at a moderate to high Reynolds number, see the schematic in Fig. 5. The jet exit diameter is D_j, jet exit velocity U_j, jet density ρ_j (speed of sound a_j). The ambient density and speed of sound are ρ_∞, and a_∞, respectively. It is assumed that the nozzle boundary layers are thin, i.e. their momentum thickness $\theta/D_j \ll 1$. The overall jet flow is insensitive to the jet Reynolds number $Re_j = \rho_j U_j D_j / \mu_j$ for high Re_j; the mean velocity profiles, Reynolds stress distributions, potential-core length etc. are not significantly affected by Re_j. The jet speed U_j, on the other hand does affect the jet flow and its noise: as the jet Mach number $M_j = U_j/a_j$ increases the potential core gets extended due to a reduced shear-layer spreading. The spectra of the radiated noise also change with M_j. For the latter the acoustic Mach number of the jet $M = U_j/a_\infty$, and the temperature ratio T_j/T_∞ are more appropriate. Tam [15] has provided a recent review of jet noise, specially for supersonic jets.

As shown in the figure four distinct regions exist in a jet flow. Immediately downstream of the nozzle the jet turbulence is confined to the annular shear layer or mixing layer which surrounds the potential core. The inward spreading of the mixing layer terminates the potential core and the jet centerline velocity falls downstream of this point. This marks an intermediate region of the jet development towards a self-similar far-field jet flow. This intermediate or transition region from a mixing layer towards the self-similar jet is often regarded as the region of the dominant noise generation. The flow properties in the mixing layer and self-similar jet regions are discussed in turn.

The flow downstream from the nozzle trailing-edge rapidly forms a mixing layer; the boundary-layer flow profiles change to that of a mixing-layer. If the initial boundary layers (at nozzle exit) are laminar, as is the case in some experiments using a high contraction-ratio nozzle, the early shear layer shows the classic Kelvin–Helmholtz instability. The width of the turbulent mixing layer, e.g. the vorticity thickness $\delta_\omega(x)$, grows as $\delta_\omega(x) \approx \alpha(x - x_0)$ and the velocity difference across the mixing layer stays constant. For this mixing region[2] $\alpha = \alpha_0 \frac{2(U_1 - U_2)}{U_1 + U_2}$ with α_0 in the range 0.08 [16,17] to 0.098 [18], U_1 and U_2 are the *free-stream* speeds of the high- and low-speed streams, respectively. For a jet in absence of any co-flow, $U_1 = U_j$ and $U_2 = 0$ yields $\alpha = 0.18$. In the mixing layer the turbulent velocity fluctuations scale with $U_1 - U_2$ or U_j, and the local turbulence integral scale grows as $L(x) = 0.7\delta_\omega(x)$, e.g. the spatial correlation measurement in Davies et al. [19]. The local velocity scale for turbulence is taken as $u_0(x) = 0.17U_j$ [20,21].

After the potential core of the jet ends the velocity at the centerline decays and the jet turbulence evolves to yield a *self-similar* far-jet. Experiments show that the half-width of the jet (based on the mean velocity falling to 0.5 of the centerline velocity $U_c(x)$) is given by $\frac{\delta_{1/2}}{D_j} \approx A(x - x_0)/D_j$ and $U_c(x)/U_j \approx \frac{B}{(x - x_0)/D_j}$, where the constants A ranges over (0.086–0.096) and B ranges over (5.4–6.1) (see compilations in [22,23]). We will take $A = 0.095$ and $B = 5.5$, along with $L(x) = 1.4\delta_{1/2}(x)$ and $u_0(x) = 0.25U_c(x)$ to make estimates for $(x - x_0)/D_j \geqslant 6$. The *virtual origin* of the jet, x_0, is known to depend on the conditions at the nozzle exit; a nearly laminar boundary layer has the effect of shifting the location where the potential core ends, while a thick turbulent boundary layer at nozzle exit shifts this upstream. We assume that the potential core ends at $x/D_j = 5.5$ as in [24], and $x_0/D_j = 4$ as in [25]. The choice of $L(x) = 1.4\delta_{1/2}(x)$ for the jet gives the same value of $L(x)$ at $x/D_j = 5.5$ (the end of the potential core) as obtained with the mixing layer length-scale estimate [19].

As a specific example consider a laboratory-scale cold air jet with $D_j = 2.5$ cm. at $M_j = 0.9$. We would estimate $U_j = 290$ m/s and $Re_D \approx 600{,}000$. At $x/D_j = 2$ using the mixing-layer estimates gives $Re_L \equiv u'L/\nu \approx 22{,}000$! Experiments show that at 90° to the jet axis the noise spectra peak at a Strouhal number $St_D \equiv fD/U_j = 0.3$, which for this jet corresponds to $f_{p_{90}} = 3.5$ KHz or $\lambda_{p_{90}}/D_j = 4.0$. Since the peak level of jet noise, which occurs at smaller angles to the jet, does not show Strouhal-scaling [26,27] but shows something like a Helmholtz-scaling it is important to estimate this peak frequency as well. Using $f_p D_j/a_\infty = 0.16$ from experiments [26–28] at 30° to the jet yields $f_{p_{30}} = 2$ KHz or $\lambda_{p_{30}}/D_j = 6.25$. These dominant acoustic wave lengths

---

[2]This neglects the effects of density-ratio and compressibility which can be restored in estimates for much higher speed jets.

can be compared with the dominant scales of turbulence at various streamwise stations. For example, if the comparison is made at $x/D_j = 2$, we get $\lambda_{p_{90}}/L_{(x/D_j=2)} = 14$, and $\lambda_{p_{30}}/L_{(x/D_j=2)} = 24$. Such ratios are useful in selecting the size of the computational domain and the grid-spacing. Closer to the nozzle these scale ratios are much more extreme. It is also evident from these estimates that in a near-sonic jet the spatial scales of energy-containing turbulence never match the acoustic wavelength of the dominant radiation (at any angle). This mismatch in spatial scales (or scale disparity) is more severe for lower speed jets and is responsible for the radiation inefficiency of these flows. However, these estimates should *not* be taken to imply that the noise sources in the jet radiate as localized compact acoustic sources. The spatial structure of the turbulence, as well as its temporal behavior, needs to be considered.

At any fixed station x, the turbulent fluctuations can be characterized using the space–time correlation $\langle u_i'(x + \xi, t + \tau)u_j'(x,t)\rangle$. For a fixed spatial separation ξ, a specific value of the time delay $\tau = \tau_m(\xi)$ gives the maximum correlation. This allows a convection velocity U_c to be defined, $U_c d\tau_m(\xi)/d\xi = 1$, and the decay of the peak correlation gives a *Lagrangian* decorrelation time τ_L. Measurements [19] show that in the mixing layer of the jet $U_c/U_j \approx 0.65$, $\tau_L \approx 4.5/\|dU/dr\|_{max}$ or equivalently that $u'\tau_L/L = 0.9$ and $U_c\tau_L/L = 4.1$. Since (subsonic) convection of a frozen eddy-pattern does not radiate sound, it is natural to associate the radiated sound with the evolution of the turbulence in the convected frame [3,29]. Associating the local turbulence of Lagrangian time scale $\tau_L(x)$ with radiation at a wavelength $\lambda(x) = a_\infty \tau_L(x)$ implies that in the mixing layer $\lambda(x)/L(x) \approx 7$ and $\lambda(x)/(U_c\tau_L(x)) = a_\infty/U_c \approx 1.5$. Evidently, the local turbulence contributes to sound at a spatial scale significantly larger than its integral scale. A similar conclusion is reached from the scaling of the noise peak at $f_p D_j/a_\infty = 0.16$, which is equivalent to $\lambda_p/D_j = 6.25$. There is, however, a caveat. Lighthill [30,31] stressed the acoustic inefficiency of noise radiation from bulk turbulence in the jet. This is consistent with the length scale ratios just discussed. However, if the flow processes in a jet *generate* very-large-scale motions, i.e. with spatial scales much larger than the *local* turbulence, the radiation efficiency of these *global* jet motions is likely to be rather high. Very-large-scale motions can dominate the acoustic radiation even when these motions are energetically weak.

The acoustic compactness of energetically dominant jet eddies is valid only in the Lagrangian frame. If viewed in a frame of reference fixed to the nozzle the sound-source-region is acoustically non-compact due to the convection of the turbulent eddy during its life-time. The specific numerical factors in these estimates would change if jets at other operating conditions are considered. Jets at low acoustic Mach number U_j/a_∞

have a greater scale disparity $\lambda(x)/L(x)$ and a greater amplitude disparity between the near-field turbulence fluctuations and the radiated sound. On the contrary when $U_c > a_\infty$ (supersonic eddy-convection) strong radiation results [29,32]. In the near-field this radiation has the structure of random Mach waves associated with the turbulent eddies. Similar but organized near-fields also arise for radiation from organized (supersonically convected) instability waves in high-speed jets [32].

3. A hierarchy of CAA simulations

A wide range of flow simulation methodologies can be used to study the problems of sound generation. These methodologies can be grouped according the range of spatial and temporal scales that are explicitly represented in the simulation. The influence of the flow-details that are not captured requires modeling. But apart from this, any specific approach may or may not aim to represent the sound that is generated by the unsteady flow. Accordingly the methods fall under two broad categories: direct and hybrid approaches. Fig. 6 provides a summary of the different approaches that are discussed in this section.

3.1. Direct computation of sound

These are methods that aim to compute both the unsteady flow and the sound generated by it. In view of the physical challenges listed in Section 1, these methods must use a domain that includes the noise-producing flow region and at least a part of the near-acoustic-field. Furthermore the computational mesh needs to be selected so that both the flow and its sound can be well represented. Once the physical realism of the computed solutions has been established, this approach provides benchmark databases to test and develop models of the unsteady flow and its sound generation. However the computational cost of such direct calculations is large, and only relatively simple flow configurations have been studied using direct methods. Specific review of the progress is deferred to Section 5, but we note that the model problems studied have gradually progressed from idealized cases (co-rotating vortices [33], vortex roll up and pairing [34]) towards the direct computation of nearly complete flow-regions ranging from supersonic jet [35], subsonic jet [36], turbulent vortex ring [37], subsonic cavity flow [38], isolated shock-cell noise source [39,40], to supersonic shear layer with a lip [41]. Although the Reynolds number of the computed flows is only modest, they have illuminated the underlying sound-generation processes and served to guide theoretical models. An illustration of this can be found in the work of Manning and Lele [42] who study the problem of the interaction between shear-layer vortices of a
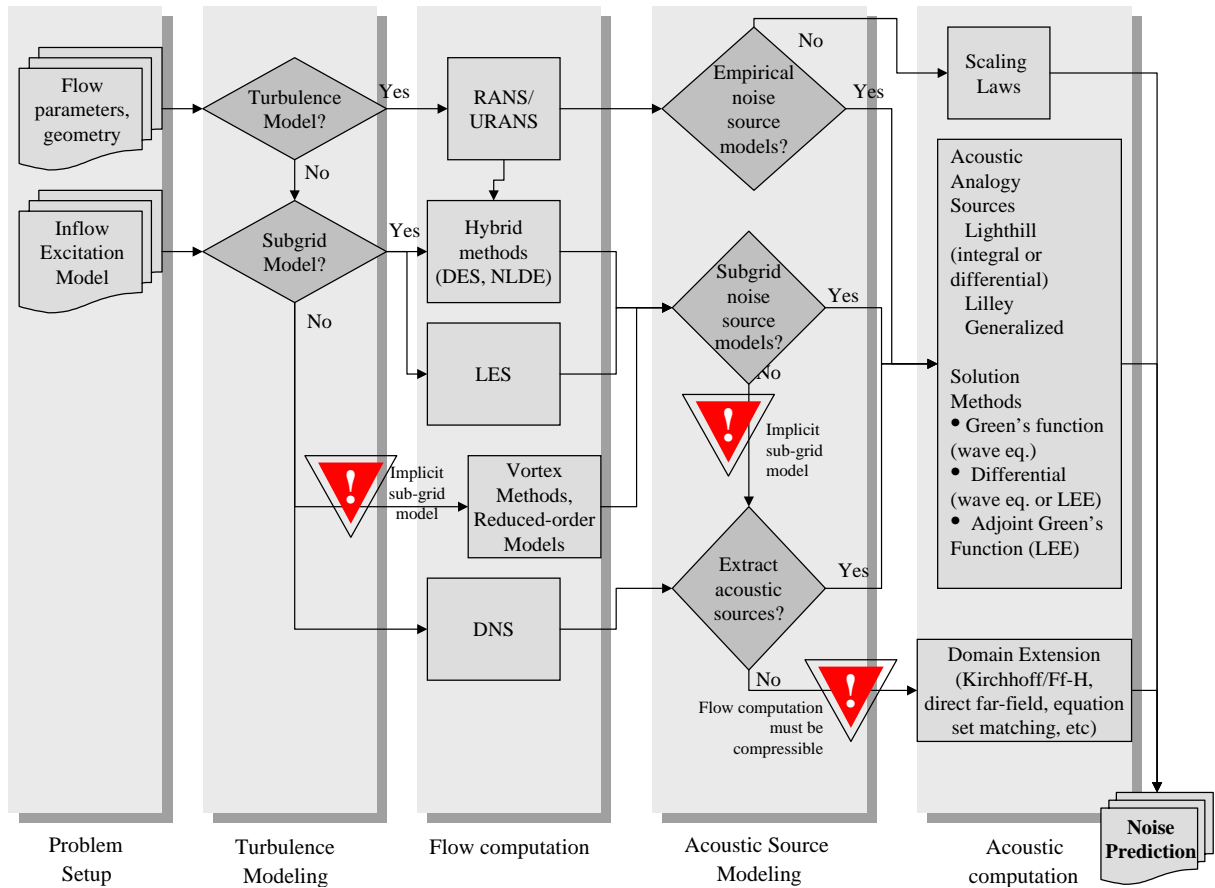
Fig. 6. A hierarchy of noise prediction methods.

supersonic shear-layer with a stationary wave-system in the supersonic flow as a model of sound generation in jet screech. Through a sequence of model problems they showed that this sound generation is in fact the leakage of otherwise trapped wave modes facilitated by the vortices. Details of physical mechanisms that generate sound in complex flows can be revealed by carefully conducted direct computations.

3.1.1. DNS or LES with compressible Navier–Stokes

If the flow is turbulent and the simulation attempts to capture the dynamics of all physical scales, it is termed direct numerical simulation, or DNS. Both the energy-containing range and the dissipative range of scales must be resolved in a DNS. Good sampling of the former requires long run times and domain sizes that are sufficiently large. Capturing the dissipative scales requires a sufficiently fine mesh, especially when accurate small-scale statistics are to be studied. In practice the adequacy of DNS is judged by ensuring that energy spectra (of the quantities of interest) decay sufficiently at high wave-numbers and frequency.

Similarly certain two-point correlations are required to decay sufficiently for large spatial and temporal separation. Budgets of fluctuating quantities provide another check on the physical realism. For example in an *equilibrium* turbulent flow the turbulent kinetic energy (TKE) dissipation is always a significant fraction of the TKE production. If this is not the case, the computed flow is quasi-laminar, unrealistically dominated by large-scale structures, or under-resolved.

In a large eddy simulation, LES, the objective is to only capture a range of energy-containing eddies. Motions on smaller scales, and in particular their effect on the resolved scales, is represented by a subgrid model. Ideally the subgrid models should reflect the physical effects of the missing-scales (e.g. energy-cascade to smaller scales, back-scatter, and progressive decorrelation of large-scales). In practise compromises are required for numerical stability, and computational efficiency. In LES, the effect of the subgrid model interacts strongly with the discretization errors inherent in the numerical scheme. This can have a significant impact on the acoustics associated with the flow. The

modeling and numerical issues associated with LES are discussed further in Section 3.3.

DNS and/or LES can be conducted in a domain that is large enough to contain a part of the near-acoustic field associated with the flow. In the case of DNS, this directly provides the near-acoustic field. For the LES only the sound field associated with the dynamics that have been captured is available, at least provided that it is not overwhelmed by errors associated with the SGS model. In both cases it is essential to ask whether the mesh used in the region away from the turbulent activity is sufficient to resolve the sound waves in the frequency range of interest. Care must be taken in designing the grid to ensure that sufficient resolution of acoustic waves is provided. If non-uniform meshes are used it is necessary to ensure that the coarsest mesh is sufficient for resolving the sound, and that grid stretching artifacts are minimized (see Section 4.1.7 for further discussion). Comparisons amongst calculations on different domain sizes and mesh resolutions provide essential assurance of the quality of the flow and acoustic data. This is also a good way to judge the impact of the numerical boundary conditions on the data, such as acoustic source strengths, being extracted from the simulation.

3.1.2. Extension of DNS or LES near-fields

A variety of methods are available to extend the near-acoustic field data to distances farther away. The simplest numerical approach is domain extension. This extension can be carried out using a mesh better suited for far-field propagation, for example a uniform cartesian mesh can be used. In the extended domain a simpler set of governing equations can be solved, for example linearized Euler equations, or their reduction to an acoustic wave equation. If a different equation set is used in the extended domain it is necessary to ensure that accurate and stable transfer of information is achieved at the grid interface (e.g. Freund et al. [43]). Also if a different mesh is used in the extended domain good quality interpolation schemes should be used. The comments made in the previous section about the care needed in mesh selection apply here as well.

Analytical methods can be exploited if the flow disturbances (in the extended region) are assumed to satisfy the acoustic wave equation. An integral formulation of the wave equation can be used and the surface enclosing the near-field is taken as a Kirchhoff surface (i.e. it encloses all acoustic sources of interest); the acoustic far-field is available as retarded-time surface integral on the Kirchhoff surface. This integral can be evaluated by numerical quadrature. The errors associated with quadrature must be kept in mind, particularly in view of the interpolation required due to the retarded-time. See for example Brentner [44] for a detailed discussion. Another source of error stems from an *open* Kirchhoff surface [45]. As is noted in Section 3.2

below, the use of an integral formulation due to Ffowcs Williams and Hawkings (Ff–H) [46] is a way to ameliorate this difficulty. In general, the Kirchhoff surface, or the Ff–H integration surface can have an arbitrary shape but convenience restricts these to surfaces that are easily represented on the mesh used in the simulation. Further analytical advantage is available if the Kirchhoff surface is cylindrical or spherical (or such that the wave-equation in the exterior domain is separable and its solution is available in terms of known special functions). In his DNS of a near-sonic jet, Freund [36] used a cylindrical Kirchhoff surface with analytical representation of the far-field sound in terms of the data collected on this surface. Such analytical representations avoid any further numerical error in the propagation of the waves to a far-field observer. They, however, require that dissipative effects on the far-field sound be negligible. In either case, the quality of the predicted far-field sound is directly linked to the quality of the near-acoustic field data from the simulation.

3.2. Hybrid methods for noise prediction

In contrast to direct methods, the hybrid methods do not aim to capture the radiated sound field but rather rely on a second calculation for predicting the noise. In some cases this can be carried out concurrently with the flow simulation. The noise prediction step can be formally based on either an aeroacoustic theory, or a flow-field decomposition.

3.2.1. DNS/LES with acoustic analogy

An acoustic analogy is a rearrangement of the equations describing conservation of mass and momentum; the right-hand side represents equivalent sound-sources (presumed known) that would radiate in an idealized hypothetical medium. The left-hand side is a partial-differential operator that represents sound propagation in the hypothetical medium. The unsteady flow field from DNS/LES can be used to compute the sound sources in the acoustic analogy. Once known, the partial-differential operator is inverted to predict the radiated sound field.

The most well known acoustic analogy is due to Lighthill [30] and the idealized hypothetical medium in which the sound propagates is the ambient medium at rest. This exact rearrangement gives

$$\frac{\partial^2 \rho'}{\partial t^2} - a_\infty^2 \frac{\partial^2 \rho'}{\partial x_i \partial x_i} = \frac{\partial^2 T_{ij}}{\partial x_i \partial x_j}, \qquad (1)$$

where $T_{ij} = \rho u_i u_j + (p' - a_\infty^2 \rho')\delta_{ij} - \tau_{ij}$, $\rho' = \rho - \rho_\infty$ is density perturbation, $p' = p - p_\infty$ is pressure perturbation, u_i is the flow velocity and τ_{ij} is the viscous stress tensor.

In this case the sound propagation is given by a simple Green's function and the exact source terms are the double divergence of the so-called *Lighthill stress-tensor* T_{ij}. Simplification of the exact source term to that representing the momentum flux in a constant density, incompressible flow, $T_{ij} \approx \rho_0 u_i u_j$, is asymptotically justified for a low-Mach number, acoustically compact noise-producing flow, see Crow (1970). The unsteady flow solution used to compute the sound sources can be based on incompressible or compressible equations. As a practical matter it is necessary to ensure that the source terms decay sufficiently towards the computational boundaries of the *noise-source region*, but it is *not* necessary to assume that the flow domain is acoustically compact. In cases where outflow of organized disturbances from the flow domain elevates the source-terms to a significant level at the boundary, it is necessary to adequately treat this aspect, since frozen convection of a disturbance at subsonic speed either into or out of the computational domain should not be a *source* of sound [47]. Methods to deal with this issue are discussed later in this section.

A Green's function that is tailored to the flow geometry should be used when this is possible. Such Green's functions can be accommodated within Curle's formulation [48] for stationary solid boundaries, or the more general Ffowcs Williams–Hawkings approach [46] can be used. Wang and Moin [5] in their study of sound generated by a turbulent flow over the trailing edge of a hydrofoil use incompressible LES to evaluate the Lighthill sound source terms, and predict the far-field sound using the half-plane Green's function [14]. It is also possible to use a numerically computed Green's function that accounts exactly for the surface geometry (e.g. [49]). Howe [12] provides a thorough discussion of the alternative strategies for predicting trailing-edge noise.

It is possible to use acoustic analogies with a better accounting of the sound propagation effects present in the real medium, such as the third-order Lilley's equation. In practice the exact equation is simplified in two steps. The nonlinear propagation operator on the left-hand side is replaced by the Pridmore–Brown operator that represents sound propagation in a transversely sheared flow, and the terms corresponding to the differences are neglected. The right-hand side source terms can also be approximated by the form given by Goldstein (1984) [50]. In shear flows the mean flow profiles evolve with streamwise position, causing some ambiguity about which shear flow profile to use on the left-hand side. A flow profile corresponding to the mean flow near the noise-generating region is found to give a good prediction of the radiated sound [34]. Goldstein [51] has given a new justification to this form of the source-term by establishing an acoustic analogy between the exact inviscid equations and the linearized equations of sound propagation in a transversely sheared flow by using transformed set of variables and specific source terms. The transformed set of variables become equal to the acoustic variables in the far-field.

The approach developed by Ffowcs Williams and Hawkings [46,52] provides a general method for noise predictions using Lighthill's acoustic analogy. Arbitrary rigid surfaces immersed in the flow can be treated in this way. The method does not require specially tailored Green's functions but their use makes the calculation more efficient. In this approach a generalized Green's formula is used to express the solution to the wave equation in terms of surface integrals over the body-surfaces immersed in the flow, integrals over other surfaces needed to enclose the integration domain, and volume integrals over the Lighthill source distributions, see general derivation in Crighton et al. [53]. A recent review of this method, particularly from a viewpoint of use with CAA, has been provided by Lyrintzis [54]. The Ffowcs Williams–Hawkings integral equation (Ff–H) allows natural treatment of moving surfaces, as well as *open* integration surfaces allowing the flow to enter and/or leave the computational domain [55]. In the latter context this formulation naturally sets up the required surface distribution of sources to ensure that no spurious sound is generated as vortical disturbances flow across the integration surface at subsonic speeds [56,57]. It is common to neglect the volume distribution of quadrupole sources in numerical implementations of the solution to Ff–H equation. Brentner and Farassat [58] show examples from helicopter rotor noise where the quadrupole terms contribute significantly. But when vortical flow passes through the integration surface the quadrupole contribution shows a spurious fluctuation which can dominate the predicted noise. Wang et al. [59] developed an effective treatment of this error in the context of Lighthill's equation. They treat the vortical outflow as *frozen convection* over a short distance (of two grid cells) near the integration surface to correct for the convected flux of *source strength*. A related approach was developed by Mitchell et al. [60] for treating the outflow of coherent vortex rings in the context of jet noise. A careful study of the use of Ff–H equation for far-field noise prediction in CAA has recently been conducted using model sources and the DNS of a transonic cavity flow [61]. The results obtained are particularly noteworthy considering the closeness of the integration surface to the cavity surface. The flow near the integration surface is definitely nonlinear! Comparison were also made with a prediction using a Kirchhoff-surface (with uniform free-stream) at the same location, and also provided reasonable predictions. In other applications the accuracy of Kirchhoff-surface based predictions is observed to degrade when the surface in within the nonlinear flow region [54,58].

3.2.2. Vortex methods with acoustic analogy

Vortex methods provide an alternative methodology for computing unsteady flows [62,63]. While it is possible, in principle, to simulate viscous flows using vortex methods, their principal attraction for CAA is that they provide a dynamic *model* of the unsteady, essentially inviscid, flow at a dramatically reduced cost. Its fidelity for flow prediction depends on the range of scales that are accurately represented for a chosen vortex-discretization. Once the computational model has been validated against more detailed calculations or experiments, an efficient simulation tool becomes available for looking at the impact of geometrical variables on the flow and its sound. The latter can be computed by combining an acoustic-analogy solver with the unsteady flow data provided by the vortex method.

In a two-dimensional flow finite sized vortex blobs/particles are used. They can be combined with methods for incompressible potential flow solution about aerodynamic body shapes of interest. Guo [64,65] has exploited conformal mappings for potential flows with a numerical solution using vortex blobs to compute the noise associated with flow separation from leading and/or trailing edges for isolated airfoils and high-lift configurations. For acoustic predictions a two-dimensional version of the Ff–H formulation was used. Howe [12,66] also illustrates the use of unsteady flow models based on vortex methods in the context of trailing-edge scattering. These methods have the potential of providing a quick assessment of the design variables on the radiated noise. The comparisons with the experimental data shown by Guo are quite encouraging. It should be stressed that the noise prediction can only be trusted if there is sufficient confidence in the simplified flow model. Three-dimensional flows are much more challenging to simulate with vortex methods. Either vortex-filaments or 3-D blobs/vortex sticks are used. The filaments preserve the inviscid invariants of the fluid motion (e.g. circulation) in a natural way, but rapidly get distorted and reparameterization and smoothing become necessary. Three-dimensional blobs/sticks are also subject to stringent rules to ensure that the vorticity they represent is divergence free, and to ensure that the inviscid invariants are maintained. Recently a vortex filament simulation of jet flows including modeling of the nozzle geometry such as mixer lobes, and tabs has been under development [67], and the results obtained have been encouraging. Another recent advance is the development of vortex methods for compressible flows [68]. This type of method, when extended to treat the presence of solid boundaries, can be an effective way to study noise-generation processes.

3.2.3. Incompressible/acoustic split

In recent years several groups have proposed computational methods for predicting the radiated noise without an explicit use of an acoustic analogy. The general idea of these methods is to compute the unsteady flow responsible for the noise with incompressible equations and then overlay a simplified set of compressible flow equations to predict the radiated noise. Hardin and Pope [69] proposed such a scheme for noise predictions from low-Mach-number flows and showed several successful test cases. Their method is based on computing a near-field density variation (called *hydrodynamic density correction*) due to the pressure variations inherent in the incompressible flow. The time variation of the *hydrodynamic density correction* is used to drive isentropic perturbations in pressure (density) and velocity. These are regarded as acoustic perturbations and the equations governing them are formed by subtracting the incompressible flow equations from the full compressible set. These acoustic disturbance equations are solved on a mesh that resolves only the acoustic field whose wavelength is much larger in a low-Mach-number flow. The derivation of this method is plausible but lacks full rigor since the singular perturbation of the compressible equations, in the limit of small Mach numbers, is not recognized in the derivation. In some ways the method is a computational equivalent of Ribner's theory of aerodynamic sound, which uses fluid-element dilatation as a primary variable. The slow decay of dilatation away from the *source region* has raised serious criticism of this theory in the past [70,1]. This difficulty is apparently circumvented in the computational approach as the near-field dilatation is not explicitly computed and a large mesh-spacing is used for the *acoustic* field. Some technical issues associated with the method require further exploration (see [71,72] for comments). This method was extended by Shen and Sorenson [73] to allow for entropy variations in the base state. Goldstein [74] provides a general acoustic analogy framework that may be useful in rationalizing methods that invoke a split between the flow and the acoustic variables.

3.2.4. Linearized Euler with source terms

Other approaches have been proposed to extend the near-field compressible flow data to the radiated acoustic field. These include numerical solution of linearized (modified) Euler equations (LEE) with specific source-terms [75] and LEE with projected source-terms [76]. The numerical difficulty of this approach stem from the fact that the full LEE set (say about a transversely sheared flow) admits non-trivial instability wave solutions of the homogeneous equations (i.e. with zero source terms). As these instability waves grow, they contaminate the near acoustic field and the errors inherent in the boundary schemes or mesh nonuniformities spuriously reflect them into radiating acoustic waves. The same fundamental problem was faced previously in the context of analytical predictions of

radiated sound using Lilley's acoustic analogy [3,77,50,78]. The third-order Pridmore–Brown equation is equivalent to the inviscid linearized stability equation for compressible shear flow [3]. In the theoretical studies the homogeneous instability wave solution was suppressed on the grounds that the physical solution is bounded.

Several distinct approaches have been proposed to overcome this problem of the unbounded homogeneous solution. The approach adopted by the Lyon group [75] is to modify the LEE by suppressing the linear terms involving the mean-flow gradients. This is essentially a geometrical acoustics approximation and suppresses the homogeneous solution and the associated numerical difficulties. For source terms the nonlinear fluctuating momentum fluxes in the linearized momentum equations and zero source terms in other equations are used. This choice for the source terms reduces precisely to Goldstein's form of the sound source term in the third-order wave equation for a transversely sheared flow. Whether this form of the source term is sufficient for other more complex base flows, e.g. flow impingment and subsequent spreading on a surface, is not known. For the test problems considered thus far this modified LEE approach provides reasonable noise predictions. A different approach to overcome the parasitic homogeneous solution is devised by Ewert et al. [76]. They propose a source-term projection approach where the full source-terms due to flow nonlinearity are projected to eliminate any excitation of the homogeneous solution. Since this projection is defined in the wavenumber-frequency domain a practical implementation requires further approximations. In more recent work, this group [79] has proposed a different scheme that reduces to the second-order Möhring's equation [80] or the equation proposed by Pierce [81], which do not permit a non-trivial homogeneous solution. Since Pierce's wave equation is explicitly derived to be *correct* to first order in a geometrical acoustics sense, the method proposed should be carefully evaluated for intermediate frequencies. Further work is needed to evaluate these recent developments. Results obtained in a boundary layer by solving the linearized version of Möhring's equation with a prescribed concentrated source [82] do capture the important features of the radiation field obtained by analysis and DNS by Suzuki and Lele [83].

In this connection recent work by Goldstein [74,51] should prove helpful. The generalized acoustic analogy is an attractive framework for defining the *flow* variables (called base state) and the sound (called *residual* variables). This framework provides a general *definition* for the source terms, as in other acoustic analogies, but since the base state can be chosen to be close to the real flow there is a potential for simplifying the source-terms. Goldstein [84] takes this one step further and offers a different treatment of the *homogeneous* solution. It is

proposed that a non-parallel base state be used so that the *homogeneous* solutions are bounded (they are driven by the initial and boundary data). The acoustic field is the sum of a homogeneous solution and a particular solution from the source-terms in the equations. Formulation of the linear adjoint problem facilitates the computation of the radiated field. The use of adjoint solutions to relate source statistics to the statistics of the radiated sound is also exploited by Tam and Auriault [85].

3.3. Large eddy simulation

High Reynolds number turbulent flows contain a broad range of spatial and temporal scales. The ratio of the energy-containing scale L (large-scale) to the small-scale dissipative motions, characterized by the Kolmogorov scale η, increases as $L/\eta \sim Re^{3/4}$, where $Re = u'L/v$ is a Reynolds number characteristic of the energy-containing scales. Similarly the dynamic range of eddy time-scales also increases with Reynolds number. For full-scale hardware in aviation, Re is large, making it is impossible to capture the full range of dynamical scales in a computational model. For example, for a full-scale jet engine the turbulence Reynolds number, Re, is about 10^6–10^7 and even for a laboratory-scale jet, with exit diameter of 1 in, Re is 10^3–10^4. DNS of laboratory-scale jets is not possible on the largest computers available today. A compromise is to explicitly represent only the large scales of the flow and model the smaller scales. This is the objective of a Large Eddy Simulation (LES). Recent reviews of LES methods are available [86–91], and the monograph by Pope [92] provides a detailed discussion of the technical issues and models used. We will not attempt to review this rapidly growing literature and confine the discussion to the issues of direct relevance to the prediction of the radiated noise.

3.3.1. LES equations and subgrid modeling

The equations used for conducting large eddy simulations are obtained by filtering the exact compressible flow equations to remove the small-scales. Conventional practice is to use a density-weighted- or Favre-filtering [93,94]. This yields LES equations for compressible flows that are close to the LES equations in widespread use for incompressible flows. It is physically more appealing to use non-density weighted filtering. This also offers some numerical advantages when non-dissipative high-order schemes are used for discretization. Using overbar to denote the filtered variables, the governing equations are:

$$\frac{\partial}{\partial t} \bar{\rho} + \frac{\partial}{\partial x_i} \bar{\rho} \, \bar{u}_i = -\frac{\partial}{\partial x_i} (\overline{\rho u_i} - \bar{\rho} \, \bar{u}_i) \equiv -\frac{\partial}{\partial x_i} m_i, \qquad (2)$$

$$\frac{\partial}{\partial t}(\overline{\rho}\,\overline{u}_i) + \frac{\partial}{\partial x_j}(\overline{\rho}\,\overline{u}_i\overline{u}_j) + \frac{\partial}{\partial x_i}\,\overline{p} - \frac{\partial}{\partial x_i}\,\overline{\tau}_{ij}$$

$$= -\frac{\partial}{\partial t}(\overline{\rho u_i} - \overline{\rho}\,\overline{u}_i) - \frac{\partial}{\partial x_j}(\overline{\rho u_i u_j} - \overline{\rho}\,\overline{u}_i\overline{u}_j). \tag{3}$$

In this non-density-weighted formulation, the mass balance (2) includes the subgrid-scale mass flux m_i, which requires additional modeling. The momentum balance (3) involves the subgrid momentum flux $r_{ij} \equiv (\overline{\rho u_i u_j} - \overline{\rho}\,\overline{u}_i\overline{u}_j)$, which requires modeling. Typically the subgrid-scale contribution to the viscous stress τ_{ij} is neglected. Accordingly, $\overline{\tau}_{ij} = \overline{\mu}(\overline{u}_{i,j} + \overline{u}_{j,i} - \frac{2}{3}\delta_{ij}\overline{u}_{k,k})$, where the subscript $,j$ denotes spatial derivative in x_j.

The energy balance can be formulated in several different ways. One of the simplest is expressed in terms of the total energy density per unit volume, $E_t = \rho e + \rho u_i u_i/2$, where e is the internal energy per unit mass. This variable is attractive for CAA because for an ideal gas $\rho e = p/(\gamma - 1)$, where γ is the ratio of specific heats. Now, $\overline{E}_t = \overline{p}/(\gamma-1) + \frac{1}{2}\overline{\rho}\,\overline{u}_i\overline{u}_i + k_s$, where $k_s = \overline{\rho u_i u_i}/2 - \overline{\rho}\,\overline{u}_i\overline{u}_i/2$ is the subgrid kinetic energy (per unit volume). It is convenient to express the energy balance in terms of the resolved total energy density, $E_l = \overline{p}/(\gamma-1) + \overline{\rho}\,\overline{u}_i\overline{u}_i/2$. Its governing equation is

$$\frac{\partial}{\partial t}E_l + \frac{\partial}{\partial x_j}((E_l + \overline{p})\overline{u}_j) - \frac{\partial}{\partial x_j}(\overline{\tau}_{ij}\overline{u}_i) + \frac{\partial}{\partial x_j}\,\overline{q}_j$$

$$= -\frac{\gamma}{\gamma-1}\frac{\partial}{\partial x_j}(\overline{p u_j} - \overline{p}\,\overline{u}_j)$$

$$- \frac{\partial}{\partial t}(\overline{\rho u_i u_i}/2 - \overline{\rho}\,\overline{u}_i\overline{u}_i/2)$$

$$- \frac{\partial}{\partial x_j}(\overline{\rho u_i u_i u_j}/2 - \overline{\rho}\,\overline{u}_j\overline{u}_i\overline{u}_i/2). \tag{4}$$

Terms representing the redistribution of total energy due to viscous and conductive sub-grid scale processes have been neglected [93,95,96]. Thus $\overline{q}_j = -\overline{k}\,\overline{T}_{,j}$, is the conductive heat-flux. It is evaluated with the approximation $\overline{T} \approx \widetilde{T}$, where the Favre-filtered temperature $\widetilde{T}$ is given by the equation of state (ideal gas) $\overline{p} = \overline{\rho}R\widetilde{T}$. The last two terms on the right-hand side of (4) are typically neglected. The remaining subgrid energy flux is modeled as $\frac{\gamma}{\gamma-1}(\overline{p u_j} - \overline{p}\,\overline{u}_j) \approx (\overline{\rho T u_j} - \overline{\rho}\,\overline{T}\,\overline{u}_j) \equiv q_{sj}$.

The following subgrid models provide closure for the subgrid fluxes of mass m_i, momentum r_{ij} and energy q_{si}, respectively:

$$m_i = -C_\rho \Delta^2 \|\overline{S}\|\overline{\rho}_{,i}, \tag{5}$$

$$r_{ij} = C_s\overline{\rho}\Delta^2\|\overline{S}\|\overline{S}_{ij} = \overline{\rho}v_s\overline{S}_{ij}, \tag{6}$$

$$q_{si} = -C_T\overline{\rho}\Delta^2\|\overline{S}\|\overline{T}_{,i}. \tag{7}$$

The subgrid momentum flux model (6) is the well-known Smagorinsky model with a subgrid viscosity v_s. The subgrid mass flux model follows a similar Boussinesq hypothesis at subgrid level. The energy flux model (7) is the usual model with a subgrid Prandtl number [93] that

has been rearranged for numerical convenience. In these models Δ is the width of the LES filter, which is usually related to the local grid spacing, $\Delta = \{\Delta_x\,\Delta_y\,\Delta_z\}^{1/3}$; $\overline{S}_{ij} = \frac{1}{2}(\overline{u}_{i,j} + \overline{u}_{j,i} - \frac{2}{3}\delta_{ij}\overline{u}_{k,k})$ is the trace-free strain rate, and $\|S\|$ is its modulus. The model coefficients C_ρ, C_s and C_T are often determined following the standard dynamic procedure [93,96].

The basic idea of dynamic evaluation of subgrid model coefficients is illustrated here in the context of the mass flux model (5). Suppose that this model holds also for *test-filtered* fields obtained by test-filtering the LES fields using a spatial filter whose width, $\hat{\Delta}$, is larger than the original LES filter width Δ. The test filtered fields will be denoted by putting a hat (or carat) on top. The test-filtered subgrid mass flux is then

$$M_i = \widehat{\overline{\rho}\,\overline{u}_i} - \hat{\overline{\rho}}\hat{\overline{u}}_i. \tag{8}$$

Now from the definitions of LES- and test-filtering it follows that

$$M_i - \hat{m}_i = \widehat{\overline{\rho}\,\overline{u}_i} - \hat{\overline{\rho}}\hat{\overline{u}}_i. \tag{9}$$

This identity provides a way to evaluate C_ρ. The left-hand side of (9) is expressible via (5), for M_i in terms of C_ρ, $\hat{\Delta}$, and the test-filtered variables, and for m_i in terms of C_ρ, Δ, and the LES variables. The right-hand side of (9) is known from the test-filtered variables. Consistency between them allows C_ρ to be found by a least-squares (or a weighted least-squares) method [97].

The dynamic subgrid models described here are the simplest models that have been successfully used in a variety of flows ranging from decaying isotropic turbulence, turbulent channel and pipe flows, boundary-layers, jets, wakes and mixing layers to more complex flows involving flow separation such as in an asymmetric diffuser or sudden-expansion. The LES methodology has been most extensively tested and validated for low speed incompressible flows, see reviews [86–91] for recent successful predictions and the challenges ahead. For compressible flows, development and validation is actively being pursued by several groups.

3.3.2. Numerical issues particular to LES

Motions with scales comparable to the grid-spacing may have significant energy in the LES of high-Reynolds number flows. Non-linear numerical instability due to aliasing errors (from the nonlinear terms in the governing equations) is encountered on coarse meshes. Experience with the use of high-order central difference schemes for LES [96,98] indicates that grid-to-grid oscillations can become locally dominant and cause numerical instability. These spurious oscillations are reduced by filtering $\overline{S}_{i,j}$, and a reformulation of the convective terms to reduce aliasing errors [99,100]. Both of these were used in the jet LES by Boersma and Lele

with a centered sixth-order compact scheme. They found that the non-density weighted LES formulation, which provides a subgrid diffusive term in the density equation, was helpful for numerically stability. Other work has used a direct approach of explicitly filtering the LES field variables at every time step [101], or the approach of controlling the build up of *energy* at short spatial scales by the addition of artificial selective damping ([102]). The latter approach is used in the recent jet LES study of Bogey, Bailly and Juve (2000). Constantenescu and Lele [98] used a filtering of the flow variables every 200 time steps. Approaches to achieve robust simulations, without degrading the wideband spatial resolution of the calculations remains an active area of new work. A staggered arrangement of flow variables in combination with compact-finite difference scheme shows promise [103]. Another recent development is based on discrete conservation of entropy and entropy variance [104] to avoid nonlinear instability. It seems to be effective for both co-located and staggered meshes. Numerical methods which enable LES of flows in complex geometries by ensuring kinetic energy conservation have been developed recently [105]. They are being applied to simulate complex flows arising within realistic gas-turbine combustor geometry.

LES of wall-bounded turbulent flows present additional challenges. Resolving the physics of near-wall turbulence requires that near-wall structures of the spanwise spatial scale of the order of 50–100 viscous wall units be captured. This places a severe near-wall resolution requirement on a near-wall structure capturing LES (see Chapman [106]). Wall models attempt to represent the effect by employing different effective wall boundary conditions [88,89]. Recently this approach was reformulated using a dynamic eddy-viscosity model of the near-wall region [107]. This approach dynamically combines RANS treatment of the near-wall region with LES approach further away from the wall. Other computational approaches which combine the capabilities of RANS in one flow region with LES is other regions of the flow are actively being developed by many groups.

3.3.3. Refined subgrid models

The subgrid models in use for compressible flow LES have several restrictions. The commutation error due to the lack of commutation between the LES filtering and differentiation is usually ignored. This can be improved by the use of test-filters that reduce the commutation error to a desired order of accuracy [108]. The Smagorinsky model shows very limited correlation in a priori tests of the model on DNS fields. A model like Bardina's mixed model [109] where *scale-similarity* terms are added give better correlations. The trace of subgrid stresses (SGS kinetic energy) is often neglected in LES calculations. While a model for this is available [94], in practice it is not used either due to numerical instabilities [100], or its lack of influence on the calculations [93]. Refinements are also possible in the non-density-weighted formulation of LES. A recent development is the notion of *deconvolution* to extract near-filter scale information to construct a better estimate of the sub-filter scale fluxes [110,111]. This has been used in a LES study of jet noise from a rectangular nozzle [112].

3.3.4. Acoustic implications of SGS models

The ratio of the local mesh size to the turbulence integral scale $\Delta/L(x)$ is the primary factor that determines the range of eddy-frequencies that are well represented in an LES calculation. The range of length and time scales at a given station can be estimated from local estimates of the turbulence parameters $u_0(x)$ and $L(x)$. For this we use an empirical modified von-Karman–Kraichnan spectrum for the three-dimensional energy spectrum $E(k)$ as a function of the wavenumber k:

$$E(k) = \frac{3}{2I_1} \frac{u_0^2}{k_0} \frac{(k/k_0)^4}{(1 + \frac{12}{5}(k/k_0)^2)^{17/6}} \exp\{-\beta Re^{-3/4} k/k_0\}.$$

(10)

This empirical spectrum[3] depends on three parameters: velocity scale u_0, integral scale L expressed via the wavenumber k_0, and the turbulence Reynolds number based on these $Re = u_0 L/v$. It contains no information about the anisotropy or the inhomogeneity of the energy-containing eddies. For estimation purposes these effects are assumed to be secondary. This empirical spectrum provides several notable built-in features. The low-wavenumber spectrum is proportional to k^4, and blends into the $-5/3$ Kolmogorov inertial subrange $E(k) \sim C\varepsilon^{2/3}k^{-5/3}$ adopted from the von-Karman spectrum ([113, p. 244]). It has a high wave number viscous roll-off consistent with Kraichnan's theory [114] which has been observed in recent high-Reynolds number turbulence measurements [115,116]. Using the normalization $\int_0^\infty E(k)\,dk = \frac{3}{2}u_0^2$ gives the normalization factor $I_1 = 0.1149$ for high Re. The spectrum has peak energy at $k/k_0 = 1$, and is consistent with the Kolmogorov estimate of dissipation $\varepsilon = Au_0^3/L$, where L is the longitudinal integral scale and A is a constant. Measurements indicate that $A \approx 1$ [117]. Using $A = 1$ gives $k_0 L \equiv I_2 = 1.608$ when the value of the Kolmogorov constant C is taken as 1.5. This value of $k_0 L$ is close to the estimate $k_0 L = 1.8$ given by Tennekes and Lumley [118]. Matching the high wavenumber roll off to the experimental data [115,116] gives $\beta = 8.36$.

Energy spectra at turbulence Reynolds number $Re = u_0 L/v$ of 10^3, 10^4, 10^5 and 10^6 are plotted in Fig. 7. In this figure the wavenumber axis is the nondimensional

---

[3]Pope (2000) describes a similar empirical master spectrum.

wavenumber k/k_0 and is logarithmic, so that the full range of spatial scales can be easily observed. On the vertical axis weighted energy spectra $\frac{k}{k_0}\left\{\frac{E(k)}{u_0^2/k_0}\right\}$ are plotted on a linear scale. This choice makes the *visual* area under the curve proportional to the energy content at each wavenumber. The group of four curves all with their peaks near $k/k_0 = 1$ correspond to the energy spectra (the peak of $E(k)$ is exactly at $k/k_0 = 1$). Evidently, in this range of Reynolds numbers the distribution in the *energy-containing scales* is not substantially affected by the Reynolds number. The normalization factor $I_1 = 0.1149$ (based on $Re \rightarrow \infty$) is used for all four curves. As expected, there is very little kinetic energy in the spatial scales with $k/k_0 > 10^2$. The other four curves on this plot show the estimated distribution of kinetic-energy dissipation for the four Reynolds numbers. The quantity $k/k_0\left\{\frac{1}{Re}\left(\frac{k}{k_0}\right)^2\frac{E(k)}{u_0^2/k_0}\right\}$ is plotted so that the *visual* area under the curves reflects the distribution of dissipation over spatial scales. For isotropic turbulence $\varepsilon = 2\nu\int_0^\infty k^2 E(k)\,\mathrm{d}k$, which motivates the choice of the variable plotted. As is evident from the plot, the scale at which peak dissipation occurs moves to higher and higher wavenumbers as the Reynolds number is increased, but the total dissipation rate (area under the curves) remains constant. The wavenumber of peak dissipation corresponds to $k\eta = 0.1$ (shown by the long tick marks) in agreement with experimental data. The most notable feature of this figure is that at high Reynolds numbers (e.g. $Re = 10^6$) there is negligible overlap between the energy-containing scales and the dissipative scales. At smaller Reynolds

numbers there is progressively more overlap. Also note that for $Re = 10^3$ the dissipation peak is within $k/k_0 < 10^2$, while for $Re = 10^4$ and higher the dissipation peak falls beyond $k/k_0 = 10^2$.

The energy spectrum also allows an estimate of the *local* timescale of eddy motions of different scales. For this the inverse eddy-turnover-time (or frequency), $f(k) = \frac{1}{\tau(k)}$, with a wavenumber k is estimated as $f(k) = \frac{1}{\tau(k)} = (k^3 E(k))^{1/2}$. Fig. 7 also shows a plot of the normalized eddy turnover frequency $\tau_0/\tau(k) = \{(k/k_0)^3 \frac{E(k)}{u_0^2/k_0}\}^{1/2}$ at different Reynolds numbers. The normalizing frequency is chosen as $\frac{1}{\tau_0} = k_0 u_0$. As expected the range of eddy turnover frequencies becomes broader as Re increases. In turn, there is a broader range of frequencies in the spectrum of the radiated noise. Interestingly the distribution of eddy frequencies is well approximated by the inertial range scaling $\frac{f}{f_0} \sim C^{1/2}(k_0 L)^{-2/3}(k/k_0)^{2/3} = 0.892(k/k_0)^{2/3}$ (see Fig. 7). This eddy-frequency estimate is useful in assessing the resolution needs for LES. An ideal numerical method would give $k_{\max} = \pi/\Delta$, where Δ is the grid spacing or the LES filter width. Usually discretization errors are small only for $k < \frac{2}{3}k_{\max}$ even for high bandwidth schemes, as discussed in Section 4.1. This latter estimate gives $f_{\max}/f_0 \approx 0.5(\Delta/L)^{-2/3}$. For $\Delta/L = \frac{1}{32}$ the highest resolved eddy frequency is only about 5 times larger than the energy-containing eddy frequency, f_0. For $\Delta/L = \frac{1}{128}$ we get $f_{\max}/f_0 \approx 13$. Since the computational domain must also be several $L(x)$ wide in each direction, the number of grid points needed to achieve these frequency-bandwidth targets are at least a factor of 4 larger than 32 or 128 in each direction. The conclusion from this analysis is that the range of acoustic frequencies that can be captured in LES depends primarily on the value of Δ/L in the dominant noise-generating region. Computational cost considerations therefore imply that a significant subrange of frequencies that are annoying to humans will be missing in a practical LES calculation. This suggests that acoustic models of the missing scales will be important in the overall noise prediction.

A direct indication of these missing scales is evident in recent jet LES calculation by Bodony and Lele [119], shown in Fig. 8. These calculations are discussed further in Section 5.2.3 but it suffices to note that as the number of grid points is increased (by an overall factor of 10) the frequency spectrum of the far-field noise picks up in the high frequency range towards the empirically observed jet noise spectra. This comparison is made at an observer angle of $30°$ from the jet axis, and similar trends are observed at other angles as well.

These considerations bring up a related numerical issue. The best SGS models should not only represent the effect of the un-represented dissipative scales on the dynamics of the scales retained in the LES, but also do
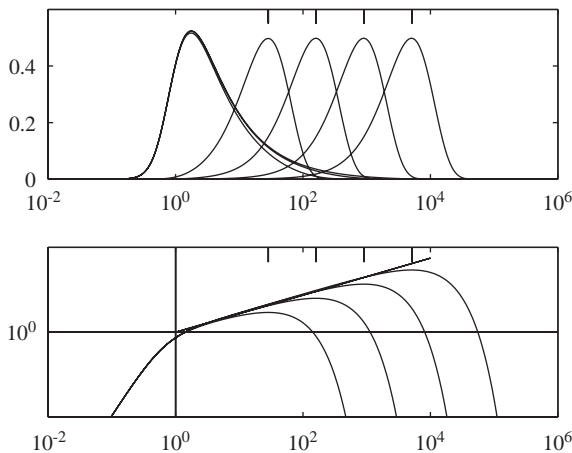

Fig. 7. Weighted energy and dissipation spectra for high Reynolds number turbulence; The turbulence Reynolds number $Re = u_0 L/\nu$ varies from 10^3 to 10^6 in factors of 10. The left curves in the top figure are energy spectra, and those on the right are estimated dissipation spectra. The lower figure shows eddy-frequency versus wavenumber.
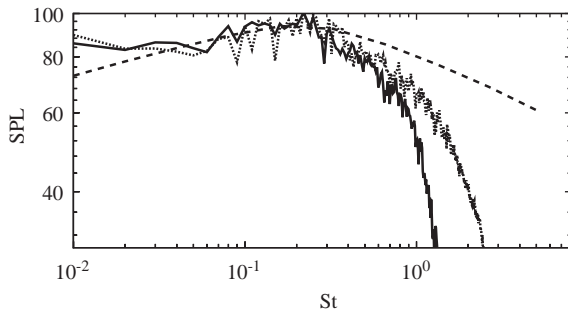
Fig. 8. Predicted far-field noise spectrum from LES of an unheated, $M_j = 0.9$ jet by Bodony and Lele [119]; .... LES with 10^6 points; — LES with 10^5 points; - - - - Empirical jet noise spectra from Tam.

so in a way that does not produce spurious acoustic radiation from the SGS model itself. This additional requirement is not automatically satisfied by the SGS models. Internal consistency between the subgrid terms in the mass, momentum, and energy equations is required to ensure that the SGS terms do not behave as dominant acoustic sources. In the context of the non-density-weighted LES formulation, Boersma and Lele [96] note that the subgrid mass-flux terms in the mass and momentum equations counteract each other (in the sense of Lighthill's acoustic analogy) and do not yield a dominant noise source. The subgrid momentum fluxes, and the subgrid heat-fluxes do appear as *sources* in a Lighthill wave-equation for the filtered density equation. The acoustic consequences of such SGS terms have not been examined in a systematic way for engineering flows. There have been some a priori studies of these acoustic source terms using DNS databases in isotropic turbulence [120,121] and for a plane channel flow [122] and a mixing layer [123]; the available information on the actual acoustic output of the SGS terms [124,125] is limited to simple flows.

Once it has been ensured that the SGS models are acoustically non-dominant relative to the noise generated by the resolved-scales, the problem of estimating the high-frequency noise due to un-represented scales needs to be addressed. Prediction methods that can estimate the acoustic output of these higher-frequency motions are needed. These can be referred to as *SGS acoustic source models* in much the same way as the current SGS models are regarded as *SGS turbulence models*. Prediction methods that allow the acoustic output of the un-represented scales to be estimated and combined with the acoustic output of the scales captured in LES are being developed [123,126]. In this connection the theoretical scalings for the high-frequency noise spectra from isotropic turbulence [127,128] should be mentioned. A recent study of decaying isotropic turbulence [129] shows that if LES captures

the time evolution of the energy spectra, the noise spectra are expected to be well captured. However, realistic flows are typically inhomogeneous and the additional effects of refraction and scattering are important for the high-frequency sound. These effect need to be accounted in relating the SGS noise sources to the far-field sound [126].

4. Computational issues

Numerical methods for problems of sound generation and propagation must overcome a host of difficulties that arise because acoustic waves are very weak compared to near-field fluctuations, and because they must propagate with little attenuation over long distances. In practice this has dictated the use of high-order-accurate numerical methods, and in particular compact (Padé) and optimized finite difference (FD) and Runge–Kutta time marching schemes, and close attention to other sources of error such as boundary conditions (BC).

Rapid development of many CAA codes, utilizing different numerical methods has also drawn attention to the need for careful validation of codes and comparisons of not only the accuracy of different schemes, but also computational speed comparisons for identical problems. The Aeroacoustics Conferences of the American Institute of Aeronautics and Astronautics have featured special sessions on Computational Aeroacoustics since 1992, and 4 workshops on benchmark problems in CAA have been sponsored by NASA in 1995, 1996, 2000, and 2003 [130]. It would be impossible to review the conclusions from all these studies; the material discussed below should be considered as representative rather than exhaustive. Omitted results largely reinforce the themes of this section: that careful attention must be accorded to issues of accuracy, artificial dissipation, nonreflecting and inflow/outflow BC, and validation of results.

4.1. Spatial discretization

Other things being equal, the best choice of discretization for a given geometry and accuracy requirement is the one that is most computationally efficient, i.e. the one that requires the smallest computing time for a given error tolerance. Other factors that determine the best choice of method include ease of implementation (and especially imposition of BC), efficiency of parallelization, memory requirements, and the potential for straightforward implementation in different geometries and flow configurations. For the most part, the trade-offs between these issues have favored finite difference (FD) methods (especially high-order-accurate and optimized methods). Before discussing these methods in

detail, we begin by discussing other discretization methods and their uses in CAA.

Spectral and pseudo-spectral methods (with fast transforms) are generally very efficient for simple geometry and BC. As such, spectral methods have been widely used in CAA to discretize homogeneous (periodic) coordinate directions in aeroacoustic computations, such as the azimuthal direction of a cylindrical-polar coordinate system [131]. They have also been used for *near field* turbulence calculations where data was subsequently analyzed with acoustic analogies [132–134]. However, when periodic BC are used for the streamwise coordinate (temporally evolving flow), caution must be exercised in interpreting the resulting sound generation [134].

Likewise, finite element and spectral element methods have been developed for the compressible Euler and Navier–Stokes equations. In particular, the Discontinuous Galerkin (DG) method (e.g. [135]) has been examined by a number of investigators for CAA problems [136–143]. DG is a finite-element method based on high-order-polynomial basis functions, but inter-element fluxes are coupled by solving an approximate Riemann problem, rather than by imposing continuity constraints as in the traditional Galerkin discretization. This produces a more compact discretization that is amenable to larger meshes and more efficient parallelization. Upwinding of the inter-element fluxes produces a dissipative error but it diminishes with increasing polynomial order. Detailed wave propagation characteristics of the scheme have been analyzed by Hu et al. [144] (analogously to what is presented in sections below for finite-difference schemes). The potential advantages over high-order finite-difference methods discussed below is the ability to use complex unstructured meshes (and adaptive refinement). While work on the DG method for compressible Navier–Stokes equations is still relatively recent, it is likely to be increasingly useful on full-scale DNS/LES problems such as those described in Section 5.

Finite-volume schemes are attractive because the staggering of fluxes with respect to the conserved variables allows global conservation principles to be enforced discretely. These principles are especially important in LES, where energy must not be allowed to accumulate at the grid scale. Similar staggered schemes for spectral element [136] and finite difference [103] discretizations have recently been extended to compressible flows. Vortex particle methods, either together with acoustic analogy [145,146], or with recent extensions to compressible flow [68] can also be used in aeroacoustic computations. Flows involving shock waves require special attention, and their spatial discretization is discussed in Section 4.4. For linear acoustic problems (not involving interaction of vorticity and or entropy waves) techniques such as the boundary

element method or other integral formulations are an alternative.

We now turn to FD methods, which have been used in the majority of CAA studies. A benefit of the FD schemes is that they are easily extended to high-order-accuracy (albeit on structured grids). Generally, lower-order methods require higher resolution, but fewer operations per node, than higher-order methods. This implies a limit where increasing order-of-accuracy results in less efficient schemes (i.e. ones that cost more for a given error tolerance than lower-order-schemes). However, for unsteady sound generation and propagation problems, where error tolerances must be kept low, it appears that higher-order and optimized methods are nearly always more efficient than lower-order methods. Evidence for this generalization is given in Section 4.1.5.

We briefly review here the derivation of high-order-accurate FD formulas for the first derivative on a uniform mesh. Second derivatives (necessary when viscous terms are retained) are briefly discussed in Section 4.1.6, and non-uniform meshes and generalized coordinate systems are discussed in Section 4.1.7. The independent variable at the nodes is $x_i = h(i - 1)$ for $1 \leqslant i \leqslant N$, and the function values at the nodes are $f_i = f(x_i)$, and the values of the derivative are $f_i' = \frac{\partial f}{\partial x}(x_i)$. First, we write a centered approximation for f_i':

$$\sum_{j=1}^{N_\alpha} \alpha_j(f_{i+j}' + f_{i-j}') + f_i'$$
$$= \frac{1}{h}\left(\sum_{j=1}^{N_a} a_j(f_{i+j} - f_{i-j})\right) + O(h^n). \tag{11}$$

If $N_\alpha = 0$ then the scheme is termed *explicit*. *Implicit* schemes (also Padé or compact FD), by contrast, have $N_\alpha \neq 0$ and require the solution of a system of equations to determine the derivatives of all nodes $1 \leqslant i \leqslant N$ simultaneously. Conventionally, the coefficients α_j and a_j are chosen to give the largest possible exponent, n, in the truncation error, for given stencil width (i.e. choice of N_α and N_a). By Taylor series expansion of Eq. (11), the maximum possible exponent is given by:

$$n_{max} = 2(N_a + N_\alpha), \tag{12}$$

provided that $N_a \geqslant 1$. Table 1 gives coefficients for several centered schemes that have been used in CAA studies.

The leading order term in truncation error in Eq. (11) depends on the choice of coefficients and the $(n + 1)$st derivative of the function f. As it is the leading term in a series, it is a good measure of the actual error only asymptotically for small h, and only when high-order derivatives of the underlying function are continuous. It is possible to look at other measures of the error; of particular interest in CAA are errors in the wave propagation characteristics of a single Fourier

Table 1
Coefficients for conventional explicit (E2,E4,E6) and implicit (C4,C6) centered FD schemes (the number refers to the order of accuracy), as well as the optimized schemes of Tam and Webb [102] (DRP; where $c = 45\pi - 128$) and Lui and Lele [150] (LUI; where the constants are: $\alpha_1 = 0.5381301488732363$, $\alpha_2 = 0.066633190123881123$, $a_1 = 1.367577724399269/2$, $a_2 = 0.8234281701082790/4$, $a_3 = 0.018520783486686603/6$)

Scheme	α_1	α_2	a_1	a_2	a_3	Order (n)
E2	—	—	1/2	—	—	2
E4	—	—	2/3	−1/12	—	4
E6	—	—	3/4	−3/20	1/60	6
C4	1/4	—	3/4	—	—	4
C6	1/3	—	7/9	1/36	—	6
DRP	—	—	$(496 - 15\pi)/42c$	$(1725\pi - 5632)/84c$	$(272 - 85\pi)/14c$	4
LUI			See caption			6

component of f. In fact, it is possible to optimize the coefficients of a FD scheme to reduce such errors, rather than to maximize the formal order of accuracy. These schemes are discussed in Section 4.1.2.

When centered difference schemes are used in hyperbolic systems of linear first-order PDE, it may be shown (see Section 4.1.2) that they disperse, but do not dissipate, the Fourier components of solution. This is an important advantage in turbulence and aeroacoustic computations. Significant dissipation, while helpful in obtaining steady state solutions and capturing shock waves that would otherwise be unresolved on the computational mesh, is deleterious in direct computations of turbulence and acoustic waves, wherein both the phase and amplitude of propagating disturbances are important. The use of dissipative schemes is discussed in greater depth in Sections 4.1.2 and 4.1.3.

4.1.1. Wave propagation characteristics of finite-difference schemes

The wave propagation characteristics of FD schemes gives information about *all* the Fourier components that are supported on the grid. The leading-order truncation error, by contrast, gives only information about the well-resolved components. In this section we derive important wave propagation characteristics for the centered FD schemes discussed in the last section.

Fourier analysis of numerical approximations to PDE dates back to the 1940s and the pioneering work of von Neumann. Analysis of the dispersive and dissipative characteristics of wave solutions to finite-difference approximation of hyperbolic systems have been systematically examined, and particularly good summaries of this work are found in the papers by Trefethen [147] and Vichnevetsky [148]. A limitation of the analysis is that it is strictly correct only when periodic BC are imposed. Parts of the analysis (the discussion on dissipation and dispersion in Section 4.1.2) also require that the governing equations are linear. Nevertheless, the analy-

sis yields an important glimpse at the behavior of FD solutions for more general situations. For example, the stability of a particular scheme (when combined with an appropriate time marching scheme) can be readily analyzed in Fourier space (von Neumann stability) for the linearized problem, and it is often found in practice that the stability limits thus determined continue to be approximately valid when other BC are applied and nonlinear equations are solved.

Consider a periodic domain with N uniformly spaced points on $x \in [0, L]$ (with $h = \frac{L}{N}$). The discrete Fourier transform (DFT) of f (denoted by $\hat{f}$) is:

$$\hat{f}_j = \frac{1}{N} \sum_{m=1}^{N} f_i e^{-ik_j x_m}, \quad j = -N/2, \ldots, N/2 - 1, \qquad (13)$$

where the wavenumber is $k_j = 2\pi j/L$ and $x_m = (m - 1)h$. The inverse transform is

$$f_m = \sum_{j=-N/2}^{N/2-1} \hat{f}_j e^{ik_j x_m}, \quad m = 1, \ldots, N. \qquad (14)$$

It may be shown that the jth component of the DFT of $\frac{\partial f}{\partial x}$, denoted $\hat{f'}_j$ is simply $ik_j \hat{f}_j$. Taking the DFT of Eq. (11) gives the approximate value of $\hat{f'}_j$, which we denote $(\hat{f'}_j)_{fd}$, as:

$$(\hat{f'}_j)_{fd} = iK(k_j h)\hat{f}_j, \qquad (15)$$

where

$$K(z) = \frac{\sum_{n=1}^{N_a} 2a_n \sin(nz)}{1 + \sum_{n=1}^{N_\alpha} 2\alpha_n \cos(nz)} \qquad (16)$$

is the so-called "modified wavenumber." Note that $k_j h$ takes on values between $-\pi$ and π as j varies between $-N/2$ and $N/2$. For $k_j h = \pi$, the period of the wave is $2h$ (and, generally, the number of points per wavelength, N_λ, is $\frac{2\pi}{k_j}$). Higher wavenumbers cannot be represented on the grid, and their energy is aliased onto the resolved wavenumbers.

Modified wavenumber curves are plotted in Fig. 9 for the FD schemes in Table 1. Also plotted is the wavenumber relation for exact differentiation (straight line). The range of wavenumbers over which the modified wavenumber approximates the exact differentiation within a specified error tolerance defines the set of *well-resolved* waves. It is evident that for the same order-of-accuracy, the compact FD schemes have superior modified wavenumbers to explicit schemes. Note that we have plotted Eq. (16) as a continuous relation, $f'(z)$, though it is really only defined at discrete points, $z = k_j h$, $-N/2 \leqslant j \leqslant N/2$, and we have only plotted the relation for positive wavenumbers, since the modified wavenumber for negative wavenumbers is simply its complex conjugate. The error between the exact and modified wavenumber, $\varepsilon(z) = (K(z) - z)/z$ is also plotted in Fig. 9. As the maximum tolerable error is reduced, the low-order schemes require large numbers of grid points per wavelength. Note that in order to gauge the computational efficiency of these schemes, the lower error associated with a higher order scheme must be tempered with their additional computational expense. We examine this issue in Section 4.1.5.

Another issue that arises in using high-order-accurate schemes is the treatment of BC/closures. Here we should distinguish between a BC of the governing equations (which is a statement of the physics of the problem), and a boundary closure, which is a specialized FD formula that is to be applied at boundary or near boundary nodes when the stencil width of the interior scheme is too large to be accommodated on the near boundary points. Ultimately, as discussed in Section 4.1.4, the two conditions are strongly coupled.

Optimized FD schemes: As mentioned above, it is possible to reduce the error in the modified wavenumber, for a fixed stencil size, by choosing coefficients in Eq. (11) for this purpose, rather than maximizing the order of the scheme. Lele [149] constructed such schemes by constraining some of the coefficients in Eq. (11) to achieve a certain truncation error, and then determining the remainder of the coefficients by requiring the modified wavenumber to be equal to exact differentiation at certain wavenumbers. A particular scheme with $N_a = 3$ and $N_\alpha = 2$ was considered that had better resolving power than the tenth order scheme on the same stencil. Tam and Webb [102] derived the so-called "dispersion-relation-preserving" (DRP) schemes (the reason for the name will become clearer in the next section). Their method involves optimizing the coefficients of both the FD approximation to the derivative as well as the coefficients of a Linear Multistep time marching method. Nevertheless, the two optimizations can be considered separately. An explicit FD is used with $N_a = 3$, and two constraints are imposed such that the truncation error is formally fourth order. The additional coefficient is determined by minimizing the integral of ε^2 over $0 \leqslant z \leqslant \pi/2$ with respect to the remaining coefficient. The coefficients for the 7 point DRP scheme are also presented in Table 1 (modified from their decimal format given in [102]), and the modified wavenumber relation was plotted in Fig. 9; evidently the modified wavenumber relation is close to the relation for the 3 point fourth-order compact scheme. Recently, Lui and Lele [150] have employed a compact pentadiagonal ($N_\alpha = 2$, $N_a = 3$) scheme that is sixth order accurate, and which interpolates exact differentiation at $kh = 1.67$ and 2.10, in computations of spatially developing compressible, turbulent mixing layers.

We close this section by noting two schemes that use the standard Taylor series expansion to maximize the order of the scheme on a given stencil, but that vary the standard FD stencil to achieve high-order-accuracy with fewer operations, or with smaller stencil size. Mahesh [151] was able to derive a sixth-order scheme with less dispersive error than the compact scheme fd1.2, by simultaneously solving for the first and second derivative of a function. This is attractive in viscous
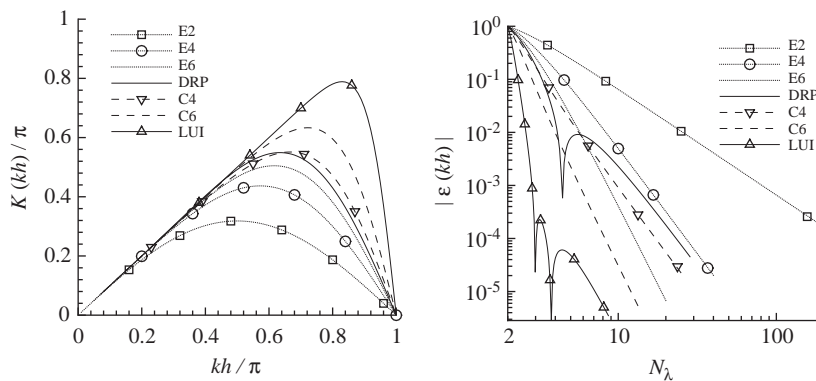

Fig. 9. The modified wavenumber (left) and the relative error between the exact and modified wavenumber (right).

calculations when both derivatives of a certain variable may be needed, and requires fewer operations than two independent evaluations. The second scheme, due to Hixon [152], factors the tridiagonal matrices associated with the fourth and sixth-order compact FD schemes into two separate left-hand side matrix operations that involve bidiagonal matrices. The principal advantage is that for the sixth order scheme, the stencil size is reduced from 5 points to 3, thus requiring only one boundary stencil. Hixon reports that BC implementation is more straightforward because of this. Operation counts are only slightly higher for these factored schemes than the original compact formulations [152].

4.1.2. Dispersion and dissipation

The dispersion and dissipation of Fourier components depends of course on the particular PDE being considered. A simplest example that nevertheless elucidates features of more complicated equations, is the one-dimensional advection equation (first-order wave equation):

$$u_t + cu_x = 0. \tag{17}$$

where c is a constant with units of speed, and the equation represents the advection of u. The exact solution, is $u = u(x - ct)$, where the functional dependence is determined by satisfying appropriate initial and BC. When the one-dimensional Euler equations are linearized about a constant base flow, they can be decoupled into a system of equations of the form of Eq. (17). The details of this transformation are discussed in Section 4.3 below in the context of constructing nonreflecting BC.

On infinite or periodic domains, the solutions of Eq. (17) may be decomposed into their Fourier components in both x and t. That is, we set $u(x,t) = \hat{u}e^{ikx}e^{-i\omega t} + c.c.$ Then nontrivial solutions to Eq. (17) may only be obtained when the dispersion relation:

$$\omega = ck \tag{18}$$

is satisfied. Since all Fourier components of the solution travel with the same constant phase speed, $\frac{\omega}{k} = c$, waveforms comprised of a superposition of modes retain their shape as the propagate, and are therefore called *non-dispersive*.

When the spatial derivative in Eq. (17) is approximated with a FD scheme (but the temporal derivative is treated, for now, as continuous) the dispersion relation for the semi-discrete numerical scheme is modified to:

$$\frac{\omega h}{c} = K(kh). \tag{19}$$

The phase speed of disturbances is now given by:

$$\frac{c_p}{c} = \frac{\omega}{ck} = \frac{K(kh)}{kh} \tag{20}$$

and therefore different Fourier components travel with different phase speed. Such a system is said to be dispersive, as waveforms comprised of a superposition of modes do not retain their identity as the propagate. This dispersive nature of FD approximations has been the subject of many investigations since the work of Trefethen [147] and Vichnevetsky [148]. Groups of waves with Fourier components whose wavenumbers are near k propagate at the group velocity,

$$\frac{c_g}{c} = \frac{1}{c}\frac{\partial \omega}{\partial k} = K'(kh), \tag{21}$$

where the prime denotes differentiation with respect to the argument, kh. Group velocities are presented in Fig. 10 for the FD schemes of Table 1. A common feature of all centered schemes is that for a given frequency, there are two solutions to the dispersion relation, one for long wavelength and the other for short wavelength. For the long wavelength solution, the group velocity is positive. These are well-resolved components of the solution and approach the solution of the original partial differential equations as the grid is refined. We refer to these as *smooth* waves. The short wavelength (poorly-resolved) solution has negative group velocity, counter to the physics of Eq. (17). We refer to these solutions as *spurious* waves, or parasitic solutions. For the second order central FD scheme, the speed of propagation of the spurious waves is equal (but in the opposite direction) to the smooth waves. As the order of the scheme is increased, the speed of propagation of the spurious wave increases.

So far we have only considered in detail centered FD formulas for which the function $K(kh)$ is real for real wavenumbers. This leads to dispersion of waveforms, but the amplitude of each Fourier component remains
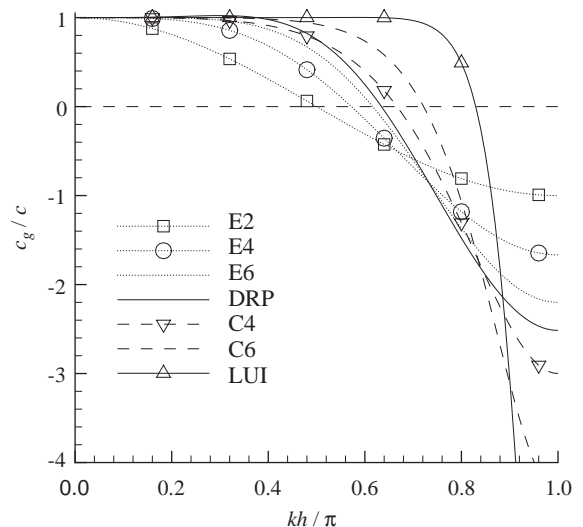

Fig. 10. The group velocity for several FD schemes.

constant. As noted above, when asymmetric stencils are used, the wavenumber is complex. For the model Eq. (17), this results in complex frequencies that will cause disturbances to be either exponentially attenuated (e.g. dissipate), when the imaginary part of $K(kh)$ is positive, or grow exponentially, when the imaginary part is negative. It is therefore necessary for stability that the scheme be dissipative for all kh. Given that the sign of the dissipation also depends on the value of c in Eq. (17), some form of *flux splitting* is usually used for systems of equations that have eigenvalues of both signs.

Various upwind schemes have been considered for CAA applications (e.g. [153,154]). A drawback of upwind schemes is that there is significant dissipation of the highest resolved wavenumbers that. The magnitude of this dissipation can only be reduced by increasing the stencil size. Here one can optimize some of the coefficients to achieve the desired level of attenuation, rather than to maximize the truncation error of the scheme [154]. When some dissipation is desired (e.g. for smoothing shock waves, stabilizing/ smoothing marginally resolved computations, etc.) it is also possible to explicitly add a dissipative term to the governing equations. Such "artificial viscosity" schemes are discussed in the next section.

4.1.3. Spurious waves, artificial viscosity, and filtering

As discussed in Section 4.1.2, centered FD schemes yield two solutions for the wavenumber for a given frequency: the small wavenumber *smooth* solution has propagation characteristics similar to the underlying PDE, while the high wavenumber (near π) *spurious* solution propagates with a group velocity of the wrong sign. In physical space, the spurious wave has a sawtooth appearance, since the Fourier component varies rapidly from grid point to grid point. These spurious waves are ubiquitous in FD solutions, and CFD practitioners have given them different colorful names: wiggles, hash, parasites, 2-Δ waves, sawtooth waves, or error waves.

Spurious waves may be produced in several ways:

1. *Initial conditions* (*IC*): In order to be free of spurious waves (in the absence of dissipation), the Fourier transform of the IC must be free of energy at wavenumbers $kh > k_c h$. This situation should be contrasted to the typical approach in steady-flow CFD of prescribing a crude (and possibly discontinuous) IC that is *relaxed* to steady-state in a highly damped nonphysical process. Aside from starting with an exact solution of the governing equations (which is rarely possible) techniques to minimize initial transients are problem specific. For simple flows (vortices, vortex rings, etc.), an approximate steady laminar solution can often be found, and for transitional thin shear layers, a converged solution to the steady boundary layer equations is appropriate. Even with an IC that is *relatively close* to an exact solution, acoustic transients can have much smaller wavelength and higher amplitude than the physical radiation. Compounding this problem is that the computational mesh will usually be optimized for the physical (non-transient) solution, for example relying on a large stretching to accommodate the long acoustic wavelength in low Mach number flows. Aside from constructing an initial condition that is closer to an exact solution, there are a few techniques that can be used to reduce large transients. Filtering of the field at strategic points in time during the transient may effectively remove poorly resolved waves, and it would be possible as well to use artificial viscosity during an initial stage of the computation, gradually reducing the viscosity to zero once the transients have been sufficiently attenuated.

2. *Nonlinear cascade to small scales in DNS and LES*: Nonlinearity will obviously couple the (linear) smooth and spurious solutions. Nonlinear cascading of energy to smaller scales is a feature of turbulent flow. Ideally, in a well-resolved DNS calculation, physical viscosity should be the only mechanism that supplies dissipation to the small scales. The presence of spurious waves in DNS calculations, therefore, is an indication of poor resolution. While artificial dissipation can be used to eliminate them, it imposes, in essence, a grid-dependent turbulence model. For LES, the effects of spurious waves are not well understood at present. Typically, the "resolved" part of the energy spectrum is defined to be all $kh < \pi$, and the information from all these scales is used to determine the magnitude of subgrid-scale dissipation. An interesting analysis of the problem is presented by Ghosal [155].

3. *Shock waves and nonlinear steepening of waves*: Since the internal structure of shocks is governed by viscous effects, this is in fact really the same issue as the nonlinear cascade. However, strong shock waves are so thin (order of several molecular mean-free paths) that it is not realistic to resolve them in a calculation. Instead, a variety of sophisticated numerical techniques can be used to allow steep gradients while minimizing the generation of oscillations (Gibbs Phenomena). A survey of some preferred methods for handling shock waves is discussed in Section 4.4.

4. *Propagation of waves through grid stretching*, *generalized coordinates*, *and/or overset grids*: The smooth-spurious wave solutions are coupled in regions of grid stretching [156]; further analysis of this phenomenon is given in Section 4.1.7. Spurious wave production by overset grids is discussed below.

5. *Boundary conditions*: Even sophisticated nonreflecting and radiation BC can strongly couple the physical and spurious solutions [157,158]. This coupling is

often the strongest source of spurious waves in a calculation. See Sections 4.1.4 and 4.3.1 for further details.

With the exception of coupling by boundary closures, it should be noted that spurious waves arise due to insufficient resolution of relevant lengthscales in a given problem. In linear, constant coefficient problems, where the relevant lengthscales are determined solely by initial and BC, smoothing of spurious waves (by artificial dissipation, artificial viscosity, or filtering) is only *cosmetic*, as it simply changes the nature of the error for the poorly resolved components from dispersive to dissipative. As the problem is linear, the solution at the resolved scales is unaffected by the presence of errors of either type.

For nonlinear problems, smoothing amounts to an ad hoc. turbulence model or shock smoothing scheme. Practically, spurious waves are often associated with nonlinear instabilities that can lead to failure of the solution. If spurious oscillations grow until they produce a negative pressure, density or temperature, the numerical solution will fail.

If spurious waves cannot be reduced by using higher-order schemes or more grid points, they can be attenuated by artificial dissipation (i.e. using upwind biased schemes that were discussed in Section 4.1.2), by adding an artificial viscosity term to the governing equations, or by directly filtering them from the solution. These methods can serve as a (relatively crude) method of shock capturing, for which the ENO and Weighted-ENO type schemes discussed later in Section 4.4 are generally superior. Aside from shock capturing, artificial dissipation, viscosity, and filtering may be used for "production" codes in order to given them some measure of robustness. By robust, we mean algorithms that, given insufficient mesh spacing or other limitations, merely return poor quality (but smooth) answers rather than failing spectacularly. On the other hand, at least failure requires the user to stand back and wonder what went wrong, and, hopefully, refrain from using the results for design. The bottom line is that users must be more cautious in interpreting the results from codes that involve artificial dissipation, viscosity, or filtering.

Artificial viscosity schemes are numerous, and texts and review articles on CFD should be consulted for a complete literature survey. Second-order schemes that have been optimized for CAA applications have been discussed by Tam et al. [159]. Here FD formulas are optimized to generate a specific damping as a function of wavenumber so as to have relatively smaller impact on the well-resolved waves, say $kh < 1$. The analysis follows analogously to the analysis for optimizing FD formulas for the first derivative evaluation. It should be recognized that the order of the viscosity that is added effects the convergence of the scheme to the exact solution. One

must be careful to balance the artificial viscosity error with the finite-difference truncation error.

An example of proper balancing of artificial viscosity and truncation error is given by Barone and Lele [41]. As discussed earlier severe numerical challenges are faced when high-resolution schemes (such as CD6) are applied to problems where simple mapped cartesian or other simple grids are insufficient, such as in aerodynamic flows about surfaces with relative sharp leading or trailing-edges. One way of dealing with this situation is to use an overset mesh technique where a body-fitted mesh wrapped around a surface is overlaid on another background mesh. High-order interpolation between them is necessary to maintain a high quality solution. However, mesh discontinuities can trigger a weak-instability in the solution. A way of controlling this [41] is to add a scaled hyperviscosity term to the governing equations. The idea is to select the coefficient and the order of the hyperviscosity in a way to achieve a balance between the (dispersive) truncation errors already present in the solution and a dissipative error of the same asymptotic order and magnitude for the ill-resolved wave-components. Fourier analysis of test problems allows the coefficient (of hyperviscosity) to be selected. Tests on model problems and realistic nonlinear problems [250] show the effectiveness of the technique. Generally speaking this method required less 'damping' than Tam and Dong's artificial selective damping. The notion of using a scaled amount of hyperviscosity may also be useful in the LES context.

Explicit filtering of the dependent variables has also been used to attenuate spurious waves. For non-periodic coordinates, these filters are usually applied discretely with FD formulas (e.g. [160,161]). Such filters do not have a sharp spectral cutoff, but rather continuously vary from 1 to 0 over the range of wavenumbers $0 < kh < \pi/2$. Lele [149] derived a hierarchy of compact filters that are superior to explicit formulas of the same stencil width (by superior we mean they more closely approximate sharp spectral cutoff). Optimized filtering schemes were also considered where higher order-of-accuracy is sacrificed in order to give sharper spectral cutoff.

Gaitonde and Visbal [162,163] have presented a useful set of numerical experiments that demonstrate the use of compact and explicit filters on high-order accurate FD solution of model problems. In particular, they consider both multi-domain and generalized coordinate implementation of their schemes.

In summary, artificial dissipation, artificial viscosity, and filtering of the dependent variables may all be used to suppress instabilities associated with the growth of spurious waves. It was stressed that in nonlinear calculations, such schemes amount to ad hoc turbulence models or shock-capturing schemes. It is preferable to

use mesh refinement, higher-quality grids, and higher-quality BC as a first line of attack.

4.1.4. Boundary closures

The FD equations presented in Section 4.1 can only be applied at nodes separated by $\max(N_a, N_\alpha)$ points from the boundary. In order to compute the derivatives near the boundary, thereby closing the set of discrete equations to be advanced to the next timestep, specialized formulas have been derived for the boundary and near-boundary nodes (e.g. [149,102]).

It should be recognized at the outset that boundary closures for FD schemes are intimately related to the physical BC to be posed on a problem. Many of the methods that have been proposed for CAA have overlooked this connection, essentially breaking the problem into two independent pieces. First, specialized upwind/downwind schemes for the boundary and near boundary nodes are derived. Second, any derivatives normal to the boundary that appear in the (continuous) BC are replaced with one-sided differences. Near-boundary nodes are treated with the interior equations and derivatives are approximated with one-sided or biased schemes.

This "decoupling" approach to BC and boundary closures can lead to instability. As discussed by Carpenter et al. [164] there are two important types of stability. The first (Lax stability) determines whether the solution remains bounded as the mesh size $\Delta x \to 0$ at a fixed time, and the second is that the error does not grow without bound in time. The G–K–S theory [165] shows how Lax stability can be analyzed in terms of normal modes on semi-infinite or finite domains. Requiring that the error does not grow without bound in time requires asymptotic stability, which for the semi-discrete case implies that there can be no eigenvalues of the spatial discretization operator in the right half of the complex plane (or on the imaginary axis in the degenerate case). Carpenter et al. [166] have stressed the desirability of having schemes that are both Lax and asymptotically stable.

In the context of Eq. (17), it is not difficult to derive boundary closures and check a posteriori for asymptotic stability (e.g. [149,152]). Generally, eigenvalues must be determined numerically, for a specified grid size, but it is straightforward to examine several cases and extrapolate if needed to larger grids. Such analyses show that it becomes difficult to find stable closures unless accuracy is sacrificed at the boundary. While it is desirable to maintain high accuracy near the boundaries, boundary closures applied to more complex equations are usually combined with other approximations to the continuous BC such as those discussed in Section 4.3. Given this, the order of accuracy near the boundaries is not as important as stability and related conservation properties.

Stable closures (both Lax and asymptotic) have been constructed for compact FD methods by requiring that the discrete approximation admit a summation-by-parts (SBP) formula [166–168]. The stability requirement is reduced to a set of algebraic constraints on the coefficients of the boundary or near-boundary FD formulas. The method requires that the BC be posed using the *simultaneous approximation term* (SAT) method, which amounts to enforcing the BC nonlocally in space. Abarbanel et al. [167] have generalized this approach and stability has been proven for multidimensional scalar equations and, under certain conditions, systems of one-dimensional equations. On the other hand, more general equations were tested a posteriori in [168], including the multidimensional Maxwell equations with good results and no apparent instability. Carpenter et al. [169] have used the SAT/SBP schemes to impose conditions at interfaces between subdomains. Generalizations include one-dimensional systems of *nonlinear* equations [170] and generalized curvilinear coordinates for multidimensional, scalar, linear hyperbolic equations [171]. Further generalization is no doubt possible, and should include consideration of more accurate BC for multidimensional flows.

Alternative stable closures for FD schemes have recently been developed by Hagstrom [172]. He attributes instability associated with boundary closures with the Runge phenomena (large oscillations in interpolating polynomials near the boundaries of evenly spaced grids). He demonstrates that clustering of grid points near boundaries can eliminate instabilities associated with high-order one-sided difference closures. Chebyshev clustering, for example, yield stable schemes butt gave rise to undesirable CFL stability constraints. Nodes associated with a recently developed hybrid Gauss-Trapezoidal quadrature scheme [173], which relax to an evenly spaced grid in the interior, however, appear to give both stability and computational efficiency.

Finally, alternative approach to the boundary closure/stability problem follows from a consideration of the dispersive properties of finite-difference approximations [147]. The resulting boundary closures are termed *discretely nonreflecting BC* and are discussed in Section 4.3.1.

4.1.5. Computational efficiency

As noted above, high-order and optimized FD schemes provide lower error, across all scales supported by the mesh, than conventional low-order methods. However, their increased accuracy must also be weighed against the increased number of computations per node. Unfortunately, due to the large computational effort involved, no conclusive comparisons have been made for full-scale problems of sound generation or propagation. Even for simple model problems, few comparisons of

actual performance have been provided in the literature; a recent paper by Zingg [174] provides a useful comparison for a model electromagnetic scattering problem. In this section we make a relatively simple comparison that should nevertheless provide a rough measure of the relative efficiency of various schemes.

While the error in a solution may be measured in various ways (e.g. phase error, amplitude error, overall error in various norms), we choose here to examine the error in modified wavenumber (plotted for different schemes in Fig. 9). As discussed above, the wavenumber is proportional to N_λ, the number of nodes per wavelength. When scaled with the computational cost per node, N_λ is thus a measure of the total "cost" of a computing a derivative for a particular wavelength. Except for pathological cases, one would then expect any measure of the overall error in a particular problem to be a weighted integral over the error at individual wavelengths.

Measuring the cost per node is not without ambiguity as it depends on the architecture of the computer, the optimization level of the compiler, the skill of the programmer, etc. In order to partially account for this, we have performed two measurements. The first is simply the operation count for a specific scheme, i.e. the number of floating point addition and subtractions plus the number of multiplies.[4] We assume, as is usually the case, that multiplies and adds require roughly equivalent CPU time. In counting operations, we have used the most efficient algorithms known to us. For compact schemes, for example, this involves computing an LDU factorization of the left-hand-side tridiagonal matrix *once* at the beginning of the program, and we do not consider this as part of the cost of evaluating a derivative (that would be performed thousands of times in a given run). The second measurement is the actual cost of a program written by the authors and run on a 400 MHz Pentium II PC. In measuring the CPU time, the size of the arrays and several other programming constructs were varied in the experiment; these had minor effects on the timings, but over a range of conditions, the cost as measured by CPU time was roughly equivalent to the cost estimated with operation counts. Therefore in what follows we use cost measured by operation count.

In order to fairly compare different schemes, we must also account for the impact of the spatial discretization on the *time step* that can be used. For this we assume that the time step is limited by a Courant constraint for both accuracy and stability. In that case, the time step scales directly with the grid spacing, with a scaling factor that depends on the accuracy of the particular scheme. The stability characteristics of FD schemes are discussed

in more detail in Section 4.2, but we note here that the Courant constraint is governed by *the maximum value of the modified wavenumber*. Let us call this value $K_{\max}$. Then the total cost of a given scheme is

$$\text{Cost} \propto N_{\text{op}} N_\lambda^2 K_{\max} \tag{22}$$

per unit physical time of the simulation.

In Fig. 11, we show the error in the modified wavenumber (absolute value), versus the estimated cost for several explicit, compact, and optimized FD schemes. In Table 2 we present values of the operation counts, N_{op} and $K_{\max}$, as well as CPU times per node per derivative evaluation (using the program discussed above) for the different schemes.

A word of explanation is in order with regard to how the optimized FD schemes have been plotted. Optimized finite difference schemes have modified wavenumbers that can be both larger and smaller than exact differentiation. Thus the error crosses through zero at certain wavenumbers (this causes the dips in the curves seen in Fig. 9). These dips could give the false impression of a lower error than would actually be obtained, since for a given number of points per wavelength within the dip, there is actually greater error for more well resolved waves. In realistic problems, a *range* of scales are involved. Therefore for a given cost, we plot the maximum value of the error in modified wavenumber for all costs greater than the given cost (in other words we remove the dips from the curves). This gives a more realistic measure of the actual error in practical problems.

Using the figure, we can ascertain which scheme has the lowest error for a given cost, and how many grid points per wavelength should be used with that scheme in order to achieve that accuracy and cost. Conversely, for a given error tolerance, the plot shows which scheme has the lowest cost (and, again, how many points per wavelength are needed for that accuracy and cost). For example, for a normalized cost of 1, the lowest error is obtained with the explicit finite-difference scheme using about 5 points per wavelength. The error level, however, is almost 30%, which is obviously too large. As a second example, if the error tolerance is 1%, than the scheme with lowest cost is the DRP scheme, again using a minimum of about 5 points per wavelength.

Several conclusions can be drawn from the figure. For error levels around 1%, nearly all of the schemes considered here are of comparable cost, differing by at most a factor of 2 (the explicit second order scheme is the exception, being more costly by a factor of 4 than the most efficient scheme). For errors smaller than about 1%, the optimized pentadiagonal scheme of Lui and Lele is the most efficient, despite the fact that it has (by far) the highest operation count and requires the smallest time step since it has the largest value of $K_{\max}$. The reason for this is that high accuracy is obtained with

---

[4]By precomputing reciprocals of coefficients, all schemes can be implemented without any divide operations.
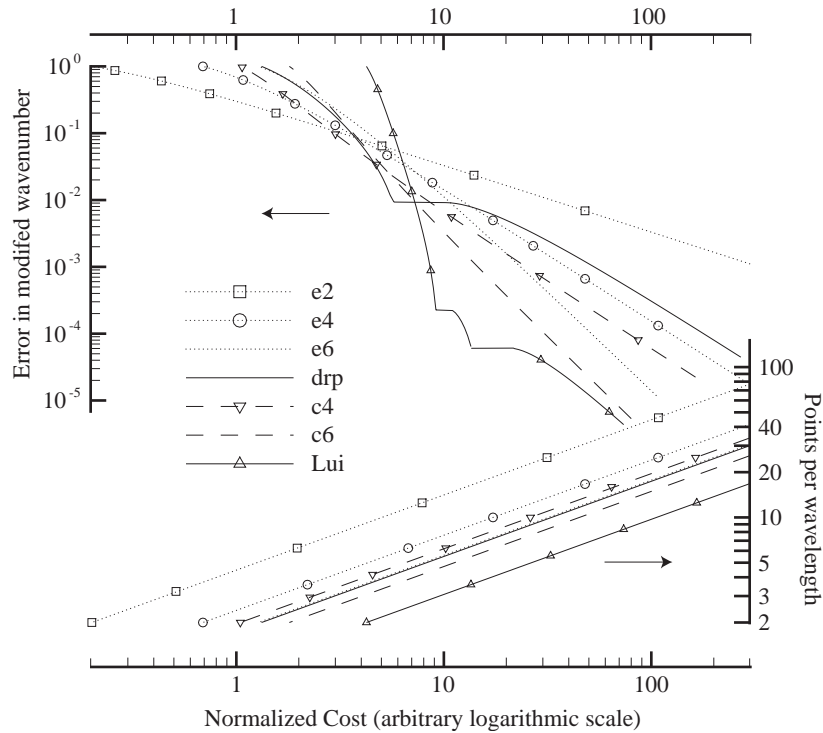
Fig. 11. The relative error in modified wavenumber and number of grid points required per wavelength, as a function of the normalized cost of computing a unit of physical time.

Table 2
Cost data for several FD schemes

Scheme	Adds	Multiplies	N_{op}	Measured CPU	K_{max}
E2	1	1	2	1.0	1.00
E4	3	2	5	1.6	1.37
E6	5	3	8	2.2	1.59
DRP	5	3	8	2.2	1.64
C4	3	3	6	2.8	1.73
C6	5	4	9	3.5	1.99
LUI	9	8	17	5.4	2.47

Note that the measured CPU has been normalized by the CPU time for the scheme e2.

as few as 3 points per wavelength. In general, it appears that optimization of schemes is useful from the point of view of efficiency.

There are several other factors that impact the choice of a differencing scheme. First, the cost we measured does not take into account issues related to storage. This may be relevant because for a given cost, two schemes with the same accuracy do not have the same number of grid points. This would shift preference toward the more accurate scheme. On the other hand, there can be some penalty associated with the compact methods when

codes are to be run in parallel. Finally, the error in a particular calculation will be a weighted integral of the errors at individual wavenumbers, the weighting being dependent on the particular problem; it is not difficult to imagine situations where the crossover point in efficiency between different methods would shift somewhat to the left or right.

4.1.6. Viscous and second-derivative terms

Second derivatives of the primitive variables appear in the viscous equations, and second derivative approximations of explicit, compact, and optimized types can be derived in an analogous manner to the first derivative discussed in Section 4.1. Some optimized schemes for the second derivative are reported by Lele [149]. The modified wavenumber concept can also be applied to such schemes, and the dissipative properties can be understood by examining a simple diffusion model problem:

$$u_t = vu_{xx}. \tag{23}$$

If centered second derivative schemes are used, then the modified wavenumbers will be purely real and negative (zero for zero wavenumber), corresponding to damping of a particular (nonzero) wavenumber. That is, they do not cause any dispersion.

The viscous terms in the equations could in principle also be computed by two applications of a first derivative scheme, but this would provide no diffusion for the highest wavenumbers, since the modified wavenumber for the first derivative goes to zero at $kh = \pi$. This would be unsatisfactory in DNS, where physical viscosity is the only mechanism available to damp the smallest scales. Thus, it is preferable to write as many viscous terms as possible as second derivatives, and directly apply second derivative FD schemes to compute those terms. When the viscosity is a function of temperature, second derivatives can be obtained by applying the chain rule. Aside from providing damping to the highest wavenumbers the second-derivative operators generally have better modified wavenumber characteristics than two applications of first derivatives.

4.1.7. Grid stretching and generalized curvilinear coordinates

Most flows of practical interest make use of nonuniform meshes, either because it is dictated by the shape of solid boundaries, or because it is desirable to have greater resolution in a particular region. For finite-difference schemes, these can take the form of stretched Cartesian meshes, generalized coordinate systems, and, most generally, overlapping combinations of such grids. In problems with moving boundaries, these grids may also be time-dependent. Even for free space problems, stretched meshes are usually used. A typical example is when a portion of the far acoustic field is to be computed together with the source region at low Mach number. Then nonuniform meshes allow a much coarser resolution in the acoustic field where the wavelength is large compared to the spatial scales in the source region. Grids that are as close to orthogonal and uniform as possible lead to the best results. Several general "rules of thumb" (e.g. [175]) that are commonly cited are that (i) grid stretching formally reduces the order of accuracy (in one dimension) by one order, (ii) grid spacing should vary slowly along a coordinate direction, thus minimizing the degradation of the truncation error; (ii) for non-orthogonal meshes, the angle between grid lines in any cell should be as close to normal as possible, and (iii) the aspect ratio of the cells should be close to unity to minimize the degradation of the truncation error.

However, there are more subtle issues that arise in how to best evaluate the grid transformation parameters (metrics). The accuracy, stability, computational expense, and shock capturing properties of schemes are modified depending on the form in which the equations in curvilinear coordinates are written (i.e. strong conservation form, weak conservation form, chain-rule form, etc.). Early work [176–178] identified certain problems with the strong conservation form, such as Galilean invariance of the discrete approximation, and stressed the desirability of evaluating metrics with

finite-difference/finite-volume formulas rather than prescribing them analytically. In order to obtain freestream preservation, certain averaging of the grid metrics is needed. Thomas and Lombard [179] employed a strong conservation form of the equations, but avoided the averaging of the grid metrics by deriving alternative (equivalent) forms for the grid metrics prior to discretization. Their method has been used in the high-order-accurate generalized coordinate CAA code developed by Gaitonde and Visbal [163], and recently extended to moving curvilinear grids by Hixon [152].

Even when smooth grids are used, the dispersion and dissipation properties of the finite difference schemes on curvilinear coordinates are altered from those on a uniform mesh. Fourier analysis does not apply directly to stretched meshes, since grid metrics appear in the governing equations as non-constant coefficients (such that the Fourier transform cannot be taken directly). However, if the coefficients are slowly varying, compared to the wavelength, then standard methods for dispersive PDE (e.g. [180]) may be applied. Trefethen [147] has performed such an analysis, and applied the results to several low-order schemes. In particular, he examined how grid stretching, grid interfaces, anisotropy, and non-constant coefficients affect the accuracy of wave propagation and generation of spurious waves. Here we extend Trefethen's analysis to the higher-order schemes of interest in CAA, and discuss some results that are of consequence for aeroacoustic calculations.

We again focus our attention on the simple advection equation, this time in multiple dimensions:

$$\frac{\partial u}{\partial t} + U_j(\mathbf{x})\frac{\partial u}{\partial x_j} = 0, \tag{24}$$

where U_j is a spatially nonuniform advection velocity, and summation is implied by the repeated index, with j running from 1 to n where n is the number of spatial dimensions. Eq. (24) is to be solved on a stretched mesh in $\mathbf{x}$, where $\mathbf{x} = \mathbf{x}(\xi)$, where ξ is a uniform grid in n dimensions. Without loss of generality, the uniform grid is assumed to have equal spacing, h, in all three coordinates, and in what follows we assume that coordinate variables $\mathbf{x}$ and ξ, and wavenumbers, $\mathbf{k}$ have been normalized by h and $1/h$, respectively. Using the chain-rule in Eq. (24) yields:

$$\frac{\partial u}{\partial t} + \alpha_j(\xi)\frac{\partial u}{\partial \xi_j} = 0, \tag{25}$$

where we have now set $\alpha_j = U_i \frac{\partial \xi_j}{\partial x_i}$.

We use a centered finite-difference scheme to discretize $\frac{\partial u}{\partial \xi_j}$ on the uniform mesh. The grid metrics in $\boldsymbol{\alpha}$ may also be discretized, and, together with the base flow,

U, we assume that they are slowly varying in space.[5] Now, since only odd derivatives appear in the Taylor series expansion of centered finite-differences, Eq. (25) may be rewritten as

$$\frac{\partial u}{\partial t} + \alpha_j \sum_{m=0}^{\infty} c_m \frac{\partial^{2m+1} u}{\partial \xi_j^{2m+1}} = 0, \tag{26}$$

The slowly varying coefficients, α_j, allow an asymptotic solution whose first term is of the form:

$$u(\xi, t) = e^{i\theta(\xi, t)} A(\xi, t), \tag{27}$$

where θ and A are slowly varying functions of ξ and t. The local wavenumber, frequency, and their consistency relation are then

$$k_j = \frac{\partial \theta}{\partial \xi_j}, \quad \omega = -\frac{\partial \theta}{\partial t} \quad \text{and} \quad \frac{\partial k_j}{\partial t} - \frac{\partial \omega}{\partial \xi_j} = 0. \tag{28}$$

Using Eq. (27) in Eq. (26) and retaining the lowest order terms yields the dispersion relation:

$$\omega(\xi, t) = \alpha_j(\xi) \sum_{m=0}^{\infty} c_m (-1)^m k_j^{2m+1} = \alpha_j(\xi) K(k_j), \tag{29}$$

where $K(k_j)$ is the same modified wavenumber function discussed above in Section 4.1.2. Using the consistency relation, we may solve for the frequency, wavenumber, and amplitude of waves by integrating the equations along characteristics:

$$\frac{d\xi_j}{dt} = C_j$$

$$C_j = \alpha_i(\xi) \frac{\partial K(k_i)}{\partial k_j} = \alpha_j(\xi) K'(k_j) \quad \text{(no summation).} \tag{30}$$

where C_j is the (vector) group velocity. Along the characteristics, we also have

$$\frac{d\omega}{dt} = 0 \quad \frac{dk_j}{dt} = -K(k_i) \frac{\partial \alpha_i}{\partial \xi_j} \quad \frac{d|A|^2}{dt} = -|A|^2 \frac{\partial C_j}{\partial \xi_j}, \tag{31}$$

where the amplitude equation follows by carrying the high frequency analysis to the next order. These are ray-tracing equations that can be solved numerically to determine the dispersion characteristics of a general grid and general nonuniform advection velocity.

It is interesting to note several general features of the equations. First, the effects of the grid metrics and non-uniform velocities are lumped together in $\boldsymbol{\alpha}$. If $\boldsymbol{\alpha}$ does not vary with ξ (when velocities are uniform and there is no curvature in the mapped coordinate), then **k** is constant along characteristics, and the group velocity is constant (wave packets travel at constant speed). Thus even skewed non-orthogonal meshes lead to similar wave propagation characteristics as Cartesian meshes (see the discussion of anisotropy below), so long as the grid spacing is constant.

In the next two sections we examine two limiting cases where analytical solutions of these equations may be found directly.

Stretched Cartesian meshes: Here we examine stretched Cartesian meshes, where each component of the mapped grid **x** is only a function of a single component of the uniform grid, ξ. We further restrict our attention to waves propagating in a direction aligned with one of the coordinates. Anisotropy, which arises when the waves do not propagate in a coordinate direction, is analyzed separately below. Under these circumstances k and ξ are scalars, and one obtains

$$\alpha(\xi) K(k) = \text{constant along characteristics.} \tag{32}$$

Thus given the initial wavenumber and location of a group of waves, Eq. (32) gives its trajectory in (k, ξ) space.

For small k, $K(k) \to k$ since differentiation becomes exact in the limit of $k \to 0$. Thus for small k, Eq. (32) shows that $k\alpha(\xi)$ is constant along the characteristic, and since $C \to 1$ as $k \to 0$, the characteristics are straight lines. Thus the well resolved waves move through the mesh without dispersion, and the wavenumbers change with the mesh spacing such that the wavenumber in the physical coordinate is constant. These properties are those of the original non-dispersive equation (24), and are thus required for consistency of the finite difference approximation.

However, when k is not small, the behavior of the waves is different. Consider a wavenumber k_0 that is initially at a position ξ_0. The evolution of the wavenumber is given by:

$$K(k) = K(k_0) \frac{\alpha(\xi_0)}{\alpha(\xi)}, \tag{33}$$

There are no solutions to the left-hand side with real k when $K(k) > K_c$, where K_c is the maximum modified wavenumber (see Fig. 9). Such waves are cutoff and cannot be transmitted through the grid stretching. Setting $K(k) = K_c$, and solving for $K(k)$, we find that the transmitted waves at any location are those for which

$$K(k_0) < K_c \frac{\alpha(\xi)}{\alpha(\xi_0)}. \tag{34}$$

For a grid stretching that transitions between a region of fine uniform mesh and a coarse uniform mesh, then for large ξ, the ratio $\frac{\alpha(\xi_0)}{\alpha(\xi)}$ gives the final mesh spacing to the original mesh spacing, which we denote here as R. Thus the transmitted waves are those for which $K(k_0) < \frac{K_c}{R}$, and *the range of transmitted waves depends on the particular finite-difference scheme used.* For second-order finite differences, $K(k) = \sin k$, and $K_c = 1$, $k_c = \frac{\pi}{2}$. Thus

---

[5] In this case, any truncation error associated with the finite differencing of grid metrics will be small compared to the truncation error associated with $\frac{\partial u}{\partial \xi}$, and it is irrelevant whether these terms are differentiated numerically or analytically.

only waves with $K(k) < 1/R$, can be transmitted. For example, if $R = 2$, those waves with $k_c < \pi/6$, or $N_\lambda > 12$ are transmitted. That is, all waves with fewer than 12 points per wavelength are reflected, no matter how slowly varying the transition between the two grid spacings. For the sixth-order compact scheme, a similar argument shows that all waves with fewer than 6 points per wavelength are reflected.

Since any $K(k_0)$ corresponds to two real wavenumbers, k, there are two sets of waves that are transmitted through the mesh stretching: a set of waves for small k, which have $C > 0$ and propagate in the correct direction, and the spurious waves on the coarser mesh with $C < 0$ and propagate through the mesh in the negative direction. All other smooth waves on the fine mesh are *reflected* back as spurious waves on the fine mesh. The reflection of different wavenumbers is depicted schematically in Fig. 12. The lines plotted in the (k, ξ) plane are the characteristics.

The transmission/reflection of waves is similar, but reversed in sense, when the mesh transition is coarse to fine. Then $R < 1$. The diagram in Fig. 12 represents this situation if the direction of the arrow is simply reversed. All of smooth waves (running to the left in the figure) on the coarse mesh are transmitted to the fine mesh. A portion of the parasitic waves (moving now to the right on the figure), those with $K(k) < RK_c$, on the fine mesh are transmitted to the coarse mesh, while the remainder of the parasitic waves are reflected back on the fine mesh as "smooth" waves. Note that smooth refers to the labeling of the waves as having $C > 0$ or $C < 0$. The reflected "smooth" waves actually have relatively few points per wavelength and do not look smooth when plotted.

While R controls the portion of waves that are reflected, the analysis also shows that $|A|^2 \alpha$ is constant along characteristics. While waves with different wave-length are reflected from the mesh transition with different speed, their amplitude is invariant to the details of the mesh transition since $\alpha(\xi)$ returns to its original value. That is, the total *wave action*, when integrated over the physical wavenumber, $\theta_x = \theta_\xi \alpha$ is constant. Smooth mesh transitions lead to a longer duration, lower amplitude reflection, while abrupt transitions lead to a shorter duration, higher amplitude reflection. The total reflected energy is *only a function of R*, not the smoothness of the mesh transition.

Anisotropy: Wave propagation in multidimensional calculations is anisotropic, as well as dispersive. That is, even when the underlying PDE corresponds to isotropic wave propagation (i.e. with phase speed independent of the direction of wavefronts), the phase speed (and group velocity) of the discrete solutions will depend on the angle of propagation. For anisotropic PDE, the finite-difference solution will alter the directions of propagation differently for different angles. This occurs for two reasons: first, wavefronts are not necessarily aligned with coordinate directions, and second, the grid spacing need not be equal in different coordinate directions.

As the simplest example, consider two-dimensional advection described by Eq. (24), in an arbitrary direction, θ, with $(U_1, U_2) = (U\cos\theta, U\sin\theta)$, on a uniform mesh with unequal mesh spacing in the two coordinate directions. The equations are nondimensionalized with the grid spacing in x_1, and the ratio of the grid spacing in x_2 to x_1 is denoted by r. We integrate Eq. (31) analytically for waves whose initial wavenumbers are $(k_1, k_2) = k\cos\theta, k\sin\theta$.

The error in propagation can again be assessed in terms of modified wavenumber, phase speed and group velocity of the disturbances. For example, the phase speed is given by:

$$\frac{c_p}{U} = \frac{K(k\cos\theta) + rK(\frac{k\sin\theta}{r})}{k}, \tag{35}$$

Eq. (35) is shown graphically in Fig. 13 and was also considered by Lele [149]. For each curve in the plots, the radial distance from the origin at an angle θ represents $\frac{c_p}{c}$ for waves propagating in that direction. The different curves represent differing numbers of grid-points per wavelength, holding r constant, for the fourth-order compact and second-order explicit schemes, respectively. Significant anisotropy is evident for the fourth-order scheme only when there are 3 or fewer grid points per wavelength. By contrast the explicit second order scheme remains significantly anisotropic for as many as 10 points per wavelength. When $r = 1$, the least error occurs in the $\pm\frac{\pi}{4}$ directions. Changing r has the obvious effect of improving (worsening) the anisotropy for waves at angles near $\pm\frac{\pi}{2}$ as r is increased (decreased) from 1, while having no effect on the waves propagating at angles near $\theta = 0, \pi$.
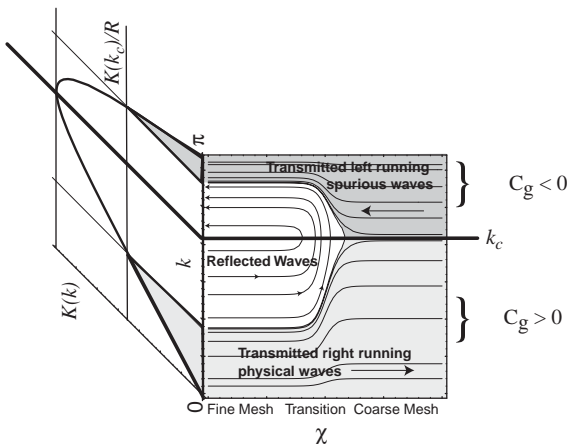

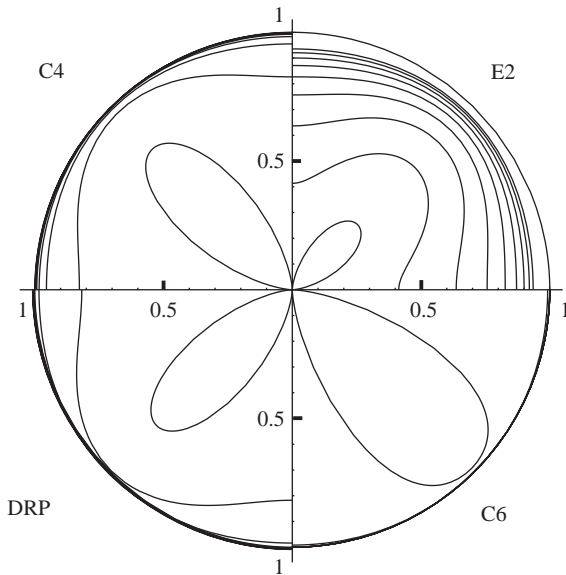Fig. 12. Schematic diagram depicting the reflection of waves on a stretched mesh.

Fig. 13. Anisotropy in 4 different finite difference schemes from Table 1. For each scheme, the distance from the origin represents the phase speed for waves propagating at the particular angle shown. Note that each scheme has a two-fold symmetry, such that the anisotropy is equivalent for angles $\theta + n\pi/2$, $n = 1, 2, \ldots$. There are 10 curves plotted for each scheme corresponding to $2, 3, \ldots, 10$, and an infinite number of grid points per wavelength.

4.2. Temporal discretization

The choice of time marching scheme is as important in preserving accurate wave propagation characteristics, and unsteady flow features in general, as is the choice of spatial discretization. In general, there are two approaches that are used to discretize the equations in time. In splitting the discussion of spatial and temporal discretization into two parts, we have tacitly assumed that we are following the so-called "semi-discrete" formulation wherein the equations are first discretized in space to produce a (large) system of nonlinear ODEs. Of course, it is also possible to proceed directly to discrete equations in both space and time, as well as "mixing" spatial and temporal discretization. An example is the Lax–Wendroff approach for hyperbolic PDE. In following the semi-discrete approach, we are guaranteed that the resulting discrete system will be consistent with the original set of PDE (at least for simple BC). Consistency means that the Taylor series expansion of the discretized equations is equivalent to the original PDE in the limit where the spatial grid size and time step go to zero *independently*.

Following the semi-discrete approach, there are a variety of time marching schemes that could be applied to the resulting system of ODE, which we now write in vector form:

$$\frac{d\mathbf{q}}{dt} = \mathbf{F}(\mathbf{q}, t), \tag{36}$$

where $\mathbf{q}$ is a vector of length N containing the discretized dependent variables on the mesh. In general $\mathbf{F}$ is a nonlinear vector function of $\mathbf{q}$, and, in problems with time-dependent forcing or BC is non-autonomous. Here N is the total number of degrees of freedom of the system, typically the number of grid points times to number of dependent variables.

Time marching methods for Eq. (36) can be separated into *explicit* schemes, where the right-hand side of Eq. (36) is written as a linear combination of its value with $\mathbf{q}$ evaluated at previous time level(s), and *implicit* schemes, where the right-hand side may also use $\mathbf{q}$ at the new time level. It is also possible to split the right-hand side, evaluating some terms with explicit schemes, and some terms with implicit schemes. Typically, implicit schemes are solved with iterative or approximate factorization methods.

Implicit methods are generally useful for integrating *stiff* systems of ODE, in situations when it is appropriate to *suppress* the components of the solution corresponding to the fastest eigenvalues. This can be done on physical grounds (e.g. allowing fast chemical reactions to be in equilibrium, following the time scale of slower reactions), or on numerical grounds (e.g. when the "fast" solutions can be identified with irrelevant or poorly resolved components of the solution space, or when acceleration to a steady state solution is desired). An example of the former (physical suppression) is the low-Mach number scheme of Wall et al. [181], which utilizes a staggered second-order discretization in *both* space and time. Semi-implicit time-advancement is used to suppress high frequency acoustic waves, effectively relieving the CFL constraint associated with the acoustic speed (i.e. much larger timesteps based on the convective CFL restriction are taken). The staggering also leads to the desirable property of not dissipating the low-frequency resolved acoustic waves. Suppression based on numerical grounds commonly arise near solid boundaries in a flow, and especially near corners and other singularities (or near singularities) that require clustering of grid points. Collis and Lele [182] have used an implicit Euler for convergence to steady state and a second-order-accurate two step implicit scheme for unsteady calculations in their studies of acoustic receptivity near a swept leading edge. Barone and Lele [41] use implicit schemes for steady state and a fourth-order RK method for time-accurate solutions trailing-edge receptivity problems. Gaitonde and Visbal [163] use second-order-accurate implicit approximately factored schemes in their high-order-accurate Navier–Stokes code. Moin and Mahesh [183] provide further discussion of these issues in the context of DNS.

For explicit FD schemes, we concentrate on two formulations that have received the most attention in CAA: Runge–Kutta methods (RK) and Linear Multistep methods (LM). These two methods differ in the way information propagates forward in time: the RK method is a so-called "one-root" method; integration proceeds forward from any point without using prior behavior of the solution. LM methods of order greater than first, are multiple-root methods; the solution depends on past instances in time, and, in general is a superposition of a physically correct solution (i.e. one that tends to the correct solution as the timestep goes to zero) and spurious solutions. Spurious solutions must be suppressed by choosing a timestep small enough such that they are damped in time. Generally, LM methods are not self-starting, since they depend on previous time levels. Lower order LM methods are required for the first few steps.

In general, an s-stage RK method for Eq. (36) is:

$$\mathbf{q}^n = \mathbf{q}^{n-1} + h \sum_{i=1}^{s} b_i \mathbf{k}_i,$$
$$\mathbf{k}_i = \mathbf{F}\left(\mathbf{q}^{n-1} + h \sum_{j=1}^{i-1} a_{ij} k_j, t^{n-1} + \Delta t c_i\right), \qquad (37)$$

where $\mathbf{q}^n$ are the dependent variables evaluated at time level $t^n = t^{n-1} + \Delta t$, and Δt is the timestep. The coefficients b_i, and a_{ij} and $c_i = \sum_{j=1}^{i-1} a_{ij}$ can be determined by satisfying a series of conditions (see, for example, Ref. [184] for a given level of accuracy, p, or by other added constraints, as discussed below).

The linear stability of RK methods can be readily analyzed. The maximal timestep that ensures stability is determined by the eigenvalues of the linearized right-hand side of Eq. (36). Classical RK methods have accuracy level equal to the number of stages, $p = s$, up to fourth order accuracy, and their stability region includes a portion of the imaginary axis for the 3rd (RK3) and fourth (RK4) order accurate schemes. For this reason these schemes have been widely used in both turbulence and aeroacoustic calculations, where the diffusion (negative real part of the eigenvalue) may be small (and is zero for the inviscid equations).

As discussed in Section 4.1, the eigenvalues of the right-hand side of Eq. (36) are pure imaginary when centered FD schemes are used in Eq. (17). In that case the minimum time step is given by a Courant condition:

$$\text{CFL} = \frac{c\Delta t}{h} < \frac{c_1}{K_{\max}}, \qquad (38)$$

where c_1 is a constant depending on the RK method, and $K_{\max}$ is the maximum value of the modified (nondimensional) wavenumber of the FD scheme, as defined in Section 4.1.5. The value of c_1 is 1.7 and 2.8 for RK3 and RK4, respectively.

For a purely diffusive model problem like Eq. (23), the eigenvalues are pure real, and negative, and

$$\frac{v\Delta t}{h^2} < \frac{c_2}{K_{\max 2}}, \qquad (39)$$

where c_2 is a constant equal to about 2.5 and 2.8 for RK3 and RK4, respectively, and $K_{\max 2}$ is the maximum modified wavenumber of the second derivative operator (Section 4.1.6).

In solving nonlinear and/or multidimensional equations, the preceding constraints can still be used to give an estimate for the maximal timestep, but c should be interpreted as an estimate of the maximum phase speed of propagation, and h the minimum grid spacing.

RK methods cause additional dispersion and dissipation, beyond that discussed in Section 4.1 for FD approximations of spatial derivatives. By optimizing the coefficients of the RK method it is possible to derive schemes that have lower formal order of accuracy than could be achieved for a given number of stages, but that are more accurate over the full range of frequencies. This is akin to optimization of the spatial scheme as discussed in Section 4.1.2. Zingg et al. [185], for example, developed a six-stage RK method that was second-order accurate, but optimized for linear wave propagation problems. Hu et al. [186] optimized 4, 5, and 6 stages schemes with at least second-order accuracy, and also proposed several two-step schemes where a different set of RK coefficients are used at alternating timesteps. These schemes were 4/6 and 4/5 stages and fourth-order accurate for linear problems and second-order-accurate for nonlinear problems. These schemes are referred to in the literature as "low dissipation and low dispersion" (LDD) schemes. The conclusions from these studies are similar to what was shown for the spatial discretization in Section 4.1.5. That is, optimized schemes are generally more efficient so long as the accuracy requirements are not too strict.

Another issue of practical relevance is storage requirements for the RK method. Let us define the number of storage locations for each of the N degrees of freedom that constitute Eq. (36) as M. Some standard third-order RK methods can be written so that $M = 2$. Standard fourth order methods cannot be found with $M < 4$, but 5-stage fourth order methods with $M = 3$ have been devised [187]. Some of the free coefficients are used to lower the storage requirements, rather than maximize the order of accuracy. Stanescu and Habashi [188] have generalized the LDD schemes so that they are fourth-order accurate even in nonlinear problems, and so that $M = 2$. They show that when the two-step 4/6 scheme is used on Eq. (17), that the error is similar to a RK4 scheme (with a smaller time step) that required about 2.5 times the number of evaluations of $\mathbf{F}(\mathbf{q})$ to reach a fixed time.

We briefly mention the work of Tam and Webb [102] in optimizing the coefficients of a LM method for wave propagation problems. LM methods are appealing from the point of view of efficiency, since they generally require only one evaluation of $\mathbf{F(q)}$ per time level. A caveat is that their spurious roots can have a much lower Courant stability constraint than higher-order RK methods. The DRP scheme has a maximum CFL = 0.23 for Eq. (17) when used with the DRP FD scheme [102]. A standard RK4 method would be stable with the same scheme to about CFL = 1.6. When the modified dispersion characteristics of the full schemes are compared, it is apparent that similar levels of dissipation are obtained when RK4 is used with CFL = 1 and Tam's LM method is used with CFL = 0.23. With 4 evaluations of $\mathbf{F(q)}$ for RK4, and one for the optimized LM method, it is apparent that they have roughly equal computational cost for a given accuracy.

4.3. Boundary conditions

One of the most challenging aspects of CAA is the imposition of robust (stable) and accurate BC. There are several important classes of BC that we may wish to simulate: solid wall boundaries (viscous, inviscid, specified acoustic impedance), "free space" BC that simulate flow on an infinite or semi-infinite domain, and, with most difficulty, inflow/outflow BC. For the latter, we seek BC that specify a (possibly turbulent) stream entering the computational domain, or conditions that allow the stream to exit the domain "smoothly" (i.e. without turning or producing acoustic reflection and/or induced flow). In subsonic flows, inflow/outflow conditions must also allow for acoustic waves that are propagating in the direction opposite to the stream. Thus, viewed as waves, incoming and outgoing dis-turbances exist at both upstream and downstream boundaries.

When the flow near the boundary consists of small amplitude disturbances to a relatively uniform flow, then analytical techniques can be used to solve the governing equations exterior to a truncated computational do-main. In this case, artificial BC on the truncated domain that are consistent with the linear exterior solution are straightforward to derive, although a host of technically challenging implementation issues arise. As there are already several reviews of these BC [189–193], we only briefly review them in Section 4.3.1 below, and compare their performance on model problems in Section 4.3.1. It should be noted that the development of artificial BC for Maxwell's equations have closely paralleled the work with the linearized Euler equations.

The development of inflow and outflow BC when there are strong flow gradients or significant fluctuation levels is conceptually less straightforward and invariably involve physical modeling approximations in addition to mathematical approximations. In many cases the under-lying fluid dynamic issues are themselves challenging, for example the sensitivity of turbulent free shear flows to their external disturbance environment. One possibility is to simply neglect nonlinear or shear effects and apply BC developed for the linearized problem. Such techni-ques are often suitable for inflow or transverse boundaries of jets and other shear flows. The primary difficulty is with outflow conditions, where linearization has been shown to produce large errors [194]. For the outflow problem, a variety of ad hoc buffer zone techniques have been developed. These are discussed in Section 4.3.3.

As a motivating example of the BC discussed here, consider the computation of flow/acoustic instabilities in open cavity flow, depicted in Fig. 14. In the separated shear layer, vortical instabilities grow and impinge on
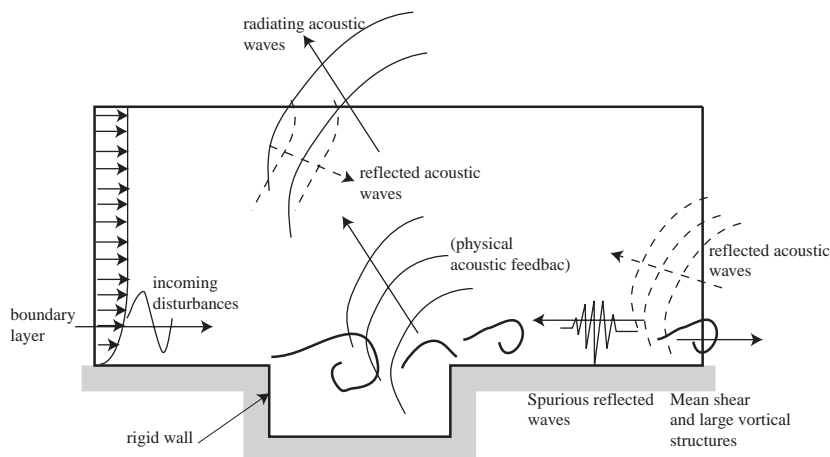

Fig. 14. Schematic diagram of boundary condition requirements for flow over an open cavity.

the cavity trailing edge, producing acoustic radiation. The acoustic waves in turn excite new instabilities as they interact with the cavity leading edge. Computational artifacts (i.e. reflections) can interfere with this instability. The no-slip BC at the rigid walls is relatively straightforward and is discussed in Section 4.3.4. At the outflow boundary, there is mean shear in the boundary layer as well as large-scale vortical structures produced by the cavity instability. The BC must allow these structures to exit the domain without producing acoustic reflections. Here buffer zone techniques are needed to control reflections (see Section 4.3.3). At the inflow boundary, a similar situation exists—the BC must allow upstream propagating acoustic waves to exit the domain while allowing for the mean boundary layer profile and incident disturbances (if any) to be specified. One could potentially use some of the linearized BC discussed in the next section, but buffer layers perform well here too. Away from the boundary layer, on the inflow, outflow, and normal boundaries, we have nearly uniform flow with small amplitude acoustic disturbances. Here the linearized BC of the next section would in principle perform well, but there is a significant practical difficulty associated with *blending* those BC with the buffer layers needed on other portions of the same boundary near the boundary layer. Thus one is tempted to use a buffer layer around the entire inflow/outflow and normal boundaries as was done by Freund [36] for turbulent jet and Rowley et al. [38] for the cavity-flow example considered here.

The motivating example shows that even relatively simple aeroacoustic problems provide many challenges for posing accurate and robust BC. In addition, implementation in codes can be difficult and if buffer zone techniques are used then tunable parameters must be set through trial and error.

4.3.1. Linearized BC

The development of BC for the Euler equations linearized about a relatively uniform flow follow three distinct approaches: *nonreflecting* BC, where one attempts to zero any *incoming* waves at a computational boundary; *radiation* BC, that assume the boundaries are located far from any source of disturbances and use asymptotic solutions to the exterior problem to specify the BC-similar to the classic Sommerfled radiation condition, but applied at a finite truncation of free-space; and the *perfectly matched layer* where the domain is enclosed in a buffer region where terms are added to the governing equations to minimize reflection of outgoing waves. All of these approaches are approximate in the sense that they are not perfectly nonreflecting, but at least in principle allow for a hierarchy of progressively more accurate conditions with increasing computational cost and/or complexity.

Nonreflecting BC: In a single spatial dimension, the characteristics of hyperbolic systems of equations are trajectories in the $x - t$ plane along which the amplitude of waves is governed by an ODE. The sign of the velocity of the wave determines whether the wave is incoming at an artificially boundary (and therefore must be specified). The resulting *characteristic* BC are exact in one-dimensional flow but have also been used in an approximate way in multidimensional flows, and are discussed below in Section 4.3.2. They are approximate because in two and three dimensions the characteristics are surfaces or hyper-surfaces, and do not give rise to a *local* decomposition of the solution into incoming and outgoing waves, with the result that any statement of nonreflection must be non-local in space and or time.[6]

One approach to developing non-local nonreflecting BC in the multidimensional case is to decompose the solution into Fourier/Laplace modes, as was accomplished for the wave equation in the work of Engquist and Majda [195,196] and for the Euler equations by Giles [197]. Such techniques are appropriate for (at least locally) planar boundaries.[7]

The general procedure is as follows. One first decomposes the solution into Fourier space in the direction(s) along the plane boundary and Laplace space in time, and attempts to decompose the resulting system of coupled ODE into incoming and outgoing waves. When such a decoupling exists, then the resulting decoupled equations are analogous to ODE for the one-dimensional characteristic amplitudes. Once the incoming wave amplitudes are specified (zero usually being the appropriate incoming wave amplitude for the *nonreflecting* case), then one must inverse Fourier/Laplace transform the resulting BC to apply them in real space. However, the inverse transformed equations are in general convolution integrals (over the coordinate tangent to the boundary and/or time). The convolution integrals must either be discretized directly, or else additional approximations need to be introduced to localize the equations (i.e. to give differential rather than integral equations).

For the linearized Euler equations, there are some difficulties associated with the waves that propagate tangent to the boundary that require special attention to insure well-posedness of the BC. For the Euler equations, nonlocality is introduced through the dispersion relation for the acoustic waves, and is expressed through a square root that appears in the decoupled

---

[6]It should be noted that exact decomposition is unnecessary in the case of supersonic flow (at least the inviscid case) since all waves propagate downstream.

[7]Techniques for other coordinate systems may be derived in similar manners as discussed at the end of this section (though in work to date such derivations have primarily been focused on the simple wave equation).

equations. Some recent work [198,199] directly discretizes the convolution integrals resulting from inverse transforming the square root; the more common attack is to develop a hierarchy of local, approximate BCs by introducing a rational function approximation. Well posedness imposes some restrictions on the specific rational function approximations (and orders of the numerator and denominator polynomials) that can be used [200,201]. Padé approximants to the square root provide a hierarchy of conditions that are locally nonreflecting for waves at progressively steeper angles to the boundary. The simplest well posed approximation is that the square root is unity, equivalent to Giles' outflow and "modified" inflow BC [197]. Whatever the choice (and order), the BC can be inverse Fourier transformed to generate a (possibly high-order) PDE to be applied to the boundary points. These can also be cast as a system of first-order equations by introducing auxiliary variables (e.g. [201,202]).

It is important to note that all (stable) rational function approximations give perfect reflection for tangential waves, and thus the resulting BC give the highest errors for waves with steep inclination to the boundary. For computational domains that involve wall or periodic BC transverse to the nonreflecting direction, relatively poor performance is obtained at long times when the solution is dominated by tangent waves. Nevertheless, the higher-order rational function approximations can vastly reduce reflection errors over a range of angles compared to the lower-order conditions [201].

At edges (3D) or corners (2D) of non-periodic rectangular domains one requires a set of compatibility conditions that would blend the differing approximations made on the intersecting boundaries. However, no general formulation of such conditions has been found. Some ad hoc procedures that can be used with (0,0), (2,0), and (2,2) Padé approximations to the square root have been found [192].

Only the lowest-order conditions (i.e one-dimensional, and modified Giles conditions) have been applied to problems linearized about a *nonuniform* base state. In the general case with multiple artificial boundaries, stability for the continuous problem with non-constant coefficients does not follow from stability of the constant coefficient case. Moreover, simply replacing the constant base flow coefficients in the BC by their local values at a point in the flow would be correct when the lengthscale of the disturbances is much smaller than any variation of the base state (i.e. the high frequency limit). There are many problems of interest for which this could lead to large errors. For example, linear instability waves in a shear flow are low frequency disturbances. Essentially any advective disturbances that has a significant non-acoustic pressure fluctuations will lead to significant acoustic reflection at a downstream boundary. Extension of nonreflecting BC to nonuniform

mean flows remains an important area of future research.

Radiation BC: An alternative procedure for specifying artificial BC for the Euler equations linearized about a uniform base flow is to consider asymptotic solutions for the propagation of outwardly propagating disturbances at large distance from their source. The technique was originally developed by Bayliss and Turkel [203,204] who derived a hierarchy of BC with increasing accuracy for the simple wave equation. The first term is equivalent to the classical Sommerfeld radiation condition, but applied at a finite distance rather than at infinity. For the linearized Euler equations, Bayliss and Turkel derived conditions suitable for the outflow and characteristic boundaries (where the mean flow is identically zero). Tam and Webb [102] have extended the analysis to inflow boundaries, but only for the first term in the expansion. This one-term expansion can suffer inaccuracies whenever the source is not centered within the domain (or when the domain is not large enough), because the asymptotic expansion converges only slowly in the general case. Hagstrom and Hariharan [205] have extended the hierarchy for the convected wave equation, and it is likely that full extension to the linearized Euler equations will be achieved in future.

Tam and Dong [206] allow for a nonuniform mean flow on the boundary by replacing the linear perturbations in the BC with departures from the base flow. As in the Fourier/Laplace BC, this is a high-frequency approximation that is not expected to be accurate at inflow/outflow boundaries in shear flows. Tam and Webb [102] also suggest a strategy for implementation of the radiation BC in FD calculations. Their method introduces rows of "ghost" points outside the computational boundary. The number of ghost points is equal to N_a of Eq. (11) for centered FD schemes. One sided optimized FD schemes are used to compute derivatives normal to the boundary at the ghost points, and the BC is used to advance the solution at the ghost points.

Perfectly matched layer: An alternative to the Fourier/Laplace and radiation BC for the linearized Euler equations is the perfectly matched layer (PML), which was originally formulated for electromagnetic radiation problems [207], but was extended to the linearized Euler equations by Hu [208]. The PML is a buffer layer adjacent to the edge of the computational domain, in which the fluid properties are altered in a manner that forces waves to decay in all directions of propagation. The theory behind the PML relies on the analytical solutions to the linearized Euler equations discussed in the two previous sections, see, for example, Abarbanel, Gottlieb and Hesthaven [209].

Early problems with the PML approach included observations of long-time stability problems [210,211] and requirements for the mean flow to be aligned with one of the coordinate directions near the boundary.

More recent work appears to have resolved these difficulties, and well-posed (stable) layers can now be obtained under general uniform flows [209,212,213]. Unlike the hierarchy of nonreflecting and radiation conditions, there are parameters that must be tuned to optimize the performance of PML. These include the layer thickness, and a profile that controls the amount of absorption over the layer. Some comparisons of PML with radiation and nonreflecting BC are given in Section 4.3.1. The computational work of PML is relatively high compared to nonreflecting conditions of a similar accuracy, but they do not suffer the corner problem inherent to nonreflecting BC.

Recently, Hagstrom and Nazarov [214] have extended PML to nonuniform flows, and in particular parallel shear flows. There are some difficulties with establishing the free parameters (there are now two, in addition to the layer thickness) in order to damp physical instabilities associated with the mean velocity profile, but promising results have been obtained [215] and further investigation of the method appears warranted.

Accuracy comparison of linearized BC: The three approaches to linearized BC rely on differing approximations and it is of interest to compare their accuracy on model problems. Many comparisons have already been presented in the literature (e.g [216,210] and references therein). A difficulty in comparing BC is assessing whether any error is caused by the formulation of the (continuous) BC, or because of errors associated with the boundary closures or other implementation issues. Some previous comparisons were made using dissipative numerics (upwind-biased or explicit artificial viscosity or filtering), but these can suppress long-time instabilities associated with the BC, leading to an accurate solution, but with a loss of generality since the BC cannot be applied independently of the choice of damping. Here we have chosen to use non-dissipative FD schemes to solve the linearized Euler equations (with uniform flow) on a uniform mesh with a 4th-order compact scheme (c4), together with fourth-order RK time stepping and a Courant number of 1/2 (such that there is only the slight dissipation associated with the time marching). The FD formula are closed using third-order explicit one-sided FD at the boundary node, and at each time step the BC are imposed by using the one-sided FD scheme for any normal derivatives that appear in the BC.[8]

We consider here several model problems involving acoustic radiation[9] in a uniform flow with a Mach number of 0.5, so that the left and right boundaries correspond to inflow and outflow, respectively. The top and bottom boundaries are treated as nonreflecting outflow boundaries for the Fourier/Laplace BC (and as closure to the PML layer), and as a regular far-field radiative condition for the radiation BC. Boundaries placed at $x_1, x_2 = \pm 10\alpha$, where α is a constant that describes the width of an initial Gaussian pulse in pressure placed in the domain, and the error is measured by comparing with the solution found on a much larger domain (with the same grid resolution and timestep), in order to isolate errors associated with the BC. The error is measured by summing the errors in u, v and p over each point in the region $x_1, x_2 = \pm 8\alpha$. We thus ignore the error in the PML layer and in a layer of equivalent width for the other BC. This way the computational work is the same for all methods. For all cases the grid spacing is 0.1α in both directions.

For the first case, the pressure pulse is initially centered in the computational domain, and the center of the pulse is taken as the origin in the radiation BC [102]. Results are shown in Fig. 15 for the following methods: local Fourier/Laplace BCs with (0,0) and (2,2) Padé approximants for the square root, simple one-dimensional characteristic BCs (that correspond to a linearized version of the Thompson BC discussed below), the radiation BC, and finally PML with 10, 20, and 30 point layer widths. The (0,0) Fourier/Laplace BC is identical to the "modified" BC proposed by Giles [197]. For this test, radiation conditions perform best especially at early times. In our implementation, the radiation conditions resulted in a slow long-time instability that was not reported in previous comparisons [102,216]. At earlier times the maximum errors of the (0,0) and (2,2) Fourier/Laplace BC are about a factor of 2 higher than the radiation BC, while maximum error for the characteristic BC are about an order of magnitude higher than the others. The PML layer with 30 points gives similar error to the (2,2) Padé Fourier Laplace condition. At the earliest times when the initial pulse is just leaving the computational domain, the (2,2) Fourier/Laplace has a much smaller

---

[8]The PML tests were conducted by Matt Barone (Stanford University) following the implementation by Arbabanel et al. [209]. All parameters were chosen identical to those that the authors used, except that the *layer strength* was changed to $C_x = C_y = 0.5$, which gave the best results with $N_{bf} = 20$. It was noted that the results were not sensitive to this parameter provided that $0.25 \leqslant C_x \leqslant 1.0$. The PML layers were closed with the one-dimensional characteristic BC discussed above. One

(footnote continued)
case was run with (0,0) Padé BC but the results were virtually identical.

[9]Nonreflectivity to passage of a vortex or entropy wave through the outflow boundary is also of interest. We consider vortex propagation in the context of nonlinear BC in Section 4.3.3. For the linearized problem, the Fourier/Laplace BC are exactly nonreflective for the vorticity and entropy waves (at least in the absence of discretization errors or artifacts). The other methods typically give rise to errors that are similar in relative magnitude (compared to the wave amplitude) as for the acoustic tests presented here.
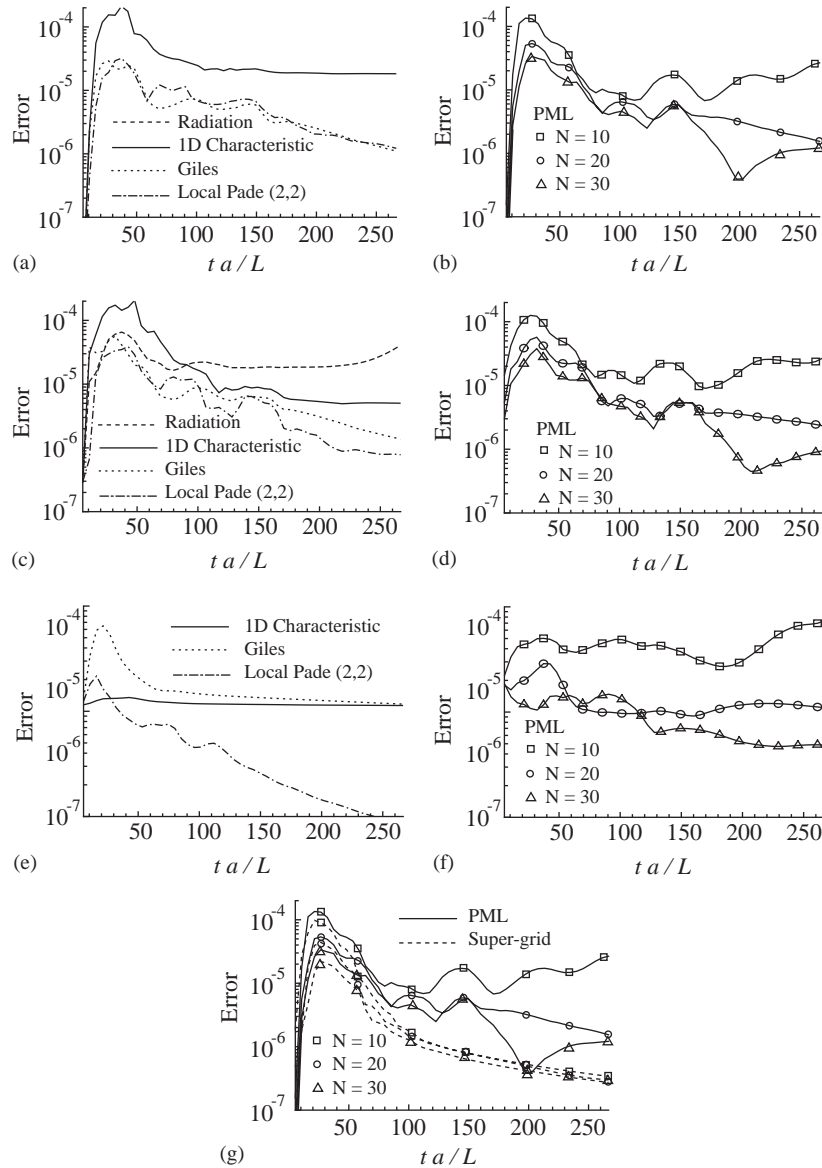
Fig. 15. Performance of linearized boundary conditions on test problems. (a,b) Centered acoustic pulse; (c,d) Off-centered acoustic pulse; (e,f) Random initial condition; (g) comparison of PML with super-grid BC (see Section 4.3.3) for the centered acoustic pulse case.

error than the (0,0) approximation (Giles), and is similar in magnitude to the radiation BC. At later times most of the waves remaining in the computational domain are propagating nearly tangent to the boundaries, which is the worst-case situation for any of the Fourier/Laplace BC.

The above test results in conclusions similar to earlier studies, in which the radiation conditions perform best. However, if we consider the same model problem, but *offset* the initial pulse from the center of the domain, we

see that the accuracy of the radiation BC is degraded. This is shown in Fig. 15(b) and (c), where the initial pulse has been offset a distance of 5α in the $+x_1$ direction. Now the $(0,0)$ Fourier/Laplace and radiation BCs show similar maximum errors, but the $(2,2)$ Fourier/Laplace now has a lower maximum error by about a factor of 2, and is roughly equivalent to the 30 point PML layer. Obviously when the center of any pulse is known a priori, optimal performance of the radiation BC could again be achieved by simply shifting

the origin of the equations, but this is not likely to be known in practice.

In a final test, we initialize the computation with u, v and p set to a different pseudo-random (uniform probability between 0 and 1) at each point (including boundary) in the domain. We then measure the sum of the root-mean-square values of u, v, and p (rather than the difference with any exact solution) as a function of time. This provides an indication of "worst case" performance the of the BCs, and measures their ability to effectively remove vortical and acoustic disturbances at a variety of wavelengths and angles of incidence from the boundary. The results are presented in Fig. 15(e,f). In this test, the $(2,2)$ Fourier/Laplace BC gives a substantial advantage over the $(0,0)$ and one-dimensional characteristic BCs, and even the 30 point PML.[10]

Discrete effects in linear BC: It has already been discussed in Sections 4.1.3 and 4.1.4 that BC boundary closures of FD formula are coupled and together can lead to the generation of spurious waves. Because the spurious solutions propagate with negative group velocity, the coupling leads to the generation of spurious waves from physical waves that are outgoing at the boundary, and to the opposite coupling when the physical wave is incoming at the boundary. This coupling was recognized by Vichnevetsky [157,158], who constructed a hierarchy of boundary closures for second-order FD schemes applied to Eq. (17) that attempt to eliminate the reflections between physical and spurious waves. Colonius [217] generalized these conditions to high-order and compact finite differences [217] for (linear) one-dimensional systems of hyperbolic equations.

For the multidimensional linearized Euler equations, the physical solutions to the continuous equations cannot in general be decoupled in physical space, as discussed in Section 4.3.1. There is now a new objective for our boundary losures: in addition to separating incoming and outgoing waves, we can also attempt to separate physical and spurious waves. Rowley and Colonius [201] showed that the accuracy of the continuous Fourier/Laplace BC (Section 4.3.1) can be significantly degraded when the coupling of physical and spurious waves is ignored. In the continuous case, there are only 3 relevant reflections to minimize at the downstream boundary (the downstream propagating vorticity, entropy and acoustic waves may all generate upstream propagating acoustic waves), and 3 relevant reflections at the upstream boundary (the upstream propagating acoustic waves may generate downstream propagating vorticity, entropy and acoustic waves). In

the discrete case, there are *twelve* reflections to minimize at each boundary. Rowley and Colonius show how to minimize the reflection coefficients by combining the Fourier/Laplace decomposition of incoming and outgoing waves (Section 4.3.1) together with a numerical Sommerfeld BC.

Boundary closures that reduce the reflection of spurious waves at a solid wall have been developed by Tam and Dong [218]. They showed that the discrete equations (using the DRP scheme) support two types of spurious waves: the short wavelength propagating wave discussed above and a spatially damped wave that is trapped near the hard wall. They present an optimized boundary treatment with ghost points to reduce the reflection of spurious waves. Damping of these modes is especially important when implicit methods are used to accelerate convergence to time-asymptotic behavior. Collis and Lele have studied such schemes in the context of the receptivity of high-speed flow near a swept leading edge [182].

4.3.2. Nonlinear BC: Thompson's approach

While there are advantages and disadvantages to each of the approaches to linearized BC discussed in the previous section, none (yet) allow accurate nonreflectivity to be achieved in general nonuniform flows. The same is true of their application to nonlinear calculations, where in addition to mean flow gradients there are finite-amplitude effects in the interaction of disturbances with the boundary. The importance of nonlinearity at the outflow boundary was demonstrated by Colonius et al. [194,219], who studied a zero-circulation vortex propagated through an outflow boundary in an otherwise uniform flow. The exact solution (close to exact for a slight viscosity) is that the vortex propagates with constant speed, unaltered by the uniform flow. Two linearized BC were used: the Giles [197] outflow condition, where in the linear case outgoing vorticity produces no incoming acoustic wave, and the modified Giles condition, which produces incoming acoustic waves proportional to the amplitude of the vortex. The results, shown in Fig. 16, demonstrate that when the induced velocity from the vortex is a significant fraction of the uniform velocity, nonlinear reflections are as significant as linear reflections from the less-accurate BC. The addition of shear at the boundary is likely to make matters worse. In this example, it is even possible for the sign of λ_1 to change as a function of time (changing outflow to inflow) when the strength of the vortex is large enough. This condition causes the standard linearized treatment to fail.[11] However, even

---

[10]Our implementation of the radiation BC was unstable for this case; the random initial conditions excited the instability early and prevented any meaningful comparison of the results with the other methods.

[11]In some situations (e.g. Mitchell et al. [33]), such as mixing layers and jets, it is possible to prevent λ_1 from changing sign by adding a small co-flow that has little impact on the physics.
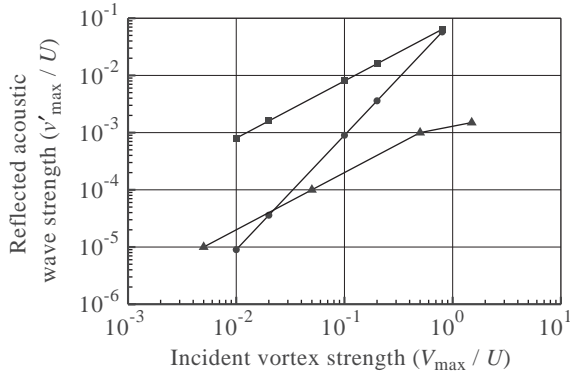
Fig. 16. Performance of linearized outflow BC for propagation of a nonlinear vortex (characterized by its maximum induced velocity, V_{max}) in a uniform flow, u_0. The maximum normal velocity in the acoustic reflection, v'_{max} is plotted. The Giles condition would, in linear calculation, produce no reflection. For reference, the super-grid model (see Section 4.3.3) is also plotted. Giles [197] (●); Modified Giles (■); Colonius and Ran [219] super-grid buffer (▲).

in less pathological cases, nonlinearity still produces large reflections.

There is one specialized circumstance in which accurate nonlinear, nonreflecting BC can be posed: flow in a single dimension. For the case of one-dimensional flow, BC follow immediately from the classical method of characteristics solution [220]. That is, it is possible to locally identify and decouple, even in the nonlinear case, left- and right-going waves. Three characteristic curves (in $x - t$) can be identified whose slopes are $\lambda_1 = u$, $\lambda_2 = u + a$, and $\lambda_3 = u - a$. BC are required for any characteristic crossing into the computational domain (based on the sign of λ). The integrated values of the dependent variables along the characteristic curves are known as Riemann invariants, and these BC are usually referred to by that name, or by the term *characteristic BC*.

The BC discussed above are exact only for one-dimensional problems, but may be used as an approximation in multidimensional flow. Thompson [221,222] proposed a similar BC in the multidimensional case. In his notation, the conservative form of the Euler, continuity, and energy equations are written

$$q_t + P(u)S(u)\mathscr{L} + g(q)_y = 0, \qquad (40)$$

where q and $g(q)$ are the standard conserved variables and their fluxes transverse to the boundary, and $u = (\rho, u, v, p)^T$ are the primitive variables. P is the Jacobian matrix that transforms between conservative and primitive variables ($p_{ij} = \frac{\partial q_i}{\partial u_j}$), and S is a matrix whose columns are the right eigenvectors of A and $\mathscr{L}$ is a

vector whose components are:

$$\mathscr{L}_1 = \lambda_1 \frac{\partial v}{\partial x},$$

$$\mathscr{L}_2 = \lambda_1 \frac{\partial s}{\partial x} = \lambda_1 \left[\frac{\partial p}{\partial x} - a^2 \frac{\partial \rho}{\partial x} \right],$$

$$\mathscr{L}_3 = \lambda_2 \left[\frac{\partial u}{\partial x} + (\rho a)^{-1} \frac{\partial p}{\partial x} \right],$$

$$\mathscr{L}_4 = \lambda_3 \left[\frac{\partial u}{\partial x} - (\rho a)^{-1} \frac{\partial p}{\partial x} \right]. \qquad (41)$$

These are just the slopes of the characteristic curves multiplied by the x-derivatives of the Riemann invariants. The analysis proceeds identically to the one-dimensional case, by specifying the values of $\mathscr{L}$ at the boundary when the 1D characteristics are directed into the computational domain (and by using one-sided differences in Eq. (41) when they are directed out). The conditions lead to a simple corner treatment for Cartesian domains: one imposes BC simultaneously on $\mathscr{L}$ and the equivalent transformation of the y-fluxes. In tests and in practical computations, this appears to be robust, though the errors near the corner are large [222,223].

While Thompson's BC share similarities with the linearized Fourier/Laplace BC of Section 4.3.1 (they are for example, exactly nonreflecting for linearized waves at normal incidence), there are fundamental differences. For the incoming characteristics must carry information about the entire flow, not just disturbances to a base state. Even labeling of $\mathscr{L}$ as incoming or outgoing is a dynamic process that could change signs on a given boundary or in time. In rare cases a complete solution of the Euler equations in the exterior could be used to compute $\mathscr{L}$ (see for example [224,33]). Usually $\mathscr{L}$ must be specified based on minimal information about the exterior problem.

For the inflow, one might wish to impose a target velocity profile, as well as perhaps temperature or another thermodynamic variable. The traditional approach is to simply impose Dirichlet BC on the correct number of variables, four in the case of inviscid subsonic inflow (in three dimensions). Such BC have been studied extensively and proofs of well posedness exist (in many cases for both inviscid and viscous cases) for a number of different specifications. Poinsot and Lele [223] describe a method that combines Dirichlet BC for velocity and temperature and Thompson-style analysis for the remaining $\mathscr{L}$ needed to close the continuity equation.

The problem is that all the Dirichlet BC are badly reflective for the upstream propagating acoustic wave, forcing, as they do, fluctuations in certain acoustic variables to zero. Imposing the one-dimensional characteristics will be equivalent, upon linearization, to the one-dimensional nonreflecting BC and therefore at least

transparent to plane waves propagating directly up-stream, but imposing velocities and density perturbations to zero will be perfectly reflecting even for plane waves.

A much less reflective inflow can, however, be constructed if more information is specified about the incoming flow. Sometimes the inflow will be laminar with small disturbances, and linearization is appropriate, i.e. $\mathscr{L} = \mathscr{L}_o + \mathscr{L}'$. In the inviscid case, steady, unidirectional, transversely sheared flows are an exact solution provided pressure is constant. Linearizing about this state, we obtain $\mathscr{L}_o = 0$, and all incoming $\mathscr{L}'$ should be specified, for example $\mathscr{L}' = 0$ for the nonreflective case. For the viscous case, often a solution of the boundary layer equations will be appropriate, and in that case $\mathscr{L}_o$ will depend on the (slow) variation of boundary layer thickness with the streamwise coordinate. In principle, any of the BC discussed in Section 4.3.1 could then be used to specify conditions for $\mathscr{L}'$, although the extent of nonreflectivity will be limited to the high-frequency limit as discussed in that section.

At a subsonic outflow, one BC is required in the inviscid case. In three dimensions, the other four variables can be found, as in the inflow case, from Thompson's approach or equivalently the *locally one-dimensional, inviscid* (LODI) approach of Poinsot and Lele [223]. The problem is to specify the sole incoming characteristic, $\mathscr{L}_4$. If linearization about a uniform state is appropriate (it seldom is at the outflow), then $\mathscr{L}_4' = 0$ could be used. In the majority of situations, however, fluctuations about the mean flow are not small, and the mean flow is not known anyway.

For nonlinear calculations the use of $\mathscr{L}_4 = 0$ has been suggested [222], but is problematic because there is nothing to prevent the time-averaged pressure from drifting, especially if characteristic BC are also imposed at the inflow [225,223]. On physical grounds, the upstream propagating characteristic would, at least under steady conditions, provide whatever acoustic reflections were needed to fix the downstream pressure. Of course, using a simple Dirichlet condition $p = p_\infty$ would rectify this (as indeed is still standard practice in many CFD codes), but this corresponds to a badly reflective boundary–perfectly reflective for plane acoustic waves. Rudy and Strikwerda [225] proposed modifying the one-dimensional characteristic condition to obtain

$$p_t - \rho a u_t + \alpha(p - p_\infty) = 0. \tag{42}$$

This modifies the reflectivity of the boundary so that, at steady state, the pressure there is fixed. In Eq. (42), α is an adjustable parameter that was optimized to achieve steady state in a one-dimensional, linearized problem most rapidly. It was later used in the characteristic formulation by [223], and in implementing Giles conditions in sheared flows by [194]. Unfortunately,

there has been no systematic study of how to prescribe α in general.

For viscous flows, the required number of inflow and outflow BC is different from the inviscid case [226,227]; additional constraints (beyond the inviscid ones) typically take the form of requiring certain gradients of the dependent variables (or combinations of them) to be zero at the boundaries. For the most part, formulations to date have focused on (i) obtaining a well-posed problem in the continuous case and a stable problem in the discrete case, and (ii) avoiding the creation of viscous boundary layers at inflow and outflow boundaries by requiring that the inviscid BC are obtained (smoothly) in the limit as viscosity vanishes (e.g. [228]). Well-posedness is of course a necessary goal, but unfortunately nonreflectivity, even in the linearized case, has been limited to one-dimensional analysis (e.g. [229]). Other work on viscous BC demonstrates the complex interaction between continuous BC and closures for finite-difference schemes near the boundary. For example, many practitioners simply use inviscid BC (usually characteristic-based) with no additional constraints beyond one-sided differences to close the viscous derivatives. This is only justified at high Reynolds number. Some studies (both theoretical and empirical) have examined the effects of extrapolating all flow variables (or fluxes) at an outflow boundary [230–233], corresponding to no BC for the continuous case. Of course, the needed closure of the discretization at the boundary (i.e. the extrapolation) does correspond to *some* BC, even if it is difficult in general to establish the continuous counterpart.

4.3.3. Nonlinear BC: Buffer zone techniques

As discussed in the previous sections, significant difficulties arise in applying the linearized or one-dimensional nonlinear BC to more general situations, such as flows involving mean flow gradients, nonlinearity, and viscosity. For flows where these effects are present, but small (i.e. at high Reynolds numbers and asymptotically far away from any nonuniform flow or large amplitude disturbances), the linearized BC can be applied to departures from a (known) mean flow field with little error. A common situation where this is the case is at large distance in the direction normal to the evolution of thin shear layer [194] (jets, mixing layers, boundary layers).

In situations where there is a significant nonuniform flow crossing the artificial boundary or where large amplitude disturbances are propagating out of the boundary, the linearized BC perform poorly. A canonical example is the downstream boundary of spatially evolving thin shear layers. It is difficult to even establish a clear definition of what a BC *should do* in such a flow configuration, and we must obviously exercise caution in not truncating the domain so severely that we leave out

dynamically important regions of the flow. For the purposes of this discussion, then, we restrict our attention to cases where it can be established, by physical arguments or a posteriori validation, that the flow within a certain region will be relatively insensitive to the detailed evolution of the flow upstream/downstream of the boundary, for the inflow and outflow BC, respectively.

In this section we examine *absorbing layers* where the flow physics are modified in a finite region upstream of the outflow boundary. In many cases the modifications may also be used at inflow and free-field boundaries. A number of absorbing layers have been suggested to (i) enhance the efficacy of an artificial BC or, (ii) to obviate the need for any artificial BC. Many of the essential ideas discussed here were introduced by Israeli and Orszag [234] in the context of linear wave equations. At that time, the techniques they developed were motivated by difficulties in specification of local, nonreflecting BC, even in linearized problems. For linear systems, all of the motivating issues have now been resolved in other ways (see Section 4.3.1), but the ideas have inspired a number of techniques that remain widely used in both linear and nonlinear computations.

Damping and artificial convection: Absorbing layer treatments typically provide for damping of disturbances prior to interaction with an artificial BC. Some obvious ways to do this are to introduce artificial dissipation (by upwinding), increase the value of physical viscosity (or add hyper-viscosity), and, perhaps most simply, to add a linear damping coefficient to the governing equations as

$$q_t + N(q) = -\sigma(x)(q - q_0), \tag{43}$$

where q is the vector of dependent variables, $N(q)$ a possibly nonlinear operator, $\sigma(x)$ is a spatially varying damping coefficient, and q_0 is some nominal state (zero if the equations are linear) about which disturbances are defined. In most cases σ is selected to blend smoothly between zero in the physical domain and a positive value in the layer. Disturbances are damped exponentially during their residence in the layer; σ is made large enough to attenuate the disturbances by the desired amount prior to interaction with the boundary. Whatever disturbances are reflected by the boundary are returned but similarly damped as they propagate back through the layer before reaching the domain as reflection error.

The basic problem with this approach is that the internal boundary of the absorbing layer (or the region over which $\sigma(x)$ gradually varies), *is itself* reflective [234]; without further modification, the only way to obtain a satisfactory result is to gradually increase the damping from zero over a relatively long distance. This results in thick, computationally inefficient layers.

Indeed, the PML approach discussed above in the context of linearized BC provides a way to ensure that the buffer layer is nonreflecting. In a PML one ensures that the modes of the interior equations are unmodified (except that their phase speed becomes complex such that they are damped), a concept that can only strictly apply to the linearized system. For nonlinear problems, one can anticipate that application of the linearized PML to nonlinear equations will produce the same type of quadratic error (resulting in reflectivity of the interface) as application of linearized, local, approximate nonreflecting BC. For this reason, one might question whether the additional effort of designing nonreflectivity of the layer is justified. Indeed, Freund [235] has shown that some relatively simple modifications of Eq. (43) provide reasonable results in the nonlinear case, but with thicker layers than could be achieved in the linearized case. An improvement follows from the observation [234] that as the quality of the artificial BC closing the layer is improved, the layer performance will improve (to the extent that if the artificial BC is exact then no absorbing layer is required!). One case for which exact artificial BC are available (at least for the inviscid case and ignoring discrete effects) is supersonic flow, where at the inflow all modes are incoming, and at the outflow all modes are outgoing. Following Ta'asan and Nark [236], an *artificial convection term* may be added to the equations to cause the flow to be supersonic in a layer near the inflow and outflow boundaries. In the outflow case, any waves that are not reflected by the internal boundary of the layer will not produce reflections at the outer boundary. Waves that are reflected are partly damped by the linear damping coefficient in Eq. (43) before returning to the domain. Provided the damping and convection are applied smoothly, reflections can be made small. At the inflow boundary, in fact, the damping coefficient need not be as large because waves traveling upstream are decelerated to zero speed at the sonic point, and thus their residence time in the buffer is long [235]. An additional benefit is that vortical forcing at the inflow is less damped (with the same value of σ), because the residence time for incoming disturbances is shorter.

A similar approach is that of Karni [237], where in addition to damping of waves in the layer, the convection speeds are modified by *slowing-down operators*. The concept is to allow for long residence times in the layer so that damping is effective. Their approach is also similar to PML in that they attempt to create layers that are themselves nonreflecting (applying the operators only to the outgoing waves). The nonreflectivity in this case, however, is only approximate: the decomposition (of the linearized problem) into modes is one-dimensional, but applied at an arbitrarily specified angle to the boundary (which they propose to compute locally based on information from the interior solution).

As in PML, the effectiveness of these ad hoc absorbing layers is strongly dependent on the width of the layer. They involve, however, an even greater number of parameters and profiles than PML that must be determined empirically.

Grid stretching: One can in principle obviate the need for BC by mapping the infinite domain to a finite one (which could be closed by specifying any fluctuations to vanish). For PDE with smooth (i.e. non-radiating/ advecting) solutions, such as normal boundaries in incompressible flow, such a technique is useful provided some care is taken in choosing an appropriate mapping. However, for radiating/advecting flows, waves with fixed or slowly varying wavelength propagate into the region of mesh stretching, where they become progressively more poorly resolved until they can no longer be supported by the discretization. However, as discussed in Section 4.1.7, such waves will eventually be reflected back once they become sufficiently poorly resolved that they attain a negative group velocity. If the grid stretching is infinite, then *all disturbances* will return, and *infinity is thus perfectly reflecting*!

However, provided that the poorly resolved disturbances are dissipated, either through dealiasing, artificial viscosity, or an explicit damping or filtering operator, then the dispersion associated with grid stretching can actually be an advantage, since the residence time in the region of grid stretching can be made indefinitely long by providing more gradual stretching. In other words, the stretching acts in a manner identical to the *slowing-down operator* of Karni [237]. This is hardly surprising if one considers the effect of grid stretching, say in a one-dimensional system of (inviscid) conservation laws:

$$q_t + \xi_x f(q)_\xi = 0, \tag{44}$$

where x is the physical coordinate extending to infinity and ξ is the finite computational coordinate. The Jacobian metric ξ_x will go to zero as $x \to \infty$ and to a constant value (say unity) in the near-field. If ξ is reinterpreted as the physical coordinate, then the effect is to reduce the convection speed of all disturbances to zero over the region where ξ_x varies.

Rai and Moin [238] proposed combined grid stretching and filtering as an absorbing layer for incompressible flows and the technique was applied to compressible aeroacoustic problems by Colonius et al. [194]. In both cases, the grid stretching was not infinite–the grid was stretched to large distance and then terminated with an artificial BC. In the latter work, explicit filtering of the equations was applied, but with variable coefficients so that filtering was gradually switched on only in the absorbing layer. It was shown that reflections from (nonlinear) vortical structures at the outflow could be reduced by several orders of magnitude compared to the linearized Giles [197] outflow condition. However, the absorbing layer was quite wide compared to PML. As with the other ad hoc absorbing layers, grid stretching and filtering involves several parameters and profiles that can only be determined through trial and error.

Fringe methods, *windowing*, *and a super-grid model*: In the fringe method developed for spatially evolving boundary layers by Spalart [239] and widely applied thereafter, the need for any inflow and outflow artificial BC is obviated by using periodic BC and an absorbing layer to modify the flow near the boundary before it is recycled back as inflow. A linear damping coefficient analogous to that in Eq. (43) is added to the right-hand side of the momentum equations. The difficulty is in specifying the appropriate q_0. It is suggested that the streamwise velocity be driven to a solution of the Navier–Stokes equations (for example a two-dimensional laminar boundary layer solution), and made periodic by choosing:

$$q_0 = Q(x,y) - (Q(x-L,y) - Q(x,y))S\left(\frac{x-L+\varDelta}{\varDelta}\right), \tag{45}$$

where q now denotes only the streamwise velocity, $Q(x,y)$ is the (approximate) laminar solution, and $S(x)$ is a smoothed step function that varies between zero at the start of the buffer (at $x = L - \varDelta$) and unity at the edge of the periodic box (at $x = L$). In using a Fourier spectral method, it is important to ensure that blending functions preserve, to machine roundoff, both periodicity and continuous differentiability. Combinations of Gaussian or hyperbolic tangent functions are typically used. The transverse component of velocity should be specified so that the target velocity is divergence free (in the incompressible case).

The fringe method was recently analyzed in detail, in a linearized framework, by Nordström et al. [240]. By carefully choosing constant coefficient model equations, they are able to argue (and confirm a posteriori with numerical experiments of the full problem) that the periodic fringe method converges (at least in incompressible flow) to the inflow/outflow problem. Specifically, they show that disturbances are appropriately damped prior to recycling at the inflow, and that the upstream influence of the fringe is small.

A different approach to using periodic BC with an absorbing layer is the spatial windowing of the equations proposed in Guo et al. [241] and revisited recently by Schlatter et al. [242]. Here the governing equations are *windowed*:

$$w(x)q_t + w(x)f(q)_x = 0 \quad \text{or}$$
$$\tilde{q}_t + (w(x)f(q))_x = w'(x)f(q), \tag{46}$$

where the one-dimensional case is written here for simplicity. Here $w(x)$ is the window function, which is zero at the edges of the domain, rises to unity over the fringe and is unity in the interior. $\tilde{q} = w(x)q$ are

windowed variables. Provided that the window function meets certain differentiability and periodicity constraints [241], similar to those on $S(x)$, then a Fourier spectral expansion for $\tilde{q}$ is appropriate and spectral accuracy is retained. In general, q cannot be exactly recovered from $\tilde{q}$ since $w(x) = 0$ at the boundary.

In the special case when the desired flow near the boundaries consists of a uniform base flow plus perturbations, then a regularized *de-windowing* operation has been suggested: $q \approx \tilde{q}$, for which Eq. (46) can be written

$$\tilde{q}_t + w(x)f(\tilde{q})_x = 0, \tag{47}$$

which is exactly analogous to an infinite grid stretching. This also makes it clear that disturbances will need to be dissipated as they interact with the fringe, so that they are not ultimately aliased back into the interior. As the BC is now periodic, dealiasing is an option, although Colonius and Ran [219] find that providing an additional absorption of disturbances in the fringe is much more effective than dealiasing alone. Guo et al. [241], for example, suggest adding a linear damping coefficient term (Eq. (43)) in the fringe. When it is desired to have some specified inflow velocity profile, then the de-windowing operation needs to be modified; Schlatter et al. [242] suggest using $q \approx (1 - w(x))q_0 + \tilde{q}$, where q_0 would be as specified for the fringe method, Eq. (45).

In fact, there is a strong analogy between modeling the effect of windowing with the traditional turbulence modeling problem [219]. In turbulence modeling, the concern is with disturbances that become (as the result of nonlinear processes) too fine to be represented on the mesh in physical space. It is well known that dealiasing (i.e. by using the Galerkin method or by explicit dealiasing of the nonlinear terms) allows this energy transferred to small scales to be removed from the computation, but in a process that is not in general a good model for the true energy cascade. In LES, for example, the governing equations are filtered, and a sub-grid model is supplied, in essence, to recover the unfiltered variables (needed in the nonlinear terms) from the filtered ones.

Filtering, in physical space, corresponds to *windowing* in Fourier-space, and vice versa. By windowing, scales that are *larger* than the extent of the domain are filtered. Thus by analogy with LES, one should also supply a *super-grid model* to correct for the unphysical effects of domain truncation. One way to do this would be to develop a more sophisticated de-windowing procedure (e.g. [242]). A different approach [219] is to use $q \approx \tilde{q}$ and then *filter* equation (47) in physical space (a step that is necessary for LES anyway). This is tantamount to de-windowing since, by analogy with grid stretching and slowing-down operators, large scales are continuously shortened as they propagate into the fringe. Once

filtered, one is presented with the standard LES modeling for the nonlinear products in $f(q)$, as well as additional products of the window function and the fluxes. For the latter, Gaussian filtering and the tensor diffusivity model [243,244] were chosen. Some additional modifications were needed to ensure that the model is globally diffusive.

Results from model problems show reasonably good transparency of the boundary using the super-grid model. Figs. 16 and 15(g) compare the performance with other BC for propagation of a nonlinear vortex in uniform flow and radiation of an acoustic pulse in free-space, respectively. For the acoustic pulse, the performance is, for an equivalent number of points in the layer (and hence comparable cost) a little better than PML. For the nonlinear vortex, a ten point layer gives reflections that are 1000 times weaker than the vortex, regardless of the vortex strength, even when the vortex is sufficiently strong to induce inflow at the outflow boundary (a case for which most BC fail, as mentioned in Section 4.3.2).

Additional tests and comparisons are presented in Refs. [219,245]. In the latter, linear, inviscid disturbances to a ducted uniform shear flow were considered. This flow represents a significant challenge for BC because repeated reflections of the initial waves from the walls decay only slowly in time, and errors from early reflections can dominate the solution at later times. The super-grid model showed convergence to the exact solution as the buffer layer was increased, even for cases where the maximum velocity was supersonic (such that there was a sonic point along the inflow and outflow boundaries). However, very large buffers (more than 128 points) were required for reasonable error levels. The PML layer developed by Hagstrom and Nazarov [215] for sheared flows performed well with many fewer points. However, when the speed of the shear was increased such that there was a sonic point at the boundary, the PML technique was unstable.

It can certainly be argued that there is no reason, at this stage, to prefer the windowing/super-grid models to other ad hoc absorbing layers discussed above. The performance is good, but roughly equivalent to what could be obtained by optimizing the parameters and profiles in other treatments. On the other hand, the super-grid model has fewer tunable parameters than other models [219]. One can reduce the problem to two scalar parameters. The first is the number of points across the layer, the second is maximum slope of the windowing function, $w(x)$ across the fringe. Properly scaled, there is only a small range of values that can be chosen for the slope, and the results are not particularly sensitive to the choice. Aside from requiring fewer tunable parameters, the analogy with turbulence modeling may provide a needed framework in which other (better?) models can be used.

4.3.4. Solid wall boundary conditions

Rigid solid boundaries are represented by the no-slip condition, which specifies that there is no relative motion between the fluid and solid. For energy conservation, the most common approximations are that the solid is isothermal or adiabatic. Thus for viscous three-dimensional flow, we have four physical BC, which is the correct number for well-posedness of the initial boundary value problem [226]. For the discretized equations, the fifth variable must be inferred by either satisfying the equations of motion (using one-sided differences where necessary), or by extrapolating the value from the interior.

To specify the fifth variable, Thompson [222] and Poinsot and Lele [223] suggest an extrapolation procedure based on a one-dimensional analysis of the acoustic reflection problem at the interface, imposing rigidity of the boundary by perfect reflection of waves with normal incidence. In the framework of Eqs. (40) and (41), one simply sets the sole incoming characteristic amplitude, $\mathscr{L}_4$, equal to $\mathscr{L}_3$ (whose value is computed using one-sided FD), and inserts the result into the continuity equation, computing other differences (derivatives tangent to the boundary) using the interior FD scheme. For non-planar boundaries, this procedure can also be applied to body-fitted, generalized coordinate systems [246,247].

While the Thompson approach leads to a stable discretization that has been widely used, the one-dimensional analysis for the extrapolated variable is not strictly needed. One can simply solve the continuity equation at the wall using one-sided differences for the wall-normal derivatives velocity and density. However, great care must be taken in specifying the differencing–certain treatments can lead to instabilities and, especially in the inviscid case, to trapped spurious waves (see Section 4.1.3) in the near wall region [248]. Tam and Dong proposed a technique for stable discretization of the pressure gradient in the wall normal direction that involves continuing the exterior grid into the body and placing a row (or rows) of ghost points inside the body. Once the normal pressure gradient is determined on the extended grid, other terms in the equations at the boundary are specified by consistency with the governing equations and the no-slip and isothermal (or adiabatic) conditions, or simply the no-penetration condition for the inviscid case. Hixon [249] extended the ghost point approach to body-fitted, generalized curvilinear coordinates. Barone [250] presents a similar implementation for compact finite-difference schemes.

A different approach to solid wall BC is needed in conjunction with *immersed-boundary* methods. Here the body is allowed to traverse a regular Cartesian mesh, and computational cells (or points) are divided into those wholly within the fluid or body, and cells partially occupied by the body. There are a wide variety of techniques (though primarily developed for incompressible flows); we mention only two schemes that have been specifically developed for CAA applications. The first is an extension of the ghost point method [251] that is applied to acoustic scattering problems solved using linearized Euler with no ambient flow. Some artificial viscosity is added to damp spurious waves that are generated by the irregular surface topology. An alternative formulation for scattering problems is the *impedance mismatch method* [252,253]. Essentially the solid is replaced by another fluid of high impedance so that the interface approximates a reflecting, rigid surface. The sharp gradients in acoustic impedance also require some artificial damping so that spurious wave generation is controlled.

4.4. Shocks

Shock waves play a role in many relevant aeroacoustic problems, but are a particularly troublesome flow feature represent numerically. As already discussed, capturing sound generation by turbulent flow necessitates the use of high-order accurate and/or optimized finite difference schemes with low artificial dissipation. Shock capturing schemes, on the other hand, invariably rely on lower-order differences and the introduction of some smoothing, or dissipation, in at least a local region surrounding the shock.

The primary difficulty stems from the fact that strong shocks have thickness that is of the order of a few mean free paths of the medium, despite which the structure of the shock is surprisingly well modeled by the continuum viscous, heat conducting compressible equations of motion. These in turn provide an estimate for the shock thickness, which is typically much smaller than the smallest turbulent scales; a useful estimate, provided by Mahesh et al. [254] is

$$\frac{\lambda_1}{\delta} = \frac{R_\lambda}{5.1} \frac{(M_1 - 1)}{M_t}, \tag{48}$$

where λ_1 and δ are the streamwise Taylor microscale and shock thickness, respectively, R_λ is the turbulent Reynolds number (using the Taylor microscale and streamwise velocity fluctuations), and M_1 and M_t are the upstream Mach number and fluctuation Mach number respectively. Obviously direct resolution of the shock thickness will be limited to values of M_1 near unity.

The alternative is to allow the shock thickness to be much smaller than the grid spacing, and provide an artificial viscosity so that the discontinuity does not produce undesirable (and destabilizing) oscillations. Such shock capturing schemes have been developed for many years, and, especially in multidimensional unsteady flow, they remain an area of active and rapidly evolving research with their own vast literature. We

provide here only a brief outline of the methods that have been applied to relevant sound generation problems. The references should be consulted for a more accurate representation of the literature leading to the developments cited here.

Early attempts to add linear diffusion terms to the governing equations (similar to the artificial viscosity terms discussed in Section 4.1.3) have been largely superceded by so-called Essentially-non-oscillatory (ENO) schemes to evaluate the fluxes in conservation laws. The method was developed in a series of papers by Harten, Osher, Shu and co-workers [255–258]. At the heart of these schemes is a flux splitting (independently in each grid coordinate) of the equations into upwind and downwind modes (labeled by the sign of the eigenvalues of the flux Jacobian). In turn, correctly biased difference formula provide the correct sign of artificial dissipation to either wave. The main difference with a standard flux splitting is that the stencil and coefficients of the differencing are dynamically changed based on the smoothness of the underlying function, and this allows one to optimize the accuracy in differencing the smooth parts of the solution adjacent to the shock. ENO schemes involve a set of logical statements to evaluate smoothness. A speed up can often be obtained by eliminating such logical statements, and this can be accomplished by using a weighted average of *all* possible stencils (and coefficients) up to a certain order of accuracy. These so-called Weighted-ENO, or WENO, schemes have been extensively developed in a series of articles (see, for example, [259–261]).

In addition to the spatial discretization, the temporal discretization can be modified to provide shock capturing benefits. We briefly mention the so-called "Total Variation Diminishing (TVD) Runge–Kutta schemes (e.g. [257]) that are similar in spirit to the optimized LDDRK schemes discussed in Section 4.2. The coefficients of the various stages can be chosen in order to yield a TVD scheme, while simultaneously minimizing the required function evaluations. The reader should consult [257] for a more detailed presentation of the theory (and literature) for these schemes.

Even with these advanced shock capturing methods, there is still a significant accuracy penalty if they are used in regions away from shocks. As was discussed in Section 4.1, compact and optimized FD schemes are specifically developed to allow accurate computation with relatively few grid points per wavelength of the underlying function. These *small scales* are rapidly dissipated even by higher-order (such as 5th or 7th) WENO schemes [262]. Thus for a fixed stencil size, more grid points would be required to accurately compute a turbulent flow with high-order WENO schemes as compared to low or non-dissipative compact and optimized schemes.

Attempts to alleviate this problem fall (for the most part) into two categories. WENO schemes with compact

(Padé) stencils can be used to achieve higher-order-accuracy [263,264], and optimized schemes can be used to trade-off formal order-of-accuracy for better performance at high wavenumbers [265,266]. Another option is to limit the use of the shock capturing differencing to regions near discontinuities. In computing DNS of shock-turbulent interactions, Lee [267] and Mahesh [254] choose to apply the ENO schemes in a thin region surrounding the (known) shock location, reverting to high-order compact FD schemes away from the shock. Adams and Shariff [268] generalized this technique to turn on the ENO schemes around discontinuities dynamically. Recently, Pirozzoli [262] has developed a similar technique, but using WENO schemes and a conservative flux-differencing. In smooth regions of the flow, he uses an optimized compact upwind scheme, and 5th and 7th-order accurate WENO at discontinuities. Tests with many model problems, including shock-turbulence interaction, show the benefits of this approach.

A principal difficulty with these *hybrid* shock capturing methods is that switches need to be devised that accurately determine where to engage the WENO scheme. These can be implemented with varying degrees of sophistication, but the basic problem is that it is difficult to assess whether *jumps* in the solution are due to actual discontinuities, or merely small-scale (but smooth) features of the flow. Nevertheless, the past decade has seen significant advances in the development of high-order shock capturing techniques, and this remains an active research area.

5. Recent progress in nonlinear CAA

It would be difficult to present concisely the full range of the nonlinear problems in CAA that are presently being studied. Our interest in this section is to highlight certain problems where computational approaches have led to better understanding of the physical mechanisms of sound generation, or which highlight technical difficulties with aeroacoustic theory or computational methodologies that were discussed in the previous sections. We are led to consider in some detail (i) sound generation due to isolated vortex dynamics and interactions of vortices with shock waves, (ii) model problems related jet noise, and (iii) model problems related to cavity noise. A specific discussion of airframe noise is not given but the relevant issues were discussed in Section 2.3.1.

5.1. CAA studies related to vortex dynamics and interaction of vortices with shock waves

Problems of nonlinear sound generation are substantially simplified, both physically and computationally,

when vortical regions or thermal inhomogeneities (e.g. entropy disturbances) are compact (rather than extensive as is the case in jets and other turbulent shear flows). Such isolated disturbances may generate acoustic waves, either through their own intrinsic dynamics, or through interaction with solid boundaries or shocks. Examples we discuss here are interactions of two vortices (co-rotation, leapfrogging, pairing, etc.), collisions of vortex rings, and interactions of vortices and thermal inhomogeneities with acoustic waves and shocks.

There are three important reasons to study these model problems. First, and most relevant to the present review, is that they can often be treated analytically and thus serve as useful validation problems for CAA codes. Even when analytical solutions are not available, run times are generally short enough so that many runs with different values of computational and physical parameters can be made. These computations can be used to isolate certain features of the sound generation process and examine, for example, whether artifacts of discretization have an impact on the sound generation process. Secondly, application of Acoustic Analogies to these problems is often more straightforward than for flows with extensive vortical regions, due to the absence of flow/acoustic interactions. Thus they can serve to validate the hybrid CAA methodologies discussed in Section 3. Finally, they are interesting problems in their own right, and offer clues about the mechanics of sound generation in more general flows.

Interactions of vortices have been considered in both 2D (line vortices) and 3D (vortex rings). Mitchell et al. [33], considered the sound radiated by co-rotating vortices (in 2D) by solving the full compressible Navier–Stokes equations with the compact sixth-order FD scheme (C6), fourth-order RK time advancement, and one-dimensional characteristic BC were used (see Section 4.3.2). The mesh was highly stretched between a near-field, with nearly uniform spacing, and a far-field that extended to several wavelengths of the radiated field. A significant computational difficulty was the resolution of sharp initial transients that must propagate through the stretched mesh in order to be eliminated from the computation. Special care had to be taken to filter these transients from the computation, at least initially, so that large spurious reflections from the grid stretching (see Section 4.1.7) did not contaminate the solution. After the initial transient passed, the sound radiated by the vortex co-rotation was fully resolved on the (stretched) mesh. The acoustic field was computed directly so that the accuracy of acoustic analogy predictions, with sources based on the near-field, could be established. The relevant parameter that determines the acoustic compactness of the radiation is the Mach number of co-rotation, M_r. Two cases were considered, a compact case with $M_r = 0.06$ and a less compact case with $M_r = 0.18$. For the compact case, a variety of

different formulations for the equivalent acoustic sources led to very accurate results: Powell's source, a modified version of the Lighthill tensor,[12] and notably vortex sound theory. In the less compact case, the directly computed acoustic radiation was also in good agreement with acoustic analogies provided that compact source assumptions were not made in defining the acoustic sources. The study demonstrates how computation can be a valuable tool in assessing the validity of approximations to the equivalent sources.

Axisymmetric computations of the (head-on) collision of two vortex rings were performed by Inoue et al. [269] using a similar numerical method, except that the stretching/filtering *sponge* boundary treatment [34] was used (see Section 4.3). Various cases with both equal and unequal strength rings, and different Mach numbers, were considered. The acoustic field was directly computed, and the equivalent acoustic sources due to Möhring and Powell were computed assuming acoustic compactness. The acoustic field was found to be closely related to the (rapid) change of direction of the vortex ring motion associated with stretching of the rings during their interaction. The results were different by as much as a factor of 2 (as well as having fewer peaks) compared to experiments at higher Reynolds number [270]; aside from a possible Reynolds number effect, a variety of causes for the discrepancy such as enforced axisymmetry, and difference in core size or vortex structure between computation and experiment were suspected.

In many other computations, the near-field was computed independently of the acoustic field (usually assuming incompressible flow) and vortex sound analogies were subsequently used to compute the equivalent acoustic sources. A variety of techniques can be used to compute the vorticity field, ranging from full DNS to inviscid computations of vortex dynamics using vortex filaments, patches, contour dynamics, etc. These latter techniques have in fact been used to investigate sound generation for more than 30 years. Recent examples include the detailed contour-dynamics computations of Tang, Ko, and co-workers (e.g. [271] and references therein), who have investigated a wide variety of configurations of vortex pairs and rings and highlight the different roles played by the dynamics of the vortex centroids and *microscopic* cores in sound generation during leapfrogging and merger.

We turn now to problems involving the interaction of vortices with shocks. The sound generated in such interactions is relevant to broadband shock associated noise in imperfectly expanded jets and other flows such as pulsatile jets from an automotive exhaust. The model

---

[12]The steady slowly decaying velocity field due to finite circulation, which would otherwise render the Lighthill source divergent, was removed prior to integration of the source.

problem of the interaction of an isolated vortex, or vortex pair (or ring) with a nominally normal shock as it is convected through the shock highlights the physical phenomena common to more complex flows. The problem of the interaction of vortices in a shear layer with an oblique shock is discussed below in Section 5.2.2. The interaction depends on the respective strengths of the vortex, say its maximum swirl velocity V_m, and the shock wave. The latter can be characterized by the relative pressure rise across the shock $\Delta p/p_1$, or the upstream Mach number M_1 (in a shock-fixed frame), or the speed of the shock V_s (in a fluid at rest). When $V_m \ll V_s$ the interaction is weak, and the shock shape is mildly perturbed. However when $V_m \gtrsim O(V_s)$ the shock is strongly distorted and shock focusing and multiple-shock fronts with triple-points and slip-lines (free-shear layers) can result. For the problem involving a vortex-pair the mutually-induced velocity can be either in the same direction as the shock propagation, called 'passing pair', or opposite direction, which is termed 'colliding pair' [272]. This distinction also applies to the vortex-ring problem.

The isolated vortex–shock interaction problem has been computed using a variety of numerical techniques. Meadows et al. [273] used an upwind second-order shock-capturing scheme, Ellzey et al. [274] used the FCT scheme, Meadows and Caughey [275] used the ENO scheme, and Grasso and Pirozzoli [276] applied the WENO scheme. Inoue and Hattori [272] used the sixth-order compact scheme to study shock-vortex interaction by numerically resolving the shock profile; only weak shocks were considered. Besides the discretization method and good non-reflecting boundary conditions surrounding the computational domain, two additional numerical issues are important in this problem. It is advantageous to maintain a steady shock at a fixed location in the computational domain, in absence of free-stream perturbations. This is computationally difficult if non-reflecting boundary conditions are desired on the lateral boundaries. Even with periodic lateral boundary conditions the mean shock profile displays a small but consistent drift [277], which is a physical effect [278,279]. One possibility is to stabilize the location of the shock by imposing a mild stream-tube area variation (small divergence) along the free-stream [273]. This, however, must be consistently treated in the specification of free-stream disturbances. Meadows et al. [273] impose the inviscid no-penetration boundary condition on the lateral boundary, which reflects sound waves and also generate steady Mach waves that complicate the interpretation of the results. An alternative is to use the absorbing sponge treatment with a reference base-state including the desired shock profile. The latter is used in studies of the interaction of oblique shocks/compression waves with a shear layer discussed in Section 5.2.2. The other numerical issue is

the modeling of the 'vortex'. The slow r^{-1} decay of the induced velocity associated with a vortex has motivated the use of vortex models that provide a fast decay of the azimuthal velocity [272,273,275,276,280]. It is common to use a swirling flow profile (used by Taylor) with zero net circulation[13] to achieve an exponentially decaying induced velocity. Such models highlight the interaction of the shock with the vortex-core and reduce the 'precursor' associated with the slowly decaying potential flow induced by the vortex [281]. The axisymmetric problem of the interaction of a shock with a vortex ring naturally eliminates the problem associated with long-range interactions and has also been studied using shock-resolving simulations [282] and with shock fitting [283]. The latter allows a treatment of stronger shocks but the vortex strength must be limited to ensure that the one-dimensional Rankine-Hugoniot relations are maintained on the perturbed shock-front.

These studies have confirmed Ribner's theoretical prediction [281] of a quadrupolar acoustic wave generation and the 'precursor' and 'vortex–core' interactions. The linear theory, however, is valid only for weak-interaction; nonlinear effects are easily triggered by strong vortices and have been the focus of simulations. The overall interaction generates a succession of compression and expansion waves and their origin has been related to the details of the shock dynamics near the vortex core [272,275,276]. Geometrical theory of the interaction of weak shocks with an inhomogeneous medium [284,285] may be useful in further study of these phenomena. The generated waves also interact with each other when there is line of symmetry present [282,283,280] which leads to more complex near-field patterns. The interaction compresses the vortex core upon passage and excites oscillations in the vortex-core (core nutation is observed in two-dimensional simulation [276]. Three-dimensionality is known to be important in the dynamics of vortex core and its role in shock-vortex interactions remains an open area for future work. The shock-vortex interaction leads to entropy generation as well as new baroclinic vorticity. The latter is subject to the Kelvin–Helmholtz instability and may rapidly roll up and create secondary vortices. The non-uniformity of entropy in flow downstream of the interaction is essential in correctly interpreting the patterns in thermodynamic variables (slip lines show a change in entropy and density but not in pressure). In this context it is also useful to recall the general linear theory of the interaction of inhomogeneous flow with a

---

[13]An exception to the is the study by Ellzey et al. [274] that uses a finite circulation vortex with a solid body core, i.e. a Rankine vortex. They use a long streamwise domain but impose periodicity in the lateral direction, in effect studying the interaction of the shock with a periodic array of Rankine vortices.

shock [286,287] that treats the problem of sound-generation as well. These theories have been very helpful in explaining the results obtained in DNS of shock-turbulence interaction [277–289]. Even though there is no clear 'radiated acoustic field' in these problems since the homogeneous turbulence is present everywhere, the notions of evanescent and radiating modes are helpful in explaining the behavior of near-field 'turbulence' comprising of vortical, acoustic and entropic disturbances. The interaction of any one mode of disturbance with a shock generates all three modes downstream and they are coupled, at least in the near-field of the interaction.

5.2. CAA studies related to jet noise

The noise of high-speed propulsive jets consists of the turbulent jet-mixing noise, shock-cell noise when the jet is imperfectly-expanded and contains tonal components (jet-screech) and broadband shock-associated noise. In practice engine noise includes 'excess' noise that includes the internal mixing noise, core-noise from the combustor and turbomachinery, and the additional noise due to the interaction of the jet flow with nearby airframe components. Technical reviews of jet noise are available [290–292,15] and should be consulted for details. The proceedings of the recent Jet Noise Workshop [293] provides a recent perspective of this field. Key features of jet noise are noted in this section along with the current understanding of the underlying noise source mechanisms. Examples from recent work on high-fidelity numerical simulations are given and the progress toward physics-based prediction methods is summarized.

5.2.1. Representation of jet turbulence and jet mixing noise

Jet flows contain both quasi-organized large-scale motions reminiscent of instability waves or wave-packets, and more irregular small scale turbulent motions. The differing characteristics of the sound radiated by organized and irregular motions has been appreciated for many years, but there is as yet no comprehensive theory that employs a formal decomposition. Methods such as the wavelet decomposition [294] and proper orthogonal decomposition [295] are being applied to jet flows and their noise, but at present the available information is limited [296–299].

One of the following two *extreme* views[14] is commonly adopted for the jet flow:

- (A) *all fluctuations represent turbulence*; no explicit representation of the organized wave packets [19,302,23,25,303] is used,

---

[14]With notable exceptions of Liu [300] and Michalke [301] and references therein.

- (B) *all large-scale motions or 'large-scale turbulence structures' correspond to instability waves* [304–308]; turbulence is assumed to only contain 'fine-scale' components [85].

Viewpoint-A is purely statistical and leads to a representation of turbulence-associated noise sources in terms of space–time correlations. Lighthill [30,309,310] adopted this view. Statistical representations of acoustic sources have been sought in many studies [29,311,312] including recent work [313,314]. Many studies take into account the effect the jet mean flow has on the radiated noise, a feature shared by Tam's fine-scale noise model [85], also see [315]. Although a statistical representation does not rule out the presence of orderly structure in jet turbulence, this information is not explicitly reflected in current models.

Viewpoint-B treats the dynamics of *large scales* as instability-wave packets.[15] This requires the mean flow to be specified, or predicted. RANS equations, sometimes with adjusted model coefficients, are often used. Integral methods are used to represent the nonlinear interactions between the wave packet and other 'background' disturbances, including finer-scale turbulence [320,308,321]. It is arguable if an accurate prediction of instability-wave packets can be managed efficiently within the framework of a small set of interacting modes, such as the nonlinear disturbance equations NLDE [322] or nonlinear parabolized stability equations NPSE [323]. Recently using PSE Bertolotti and Colonius [324] identified the potential importance of supersonically convected entropic nonuniformities in the core of a heated jet (called 'core modes') to the noise radiation. NPSE has also shown remarkable accuracy in strongly nonlinear two-dimensional shear layers [325]. Noise radiation predictions using NPSE are under development [326]. DNS data from a supersonic turbulent jet [327] also reveals the importance of nonlinearity for modal amplitude prediction.

Tam et al. [328] show that far-field jet noise spectra are well described by two empirical spectra, one attributed to large-scales and the other to fine-scales. There is, however, no experimental evidence of a scale-gap between large and fine-scales in turbulent jets. Jet turbulence is intrinsically a continuous-spectrum, multi-scale phenomena. Hence the predictions of the noise radiated by the large scales need to be combined with

---

[15]The large-scale eddy structure in jets has been linked to the linearized instability characteristics of the mean flow [308,316]. A flow disturbance at a fixed frequency initially grows in amplitude and subsequently decays due to mean flow spreading and nonlinear interactions, giving rise to a *wave packet* with a carrier wavenumber and modulation amplitude that change slowly along the jet [317]. This modulation results in noise radiation from subsonically convected *instability wave* disturbances [300,318,32,319].

models for the noise radiated by intermediate and fine-scales. Goldstein [74] suggests that the two components of jet noise can be rationalized as two distinct types of flow response: one associated with the direct radiation from the bulk distribution of acoustic sources attributed to jet turbulence, and the other associated with an instability-wave response in a slowly-varying non-parallel jet mean flow. The latter radiates preferentially at small angles to the jet axis and the former contains a broad range of frequencies. A noise prediction method incorporating these notions is not yet available.

There are other distinctive features of jet mixing noise for which are at present not satisfactorily understood. For example the frequency of peak radiation (at small angles to the jet) does not follow a Strouhal scaling, and data [27,26,329] indicate that it is *not* dependent on the jet exit velocity! Different proposals exist in literature on the effects of jet temperature, and how they should be modeled in a jet noise prediction method. The reader is referred to articles that focus on jet noise [15,330,329] for further discussion of the open issues in jet noise modeling.

A computational alternative to the methods based on specific decompositions/representation of turbulence is to lump all disturbances together and model only the unresolved-scales. This sidesteps the issue of wave-packet/irregular turbulence decomposition and is the general approach of large-eddy simulation (LES). Significant progress in the use of LES for jet noise predictions has been made recently [331,332,98,119] (see Fig. 17 as an illustration) and new insights on noise generation in turbulent jets are expected from such studies in the next few years. The present status of DNS/LES for jet noise is discussed in Section 5.2.3.

5.2.2. Jet screech and shock-associated noise

Imperfectly expanded jets produce additional noise due to the interaction of the jet turbulence, particularly its large-scales, with the shock-cell structure existing within the jet. Its tonal components called jet screech, requires a feedback loop [333]. Tam's review [15] discusses the present physical understanding of these noise components. At the nozzle lip *embryonic* shear-layer disturbances are generated, which convect and amplify in the developing shear-layers. Their interaction with the second/third shock cell generates acoustic waves that travel upstream to the nozzle lip and close the loop. The phase criterion for constructive reinforcement over the feedback loop provides a formula for the frequency of screech tones with good agreement with data (see [334]). However, predictions of screech amplitude, its directivity and the nonlinear staging phenomena are not available [15]. Developing methods for noise predictions in flows involving a resonance, including jet screech and cavity flows, is an area of active research.
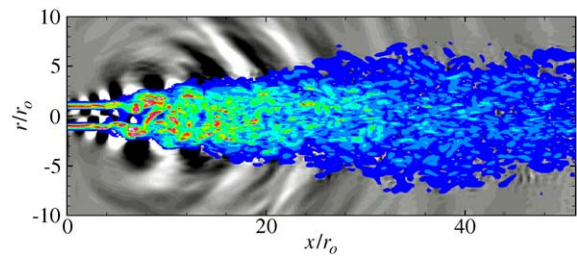

Fig. 17. A composite visualization of an unheated turbulent jet at $M_j = 0.9$ and its sound radiation obtained by LES from Bodony and Lele [119]; Color contours show the vorticity magnitude and highlight the jet turbulence. The grey scale contours represent dilatation and show the acoustic wave radiation.

Shock-associated noise is typically most intense in the direction upstream to the jet and exhibits spectral bumps with peak frequency increasing with the inlet angle χ. Harper Bourne and Fisher's pioneering study [335] explained these features using a phased array of simple noise sources located at the end of each shock cell, and phased according to the convective time delay for a turbulent eddy to pass over each shock cell. The Lagrangian correlation time limits the spatial coherence of the noise sources. Tam and Tanna [336] noted that a phased-array of simple sources predicts noise radiation at harmonically related tones that are not observed, and proposed a distributed-source model for the shock-cell noise generation. In their model the turbulent motions are regarded as stochastic instability waves (viewpoint B). Its non-linear interaction with the wave-guide modes (representing the shock-cell structure) radiates sound. This interaction implies flow disturbances with up-stream-directed supersonic phase speed and results in upstream-directed Mach waves. Specific frequencies radiate preferentially at particular angles from the inlet axis. This basic model was given a firm mathematical foundation in later work by Tam [307], who also gave a semi-empirical formula for predicting the shock-cell noise, and showed its effectiveness with detailed comparisons to the narrow band shock-cell noise measurements by Norum and Seiner [337] and others. This semi-empirical model has been refined further [338,339] and represents the present state-of-the-art in shock-cell noise prediction.

Despite its success, some significant limitations exist in this model. The noise prediction is based on an *assumed* spatio-temporal distribution of near-field pressure disturbances that are supposed to result from a nonlinear interaction between the large-scale instability waves of the jet and its shock-cell structure. The former is modeled with a Gaussian wave packet shape and the latter is an empirical modification of the Prandtl-Pack solution.

In principle LES can be used to study the noise-generation mechanisms in an imperfectly-expanded jet, but this is computationally demanding. Besides representing the multi-scale jet turbulence, the shock-cell structure that involves steep gradients in the early jet, would also need to be accurately captured. Such a calculation is yet to be attempted, but detailed study of related model problems [340,40] has provided insights into improving shock-cell noise prediction methods.

5.2.3. Computation of jet noise using DNS and LES

Computational studies that aim to contribute to an improved understanding of jet noise sources need to first establish that the turbulence dynamics is adequately captured by the simulation. Direct numerical simulation (DNS) of the jet turbulence requires very few a priori assumptions, and hence can serve as a testbed for noise source modeling ideas. Recent work of Freund [36,35] is illustrative of what is currently feasible with DNS. However the computational cost involved in DNS of jet turbulence is very large, see [341] for a detailed estimate of the resolution requirements. As discussed in Section 2.3.2 the range of spatial and temporal scales in a turbulent jet increases rapidly as the jet Reynolds number is increased. This places practical limits on the jet Reynolds number in DNS to rather low values. Fortunately, jet noise experiments, e.g. in Seiner [342], show that many attributes of jet noise are not strongly dependent on Reynolds number. This gives reassurance that the noise-generation physics can be revealed by detailed computational studies even if the Reynolds number is limited.

The frequency bandwidth of turbulent motions in current jet DNS is quite limited and consequently so is the spectrum of radiated noise. The severe resolution requirements associated with capturing the thin shear layers in the near-nozzle region motivate the use of relatively thick early shear layers. Due to this a significant portion of the jet flow is dominated by unsteady laminar/transitional flow. Realistic turbulence develops quite late, approximately where the shear-layer from opposite sides of the jet have begun to interact. This results in turbulence spectra with limited band-width, especially in the region of the potential core closure, which in turn is regarded as the region of dominant noise-production. The quasi-laminar shear-layers also imply that the higher frequency noise that is associated with the turbulence in the thin-shear layers is also missed in the calculations.

These limitations notwithstanding DNS studies of a high speed turbulent jets have provided a rich database of useful information [36,343,35]. The overall features of the flow, such as the mean flow profiles, the rate of spreading of the jet, turbulence profiles, and overall SPL and its directivity are in remarkable agreement with the available experimental data [344] (at low Reynolds numbers). Also reported was an analysis of the noise-sources based on Lighthill's formulation, such as the spatial distribution of sound-source strength and its frequency-wavenumber dependence. It is intriguing that the source-distribution responsible for the dominant noise radiation from this turbulent jet has a very simple wave-packet structure. At present it is not known whether this simple source structure would persist if the early shear-layers of the jet were also turbulent, but this is a distinct possibility. There is experimental evidence for wave-packet-like source distributions. Laufer and Yen [345] and Crow [346] interpreted their jet noise measurements in terms of a line-antenna model of the jet. Crighton [1] analyzed the noise radiation from the jet's orderly structure in terms of a wave-packet model, and this idea has been exploited by Fuchs and Michalke [347]. Crighton and Huerre [319] developed the model problem of radiation from a wave-packet further and characterized its radiation as 'superdirective'. Colonius et al. [34] also found that the noise radiation from organized vortex-pairings could be represented as a 'superdirective' radiation from a wave-packet. Further analysis of the data gathered from such DNS/LES studies of jets will be forthcoming and this will provide a fertile ground for developing new source approximations, and for developing hybrid methods for computations and noise predictions. An interesting use of jet DNS data is reported by Freund et al. [348]. The time dependent data was filtered to remove the scales containing most of the turbulent kinetic energy via spatial filtering and the dynamics of the very-large scales were studied. This severe filtering did not affect the dominant low-frequency noise radiation from the jet confirming the importance of very-large scales to noise radiation.

Development of LES for aeroacoustic predictions is an active area. Appropriate treatment of turbulent inflow, SGS models, and noise models for the scales not captured in LES are being pursued. Control of numerical errors is very critical in such calculations. Constantinescu and Lele [98] conducted the LES of a near-sonic jet using high-order compact finite difference schemes. They devised a special treatment of the governing equations near the cylindrical co-ordinate singularity [349]. They note that as the Reynolds number of the jet is increased a problem associated with energy accumulation near the grid scale is encountered. This is attributed to aliasing errors from non-linear terms; the sub-grid model alone is not sufficient to prevent energy pile up. A spatial filtering of the solution, with an eighth-order compact filter [162], is applied every 200 time steps. This procedure is adopted in further work [119]. A recent study of jet LES by Bogey and Bailly [350] relies entirely on high wave number filtering as a surrogate SGS model with striking results on jet turbulence and noise.
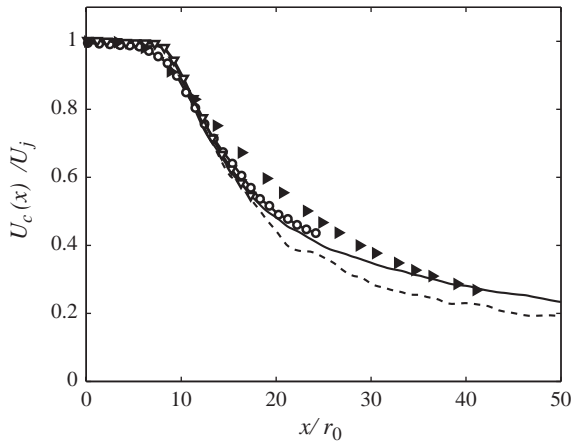
Fig. 18. Time-averaged axial velocity along the centerline of an unheated, $M_j = 0.9$ jet, from Bodony and Lele [119]; — LES with 10^6 points; - - - - LES with 10^5 points; ○ Freund [36]; ▽ Bogey and Bailly [331]; ► Zaman [23].

Fig. 19. Centerline root-mean-square streamwise fluctuations for an unheated, $M_j = 0.9$ jet, from Bodony and Lele [119]; — LES with 10^6 points; - - - - LES with 10^5 points; ▽ Tanna at case sp7 [416]; Bogey and Bailly [331]; ► Zaman [23].

Due to computer resource limitations (see [341] for estimates), current jet LES studies use inlet conditions of an artificially thickened shear layer [331,332,98]. This can adversely impact the natural development of azimuthal variations in the jet and the radiated noise levels (see [351] for documentation of these issues). Once proper care is taken to allow the development of the azimuthal disturbances the obtained LES results compare favorably with the experimental data. As an illustration see the comparisons shown in Figs. 18 and 19 which show that jet mean flow and turbulence levels are being predicted well. More importantly, as shown in Fig. 20 the radiated noise levels and its directivity are also in reasonable agreement with data. Furthermore the spectral content of the radiated noise is also quite reasonable and LES with greater resolution captures the spectral shape better (recall the data shown in Fig. 8). Other groups [331,332,98,112][16] have reported qualitatively similar results. Since these calculations differ in the details of the numerical algorithms and subgrid models, taken together they support the notion that the spectral bandwidth of the radiated noise (and the near-field turbulence) depend primarily on the number of grid-points used, i.e. by the range of turbulent motions that the computational model captures. If dissipative or upwind-biased algorithms are used in jet LES, the range of scales that are accurately captured deteriorates dramatically. LES has been successful in capturing the trends observed in jet noise data as the jet operating parameters (jet Mach number, heating) are varied [119],

Fig. 20. OASPL directivity at a distance of $60r_o$ from the jet exit (unheated, $M_j = 0.9$) from Bodony and Lele [119]; — LES with 10^6 points; - - - - LES with 10^5 points; ○ Freund [36]; △ Stromberg et al. [344]; ▽ Mollo-Christensen et al. [417].

and a refined look at the changes in the flow responsible for the overall trends is underway. A major challenge for future studies is the incorporation of the nozzle in a high-fidelity simulation. A hybrid URANS-LES approach is a promising direction to achieve this. Sub-grid noise models [126,123] to address the impact of scales not captured in a LES approach is another important development for future. A more complete discussion of the far-field jet noise predictions using LES is provided by Bodony and Lele in [352].

5.2.4. Model problems related to jet noise
Sound radiation from a mixing layer: Sound radiation from unsteady vortex-dynamics in a planar shear-layer, such as vortex roll-up and pairing, has been studied using direct simulation of compressible flow [34,353].

---

[16]The study by Rembold and Kleiser [112] uses DNS and LES to compute a low Reynolds number $M_j = 0.5$ turbulent jet from a rectangular nozzle. Lighthill's acoustic analogy is used to predict the radiated noise and compared with DNS data.
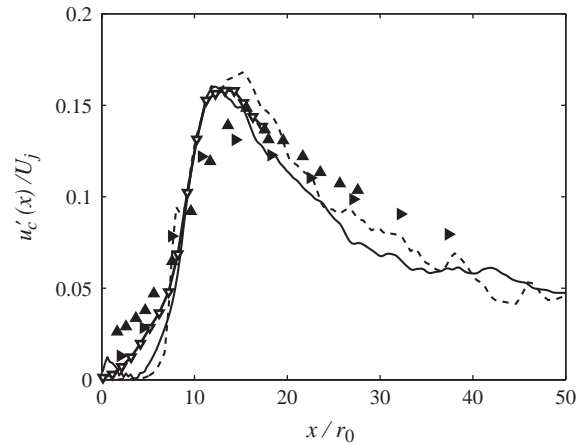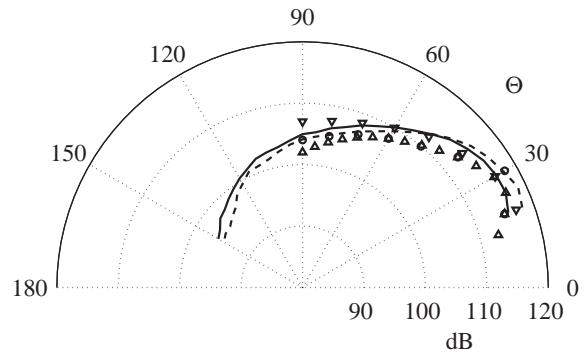
The simulation data was used to study acoustic source-term approximations, in the context of Lilley's equation [34], and for Lighthill's equation [353]. Colonius et al. [34] found that the particular approximation of the source terms due to Goldstein [50] gave good predictions for the noise radiation observed in the direct computation. They also found that the source-distributions responsible for the noise radiation from vortex-pairing could be fitted to a wave-packet shape and which explains its superdirective radiation [319]. Such radiation from wave packets in subsonic flows has also been studied by Avital et al. [134]. A recent study by Cheung et al. [326] studies the noise radiation from instability waves and vortex-pairing in subsonic and supersonic shear layers using nonlinear PSE and compares the predictions to DNS. They find that NPSE provides good unsteady flow predictions and the mean flow spreading plays a critical role in achieving this. For sound radiation NPSE provides good predictions for supersonic instability waves but not for the subsonic instability waves. For the latter Goldstein's form of the Lilley-equation source terms gave good noise predictions.

Sound radiation from vortex-pairing in a jet: Sound radiation from unsteady vortex-dynamics in the shear-layer of an axisymmetric jet was studied over a range of jet Mach numbers using direct computations [60]. For low Mach number jets the sound field due to the vortex-pairing resembled that of an localized quadrupole source, as also observed experimentally by Bridges and Hussain [354]. At higher Mach numbers the sound field became more strongly directed toward the jet-axis. Predictions of sound radiation were carried out using the Lighthill source terms. This required special care since the organized instability waves gave rise to spatially extensive sources. When the flow disturbances being convected out of the computational domain were accounted good agreement with the DNS sound-field was observed. Predictions were also made using a cylindrical Kirchhoff-surface around the jet. This

provided a fairly robust prediction and served as an internal consistency check on the calculations.

Sound radiation from supersonic instability waves: The sound radiation from supersonic instability waves in a jet has been studied by many authors [35,355,356]. Simulations of linear and nonlinear development of supersonic instability waves have been compared with the asymptotic theory of Tam and Burton [32] and experiments [357–359]. The agreement is quite good. Mohseni et al. [327] find that nonlinear interactions must be included for accurate amplitude predictions for all but the most unstable mode (peak frequency). This is also supported in recent work on supersonic instability waves in a shear layer [326].

Receptivity of a supersonic shear layer to incident sound: The problem of excitation of shear layer instability waves near a nozzle lip is of broad interest in predicting flow-acoustic resonance phenomena, such as jet screech and cavity resonance, and in active or passive management of flow for mixing and separation control. DNS of the receptivity of a shear layer to external forcing near the nozzle lip, and in particular to incident acoustic excitation has been studied by Barone and Lele [360,250]. They developed an overset-grid method using high-order interpolations [41] to embed a splitter plate with a rounded trailing-edge in the flow domain. The instability wave receptivity response was also predicted by solving the viscous adjoint equations and verified by solving the direct problem (see Fig. 21). The adjoint solutions provide an efficient way to characterize the shear-layer receptivity to many types of external forcing. Extension of this methodology to jet flow and other applications would be very useful.

Sound generation in jet screech: Shen and Tam [361] used a hybrid method to study jet-screech. They solve the jet mean flow using the unsteady RANS approach. The $k - \varepsilon$ equations, with coefficients for jet flows [362], were solved in the turbulent flow region and the (axisymmetric) Euler equations are solved in the exterior region. The nozzle geometry is retained with a multiple
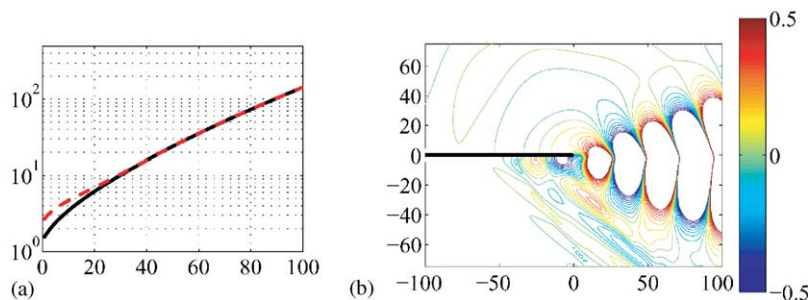

Fig. 21. (a) Instantaneous fluctuation pressure contours showing instability wave excitation for a streamwise momentum source placed in the lower stream boundary layer at $(x; y) = (37 : 5; 3 : 5)$. There are 16 equally spaced contours over the range 0:5 to 0:5. (b) Disturbance $|u|$ along $y = 3.$, solid line: computed solution, dashed line: prediction based on the adjoint solution. Both figures are from Barone and Lele [360].

block mesh with the highest resolution in the near-nozzle region. The calculations use the DRP scheme. The aim is to predict the amplitude and directivity of screech tones. This type of URANS approach can be justified when the spatial and temporal scales L_a, τ_a, of the dominant acoustic waves *and* their 'source processes' satisfy $L_a \gg L$, and $\tau_a \gg \tau$, where L and τ are representative spatial and temporal scales of the turbulence. The former condition is easily satisfied but the latter holds only marginally for the observed screech tones. URANS has also been used in other resonant acoustics phenomena such as supersonic cavity tones [363,364]. In recent work, Tam et al. [365]. have extended this approach to non-axisymmetric modes and shown that the mode-switching phenomena observed in screech from circular jets is reproduced. This raises expectations that a simple dynamical systems model could be developed to predict jet screech behavior (see also [366]).

A similar suggestion that the sound generation process in jet screech can be modeled with simpler models has emerged from DNS studies. Manning and Lele [42] studied an isolated screech-noise source region in a shear layer. Inflow boundary conditions are used to specify instability-wave eigenmodes that grow downstream and form large-scale vortices. Boundary conditions are used to independently specify a compression wave that is stationary in the supersonic stream. The interaction of the vortices with the compression-expansion wave generates sound. Upstream boundary conditions are designed to 'absorb' the upstream traveling sound and thus suppress the re-excitation of the shear-layer. Other critical boundary conditions are a 'quiet' treatment of the outflow zone so that large-scale vortices and sound travel out of the domain without a significant reflection. The numerical boundary conditions are quite challenging and require a careful validation [367]. The snapshots from DNS [42] illustrate the sound generation process. As the large-scale shear-layer vortices convect past the interaction location, the tip of the compression wave oscillates significantly. During the time when the so-called braid region passes over the compression wave tip, a part of this wave is observed to leak across the shear-layer toward the ambient region initiating a sharp cylindrical compression wave. Refraction of this wave back into the supersonic flow can also be observed. This is an upstream traveling Mach wave within the supersonic flow.

The DNS data [42] show that the radiated sound pressure level is proportional to the 'local' pressure rise in the shock-cell structure at the noise-source location. This is consistent with the experimental data on broadband shock-associated noise [335,336] which show a proportional scaling. This proportional scaling draws attention to a 'linear' mechanism of sound-generation. The linear scaling is further verified by a separate calculation using the linearized Euler equations (LEE)

about the non-linear unsteady flow of the shear layer. Primary features of the radiated signal observed in DNS agree very well with the LEE calculation. The radiated sound level is, however, *not* necessarily proportional to the amplitude of the unsteady disturbances in the shear layer. An amplitude threshold is observed below which the radiated sound is proportionally weak, but above it strong radiation occurs. As the shear-layer disturbances grow, they form distinct vortices (clumps of vorticity) and braid regions between them. Using Stuart's solution [368] (which contains an amplitude parameter A that controls vorticity clumping) of the (incompressible) Euler equation as a base flow, it was found that a vortex-laden mixing layer also shows the same thresholding behavior as the full DNS.

The model of geometrical acoustics to track ray trajectories and wavefronts through the unsteady base flows of the vortex-laden mixing layer offers an explanation [42] of the DNS results. The initial ray direction corresponds to the stationary Mach waves in the supersonic stream. For small A all rays are reflected back toward the supersonic flow, but as A increases a small window of rays penetrate across the mixing layer; the onset of transmission occurring around $A \approx 0.54$. The size of the ray bundle that is transmitted above this threshold grows initially but saturates at high A; this limits the maximum transmission across the mixing layer as observed in full DNS. In more recent studies Suzuki and Lele [369] have provided a mathematical justification of the ray-acoustics limit for the jet-screech problem. They show that the problem of propagation of a weak shock, with a steep gradient, in a vortex-laden mixing layer is analogous to the ray-tracing approach of high-frequency geometrical acoustics. An example of the computed ray paths in a spatially-developing mixing layer are shown in Fig. 22. Evidently, all rays are reflected back in the early part of the shear layer but some rays penetrate across to the subsonic side once the shear layer has rolled up into clumped vortices. Taking this approach to the next order, they also show that the amplitude of the radiated sound can be satisfactorily predicted. An example of this is shown in Fig. 23. The prediction of the radiated shock front agrees closely with the DNS observation. Recent measurements [370] in a screeching jet have provided an unprecedented detail of the unsteady jet flow during the screech cycle. These data support the notion that vorticity clumping in the jet shear layer plays a major role in determining the screech amplitude.

Broadband shock-cell noise generation: Recent numerical simulations have also given new insights into the broadband shock-cell noise generation. Consider the schematic of an underexpanded jet in Fig. 24. The shock-cell structure in early parts of a jet comprises of relatively steep compression waves or shocks. The turbulent eddies in the early jet have a short life time,

thus each interaction with the shock-cell structure behaves as an isolated source region. Lui and Lele [340] have conducted DNS studies of noise generation from such an 'isolated noise source'. Fig. 25 shows a visualization of the noise radiation from the interaction of a turbulent shear layer with an isolated shock cell. The cylindrical waves originating from the interaction region are attributed to this interaction. This radiation is approximately omni-directional with an apparent origin somewhat downstream of the interaction site. A detailed study of the noise-generation [40] shows that the observed sound is generated closer to the supersonic edge of the shear-layer and travels downstream before radiating into the ambient. This explains the down-stream shift in the apparent source. The magnitude of the radiated pressure was found to scale with the imposed pressure change in the incident compression wave, a scaling observed in experiments. Interestingly, the spectral peak of the radiated noise corresponds closely with the spectral peak of the turbulence in the

shear-layer at the interaction location. This can be observed in Figs. 26(a) and (b), which show the frequency spectrum of TKE near the interaction
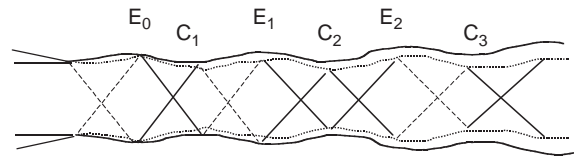
Fig. 24. A schematic representation of the shock cell structure in a moderately under-expanded jet. Solid lines drawn within the jet represent compression waves, similar dashed lines are expansion waves. Shock-cell shear-layer interaction locations are labeled.

Fig. 25. Visualization from DNS of the interaction of a compression wave with a turbulent shear layer. Contours of vorticity magnitude show the shear layer and the compression wave and its reflection are observed in the pressure contours (triangle shape). Contours of dilatation in gray-scale show the sound field. The noise generated by the interaction of turbulence with the compression wave appears as weak cylindrical waves. $M_1 = 1.2$, $M_2 = 0.0$, $\Delta p/p_1 = 0.2$ reproduced from Lui and Lele [340].
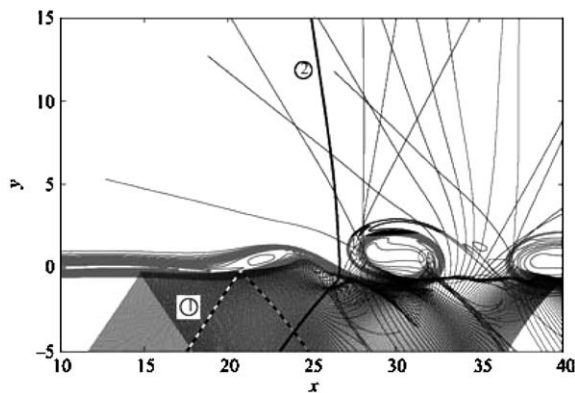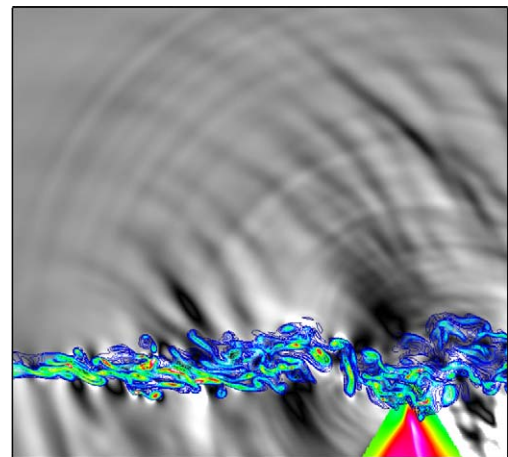

Fig. 22. Ray trajectories in a vortex laden supersonic shear-layer, reproduced from Suzuki and Lele [369]. The initial direction of the rays corresponds to the Mach wave direction. They are totally internally reflected from regions where the shear layer vorticity is strong and leak into the subsonic flow region in between the clumped vortices.
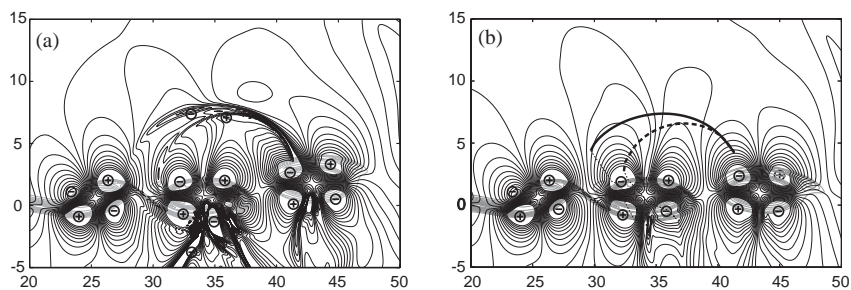

Fig. 23. A snapshot of results from screech model problem. (a) DNS result; (b) Geometrical acoustics result. Solid lines show contours of dilatation whose sign is marked. Also overlaid are contours of vorticity at the same instant. From Suzuki and Lele [369].

location and the (noise) pressure spectrum at an upstream observer point, respectively. This coincidence is significant since the elevated spectral level of shock-cell noise typically extends to frequencies much higher than the mixing-noise peak at $\chi = 90°$. First few shock-cell shear-layer interactions, see Fig. 24, can potentially generate noise at these high frequencies. A theoretical model that captures many features of the DNS results has also been developed recently [371]. This model provides analytical predictions for the noise radiation from the interaction of shear-layer disturbances with an isolated shock cell. Its formulation draws from previous theoretical work by Kerschen and Cain [372] and Tam [307]. The noise source terms associated with the shock shear-layer interaction are reformulated using generalized functions in the context of Lighthill's equation, and the result is simplified by appeal to observations from DNS. The radiated noise depends on the local shock and turbulence properties; the model shows the streamwise (turbulent) velocity fluctuation, $\frac{u_1'}{U_j}$, and the local (shockcell) pressure amplitude Δp to be controlling variables. Such a model can provide useful extensions of the existing shock-cell noise prediction methods, and efforts along these lines are underway.

Lui and Lele's DNS provides data on space–time correlations relevant to shock-cell noise prediction. Such data have guided the development of a statistical shock-cell noise model. It is common in shock-cell noise literature to associate the radiated noise amplitude with the shock-cell pressure amplitude Δp. The new model [371] provides a mathematical basis/explanation of this scaling. It also explains why shock-cell noise is independent of the jet velocity (for a given pressure ratio). This remarkable property of heated jets has a simple explanation [371]. The shock-cell noise sources, for example the unsteady stress-fields due to the interaction, are proportional to the local (mean) jet density and are bilinear in the turbulence velocity $u_i^{(t)}$ and shock-cell-associated velocity disturbance $u_i^{(s)}$. For small amplitude disturbances the latter (Mach waves) is proportional to Δp but is also inversely proportional to the local (mean) jet density. If the local turbulence intensity $u_i^{(t)}/U_j$ is insensitive to the jet temperature, the radiated shock-cell noise is proportional to Δp and independent of U_j and T_j, etc. This simple scaling property is shared by a more complete shock-cell noise model that accounts for the spatially extensive noise-sources. This simple scaling can be contrasted with the empirically determined amplitude factor in Tam's formula [338] which shows good agreement with data but with no explanation offered for the specific empirical function used.

Sound radiation by a turbulent vortex ring: Sound generated by turbulent vortex rings (as distinguished from sound generated by interactions of laminar vortex rings discussed in Section 5.1), has been experimentally measured and theoretically modeled in a series of papers by Kopiev and co-workers (e.g. [373,374] and references therein). Transition and turbulent decay of an initially laminar vortex ring together with its radiated acoustic field was recently computed by Ran & Colonius [37]. In the computations, the vortex ring was created by a body force with specified spatial and temporal distribution in order to mimic the cylinder/piston mechanism for generating vortex rings in the laboratory. The formed rings have a Reynolds number based on circulation of 4500, and an approximately Gaussian distribution of vorticity in the core, with a core to ring radius ratio of 0.34. The corresponding piston stroke length to cylinder diameter ratio for the laboratory generation is 1.5. A stochastic perturbation is added to the body force in order to produce rings with random distortion of the ring radius in the azimuthal direction. This produces an initially divergence free perturbation field. A series of 15
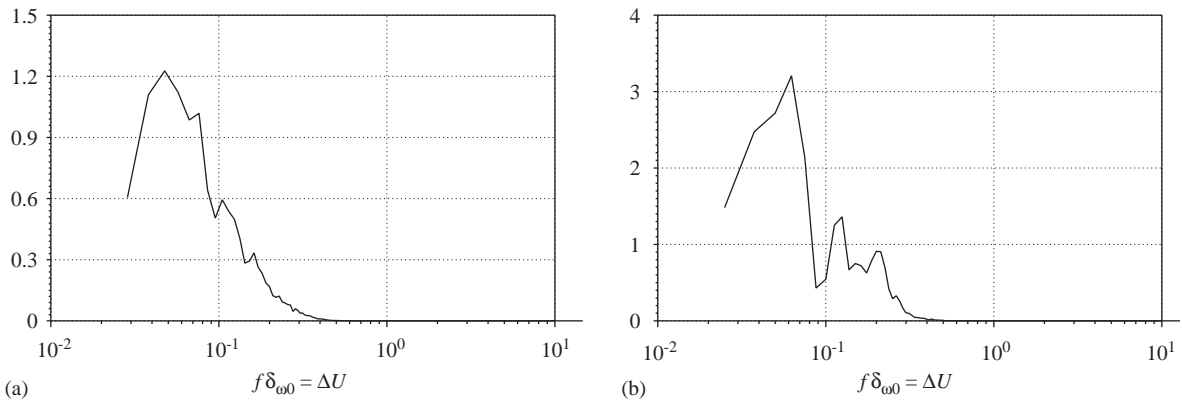

Fig. 26. (a) Frequency spectrum of u_1' near the interaction location; (b) Spectrum of the radiated noise (pressure) measured at approximately 45° from the upstream direction. Both spectra are pre-multiplied by the frequency, f. Reproduced from Lui and Lele [40].

calculations were performed in order to gather ensemble-averaged statistics for transition and turbulent phases. The far-field radiation was computed directly from the compressible Navier–Stokes computations by using a Kirchhoff surface placed on a large sphere with radius ten times the ring radius. The far-field radiation is also estimated using low Mach number vortex sound theory by computing relevent moments of vorticity from the DNS data.

After an initial transient associated with the forcing, instabilities with specific azimuthal mode numbers (primarily $n = 6$ and 7) and a particular radial structure grow most rapidly, in accord with linear stability theory [375]. During later stages, nonlinear interactions bring about significant growth of the lower azimuthal modes ($n = 0$, 1, and 2) and lead to the strongest acoustic radiation. Eventually the vortex ring breaks down and the turbulence decays. During decay, a good collapse of the azimuthally and ensemble-averaged velocity fields with the self-similar theory [376] is observed. Fig. 27 shows the evolution of the near-field vorticity together with results for the acoustic field. The growth, satura-

tion, and decay of the acoustic field correspond to the linear instability, nonlinear interaction and breakdown, and turbulent decay phases, respectively.

The directivity for azimuthal modes with $n = 0$, 1 and 2 agreed well with predictions of vortex sound theory provided that Doppler corrections are made to account for the finite Mach number of ring translation (two different average translation Mach numbers were considered–0.14 and 0.28). Based on the theory for self-similar decay of the turbulent near-field, vortex sound theory was used to predict the decay rate for the acoustic field. Simulation results at the two different Mach numbers confirm the scaling. The (temporal) spectra at all angles were peaked at a frequency $\omega = \Omega_0/2$, where Ω_0 is the equivalent vorticity of a ring with constant vorticity across the core. This is in agreement with experiments [377], and is also predicted theoretically by examining linear eigen-oscillations of a thin-cored vortex ring [373].

Ran and Colonius also used the ensemble of vortex ring calculations to examine a heuristic model of a jet composed of a train of un-correlated vortex rings with a
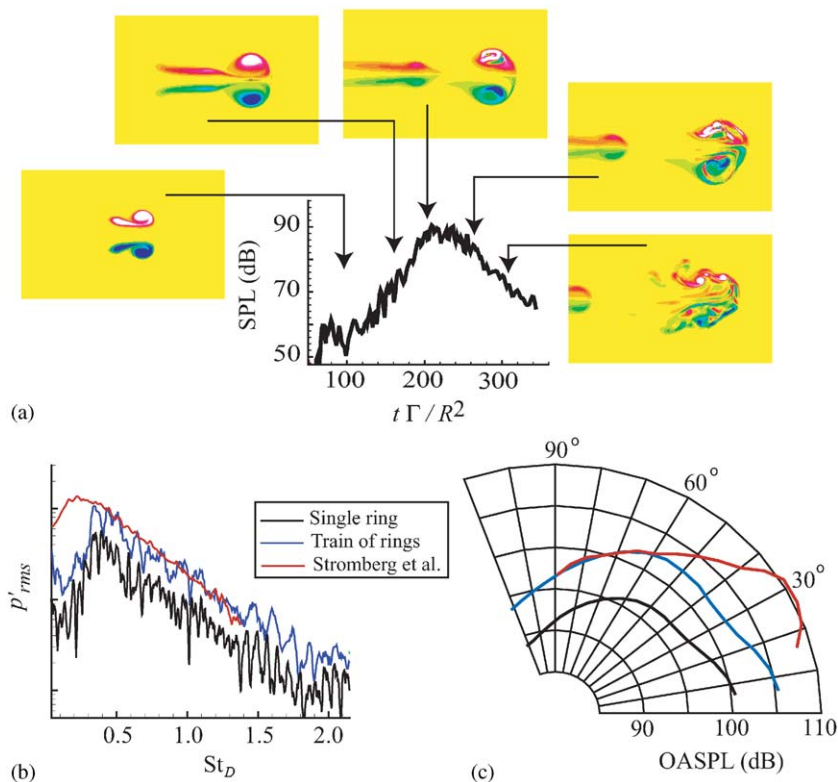

Fig. 27. Sound generated by a turbulent vortex ring (from [37]). (a) Temporal evolution of ensemble-averaged acoustic field and selected snapshots (single realization) of vorticity contours in a slice through the ring. (b) Frequency spectra and (c) directivity of acoustic field. All acoustic results are at 30 degrees to the axis of translation and 15 radii from the (nominal) center of the ring. For the train of vortex rings (see text), the replication frequency corresponds to a jet Strouhal number of 0.2. The experimental data [344] corresponds to a $M = 0.9$ jet with $Re = 3600$, and OSPL is shifted to agree at $60°$.

fixed replication frequencies. To compare frequencies between the ring and jet, they assume that the ring translates with a convection speed corresponding to $0.5U_j$ to $0.6U_j$. Results are displayed in Fig. 27 and compared with low Reynolds number jet noise measurements [344]. The noise spectrum was nearly invariant to replication frequencies around the range corresponding to jet Strouhal numbers $St = 0.2$ to 0.3, which corresponds to the frequency of peak amplification of linear instability waves in the jet mean flow field. The primary effect of replication was to enhance SPL by about 5 dB. The peak frequency of the single vortex ring was preserved in the train of rings. It corresponded to about $St = 0.4$, which is somewhat higher than the peak frequency of jet noise, especially at low Mach and Reynolds numbers. Nevertheless, the spectral shape at frequencies above $St = 0.4$ and the directivity at angles greater than about $60°$ are quite similar to the low Reynolds number experiments. The overall sound pressure level (of the replicated ring) was within about 4 dB of a higher-Reynolds number jet [26] with a similar Mach number as the computations.

5.3. Model problems of cavity noise

A number of groups have recently used CAA codes to investigate the resonant flow/acoustic instabilities in flows over open cavities. A renewed interest in this problem stems from recent experimental efforts to suppress cavity tones and broad band noise through actuation near the leading cavity edge. Unsuppressed, intense noise levels in open cavities on aircraft can reach levels exceeding 160 dB. These high noise levels can damage stores, fatigue nearby surfaces and components, and adversely affect store separation and accurate delivery of weapons [378,379]. It has long been known that passive devices, such as spoilers and fences near the separation point, and trailing edge ramps can significantly reduce tone amplitudes [380]. More recently, attention has shifted to both open and closed-loop control with active devices such as unsteady mass injection, synthetic jets, powered resonance tubes, etc. Further details regarding these experiments may be found in a recent review [381]. In addition to adapting to changing flow conditions, feedback control has the potential to reduce required actuator power once control is achieved. However, effective feedback control of flows is made difficult by, on one hand the flow's sensitivity to external disturbances, and on the other hand by the difficulty of establishing accurate system models that fit into the framework of modern control theory. Generally speaking, the better the understanding of the flow physics, the more likely it is that robust and efficient control strategies may be developed.

Computational efforts can play a key role in developing an understanding of the flow physics and providing data for reduced-order models. Early work by Powell [382] and Krishnamurty [383] identified essential features of the cavity resonant feedback loop: (i) excitation of an unstable shear layer spanning the cavity, (ii) generation of an unsteady irrotational field by interaction of the shear layer with the downstream edge, and (iii) the upstream influence of the irrotational field which provides for the further excitation of the instabilities in the shear layer, especially near the upstream edge. For incompressible flow, the upstream influence is instantaneous, while for compressible flow there is an acoustic delay. Obviously the feedback loop has much in common with other flow/acoustic instabilities such as jet screech (see Section 5.2.2 above), and edge-tones.

The earliest complete description of the resonant process is due to Rossiter [384], who developed a semi-empirical formula to predict when the phase change of a disturbance, at a given frequency, leads to constructive reinforcement and, ultimately, saturation:

$$St_n = \frac{f_n L}{U} = \frac{n - \alpha}{M + \frac{1}{\kappa}}, \quad n = 1, 2, 3, \ldots, \tag{49}$$

where St_n is the Strouhal number corresponding to the nth mode frequency, f_n, κ is the average phase speed of the vortical disturbances, and α is an empirical constant, typically taken around 0.25. Various refinements of this formula have been suggested (e.g. [380]), for example to account for the higher sound speed inside the cavity at higher Mach numbers. Spectra from a large number of experiments over the years show reasonable agreement with Eq. (49), but with a significant amount of scatter particularly at low Mach numbers. The data for the saturation amplitudes exhibit a far greater scatter than the frequencies. It should be noted that a dimensional analysis would show that cavity resonant frequencies and amplitudes could depend on the flow speed, U, the boundary layer (momentum) thickness, θ just upstream of the cavity, and ambient density, ρ_∞, viscosity, μ_∞, and sound speed, a_∞. For the three dimensional rectangular cavity with length, L, depth, D, and breadth, H, there are thus 5 dimensionless parameters governing the flow $L/D, L/H, L/\theta, Re_\theta = \frac{\rho_\infty U \theta}{\mu_\infty}, M = \frac{U}{a_\infty}$ as well as additional parameters and profiles that would specify the state of the boundary layer upstream of the cavity if it is turbulent. Given this, it is not surprising that there is significant scatter. A primary source of scatter at low Mach number is due to an interaction with normal acoustic resonant modes of the rectangular cavity [380,385–387], and at all Mach numbers dependence on L/D that does not appear in Rossiter's formula. Some of the sensitivity of the amplitudes can be understood by using linear parallel stability theory to predict the growth rate of unstable disturbances in the shear layer [38].

5.3.1. Computational efforts

Computation of cavity resonance is, on one hand, facilitated by the high amplitude of the acoustic fluctuations that are driven (and drive) the instability (by comparison jet noise is much less efficient). On the other hand, because hydrodynamic disturbances are driven by the acoustic fluctuations, it is not possible (except perhaps at low Mach number) to consider acoustic radiation as a weak byproduct of the turbulent flow, and therefore hybrid techniques such as acoustic analogy or flow/acoustic decoupling (see Section 3) are inappropriate. This dictates a direct approach wherein the compressible Navier–Stokes are computed over the near-field (and to sufficient distance from the cavity in all directions such that the oscillations do not depend on the domain size).

Resonant oscillations in cavity flows were first computed with two-dimensional, unsteady simulations employing RANS models [388]. RANS has remained widely used for subsonic [389–392], transonic and supersonic [388,363,393,394,364,391,395,396], and hypersonic [397] regimes. Most of the calculations have concentrated on rectangular cavities, with L/D ranging from about 2 to 10. The earlier works utilized zero equation turbulence models, and later works generally used two-equation models in the $k - \varepsilon$ or $k - \omega$ framework. Experimental validation of these simulations include good agreement with frequencies of oscillation from experiments (and as predicted by Rossiter's formula), and in some cases reasonable agreement for mean velocity profiles, RMS pressure fluctuations along the cavity walls, and the peak amplitudes in pressure spectra.

LES computations: Given the dominance of large scale vortices in the instability process, cavity flow would at seem a good candidate for Large Eddy Simulation. Complicating this, however, is the recognition that proper resolution of the large scale turbulence in the incoming boundary layer flow will require large grids, for even moderate Reynolds number cavities. One alternative, which has been used in practice, is to use RANS in the boundary layer upstream of the cavity, switching to LES over the cavity [398]. Shieh and Morris [390,399] have computed subsonic cavities with such a hybrid RANS/LES methodology and the Spalart/ Allmaras turbulence model. They considered a cavity with $L/D = 4.4$, $L/H = 4.4$, $M = 0.6$ and $Re_D = 40,000$. They concentrated on investigating issues related to wake mode (see discussion below), and did not compare with experimental measurements. The boundary layer had a thickness $\delta_{99}/D = 0.2$. Supersonic results have been published [395] for three-dimensional LES (Smagorinsky) of a rectangular cavity with $L/D = 4.5$, $L/H = 4.5$, $M = 2$, and $Re_L = 4.5 \times 10^6$, and for the same cavity with $M = 1.5$ by the Lockheed group [400]. In both cases the run conditions correspond to the high-speed data of Shaw [401]. The Lockheed study also compared results with an Euler method (which relies on numerical viscosity as a crude turbulence model). Peak amplitudes in the pressure spectra showed reasonable agreement with the experiments, but were sensitive to numerical diffusion and modeling assumptions and grid densities [400]. Sinha et al. [395] report vorticity iso-surfaces and Reynolds stresses at the cavity mid-length and mid-span that show little three-dimensionality, but it is not clear whether three-dimensionality would evolve correctly in the absence of forcing from the upstream boundary layer. LES simulations of supersonic cavities have been performed by Rizzetta and Visbal [402]. They used compact fourth-order FD schemes in conjunction with sixth-order non-dispersive filters. An iterative semi-implicit second-order time advancements is used. The computations were performed with over 20 million grid points on 254 processors and utilized the dynamic Smagorinsky model for the subgrid stresses. The Reynolds number based on cavity length was 20,000. The displacement thickness of the incoming boundary layer was large, about 1/6 of the cavity depth. The turbulent boundary layer ahead of the cavity was also resolved directly, and separate simulations of boundary layer turbulence were needed to provide for inflow data to the cavity simulations. Unsteady, high-frequency mass injection was also simulated by applying a given jet velocity profile across a small (spanwise uniform) slot upstream of the cavity. Comparisons with experiment (at a Reynolds number some 10 times higher) consisted of spectra of pressure fluctuations at various positions along the cavity bottom, and showed reasonable agreement in both magnitude and trends.

These LES studies show great promise but were hampered, to some extent, by a lack of contact between experiment and computation, especially with regard to detailed turbulence statistics. In recent work, Larchevê-que et al. [403] have performed LES for $M = 0.8$ flow over a deep cavity with $L/D = 0.42$, matching the experimental conditions of Forestier et al. [404]. The final computations relied the *selective mixed-scale* LES model [405] with a second-order centered scheme. The simpler MiLES approach [406] was used for a series of computations that were used to assess the impact of spanwise extent of the domain and the resolution, and for a comparison with the LES computations. The MiLES approach solves the Navier–Stokes equations with dissipative numerics (upwinding) to provide some model for the dissipative behavior of unresolved turbulent stresses.

The ONERA LES computations (including MiLES) showed impressive agreement with the experiments for a number of important quantities: mean velocity, turbulent kinetic energy, Reynolds stress, momentum thickness, phase-averaged velocities, and pressure spectra. The dynamics of the coherent structures were also

similar—the dominant oscillation mode showed 3 vortices, one of which is subsumed within the cavity, one of which interacts with the first before impinging on the trailing edge and being ejected, and a third which is flung over the cavity. These dynamics are not necessarily consistent with the standard view of Rossiter modes, but the spectral peaks can be fit reasonably well to mode $n = 1$ of Eq. (49) provided a low value is chosen for the empirical constant α. A second peak in the spectrum was attributed to a longitudinal acoustic mode in the cavity. Interestingly, the LES computations were performed both with and without an upper wall located at a height of 2 cavity lengths (which mimics the wind tunnel of the experiment). The confinement led to additional reinforcement of harmonics in the spectra, and without the upper wall, the third vortex in the pattern disappeared. It was hypothesized that the increased amplitude of pressure fluctuations in the confined case led to a baroclinic torque acting on the density profile in the separating boundary layer to produce the third vortex. Finally, the wake-mode mechanism discussed below was not believed to be the cause of the observed dynamics.

The ONERA computations show clearly how accurate LES computations can be used to explore the dynamics of complex unsteady, separated flows. While the interpretation of the modes of oscillation is perhaps open to debate, further computations should be able to offer more definitive answers. In particular, it is suggested that the Mach number and cavity dimensions be varied. Since all three modes considered (Rossiter, longitudinal acoustic mode, and wake mode) have *different* scaling with Mach number, and the acoustic modes are strong functions of L/D, it should thus be possible to sort out which mode is dominant.

DNS computations: DNS has of the cavity flow has been limited to (transitional) two-dimensional flows [407,408,390,38,61], and has featured the high-order-accurate FD schemes discussed in Section 4.1, including the compact scheme, C6 [407] and the DRP scheme [408,61]. In the Caltech work, two-dimensional DNS calculations were performed over a wide range of parameters $1 < L/D < 8$, $30 < Re_\theta < 80$, $20 < L/\theta < 120$ and $0.2 < M < 0.8$. Grid convergence and boundary placement experiments confirmed that the computed solutions were independent of numerical artifacts. Further details of the code and its validation is given in the references. Experimental verification of the results is somewhat limited due to two dimensionality and low Reynolds number considered. The early laminar boundary layer experiments of shallow but broad cavities by Kirshnamurty are closest to the DNS data, and a qualitative comparison of Schlieren images for the cavity and its radiated acoustic field (Fig. 28) shows encouraging agreement that includes the change in structure of the acoustic field as the Mach number is varied. Gloerfelt et al. [61] showed that the directly computed
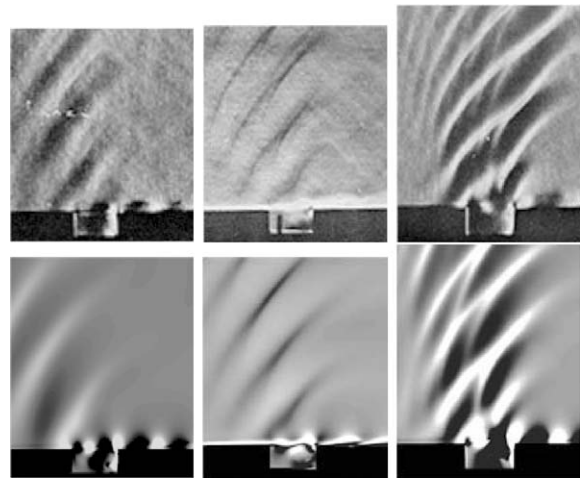

Fig. 28. Comparison of Schlieren photographs [383] with contours of density gradient from the DNS [38]. Top row are the experimental results at $M = 0.64$, 0.7, and 0.8 (left to right) and the bottom row are density gradient contours from DNS at similar Mach numbers. Note that middle column have the knife-edge horizontal while the top and bottom have knife-edge vertical.

acoustic field was in good agreement with either a Kirchhoff- or Ffowcs-Williams–Hawkings-surface placed one cavity-depth above the cavity lip.

Oscillation regimes: Gharib and Roshko [409] observed that as the length of the cavity[17] was increased, there was a substantial change in the behavior of the cavity oscillations. They dubbed the newly observed phenomena as "wake-mode" oscillations. The flow became dominated by shedding of a large-scale (order of the cavity depth) vortex from the cavity leading edge, and involved intermittent impingement of a the free-stream flow inside the cavity. This led to a much larger cavity drag than shear-layer mode oscillations described by the Rossiter feedback cycle. A similar instability was present in numerical simulations of instabilities in dump combustor [410]. In two-dimensional DNS, Colonius et al. [407,38] have observed a similar transition. In both experiment and computation, the boundary layer upstream of the cavity was laminar. The wake mode transition has also been observed in two-dimensional RANS calculations at higher Reynolds numbers [389,390,392].

Rowley et al. [38] have performed an extensive mapping of the transition to wake mode in parameter space. A key point is that the frequency of oscillation in wake mode is to be nearly constant with Mach number (from 0.4 to 0.8) and it would appear that the instability is in this regime is purely hydrodynamic in nature. Based

---

[17]It should be noted that Gharib and Roshko utilized an axisymmetric cavity in a water tunnel.

on similarities of the mean flow profiles with those of wakes and shear layers between streams of opposing direction, it was speculated that the transition may be the result of an absolute instability. A consistent prediction for the transitions from steady flow to shear layer mode and shear layer mode to wake mode was derived based on linear quasi-parallel stability analysis of the shear layer, coupled to simple models for acoustic scattering, propagation and receptivity problems [38]. The so-called 'loop-gain' (the total amplification of an unsaturated disturbance once around the feedback loop) was used as a measure of the saturation amplitude.

In addition to the presence of wake mode in the aforementioned incompressible experiments [409], a similar phenomenon has been noted in experiments on the side-branch of a pipe at high Reynolds number (which can be considered an infinitely deep cavity). However, for cavity flows at similar values M and L/D as in the 2D computations, but at higher Reynolds number and with turbulent upstream boundary layers, wake mode has not been observed in experiments. The LES computations of Shieh and Morris [399] showed that at otherwise identical parameters, two-dimensional computations exhibited transition to wake mode while three-dimensional computations did not. This has led to the hypothesis that wake mode is an artifact of two-dimensionality [399,61]. What is clear is that two dimensionality plays a role in the transition from shear layer to wake mode, but one cannot conclude that two-dimensionality *precludes* wake mode over the entire parameter regime (after all it is observed in experiments!). The hypothesis that the transition to wake mode occurs when shear layer instabilities suffer high amplification rates [38] is consistent with the observation that cavity oscillations are *stronger* for laminar flow than turbulent flow [383]. Apparently the additional turbulent spreading of the shear layer leads to overall lower levels of amplification. This may be what delays or prevents transition to wake mode at higher Reynolds numbers. Similarly, the turbulent flow within the cavity is likely to be much less organized in three-dimensional flow. The correspondingly smaller recirculation, especially near the upstream edge, may also deter the transition. Further three-dimensional computations (together with experiments) may be needed to fully resolve the parameter space where wake mode can be expected.

5.3.2. Summary

Some issues regarding the resonant oscillations in cavity flows that have received little attention are nonlinear interactions of modes (for which there is experimental evidence), and their three-dimensionality. Numerical simulations are likely to play a key role in such investigations. Recent simulation efforts have been guided by advances in computational methods that are the subject of this review. DNS at low Reynolds number offers an important glimpse into the details of nonlinear cavity dynamics; LES at moderate Reynolds numbers shows promise in bringing accurate computation to realistic conditions; validating the LES in detail requires experimental data at closely matched conditions, especially turbulence statistics.

6. Closure

Lighthill [411] envisioned that CAA would lead to a 'second golden age of aeroacoustics' and the level of active current research attests to his view. The next few years promise to bring about a wealth of new information about sound-generation physics and its modeling. It should be stressed that the new advances in aeroacoustics are expected from new ways of analyzing, processing, probing and modeling the flow and its noise. The steps of modeling the acoustic sources and their attendant radiation field require approximations that have been at the heart of the science of aeroacoustics for fifty years. Computation will not for replace such modeling in the foreseeable future. While it is tempting to compute ever more realistic flow configurations with LES and hybrid RANS/LES methods, there is still much to be gained by examining the physics of sound generation in relatively simple turbulent flows, and using computations to inspire models and to provide data to calibrate models and validate approximations.

And while much has been learned about how to accurately compute a flow and its radiated acoustic field, either directly or through acoustic analogy, there remain substantial computational challenges. Sub-grid modeling for LES (both for the sub-grid stresses and the sub-grid noise sources), accurate and robust boundary conditions, and high-order-accurate methods in complex geometries are pacing items in CAA. As we have stressed in this review, existing techniques require some "care and feeding" in their use. Artifacts (spurious waves) can lead to instabilities and poor quality solutions without sufficient resolution and careful use of artificial viscosity. Overly dissipative numerics can be equally disastrous. New problems and new methods should be carefully validated against previous solutions and experimental data, when available, and, in any case, be subjected to grid resolution and artificial boundary placement studies.

We close by citing some recent studies that have used CAA techniques for aeroacoustic optimization, and active flow and noise control. We expect studies of this type, and novel application of CAA in general, to grow. For example, Barone and Lele [360] solved the viscous, linearized, adjoint equations to determine the sensitivity of convectively unstable instability waves in a supersonic shear layer to different types of forcing near the splitter-plate tip. In Fig. 29 the effectiveness of forcing due to an
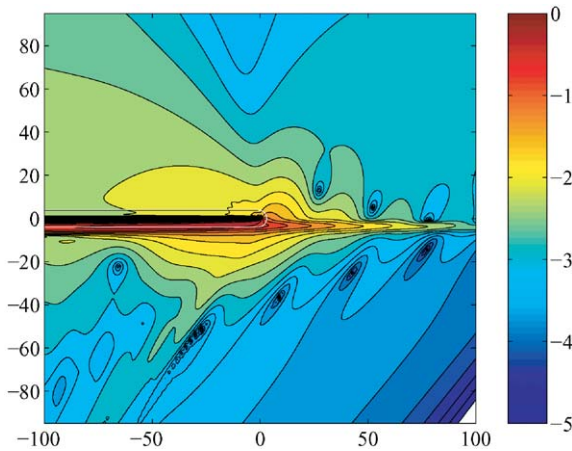
Fig. 29. Modulus of the adjoint streamwise velocity for a supersonic mixing layer with a forcing frequency $\omega\theta/C_1 = 0.08$, where θ the momentum thickness of the high-speed boundary layer near the trailing edge. The modulus is plotted on a base-10 logarithmic scale. High values indicate regions where a streamwise body force is more effective in exciting shear-layer instability waves at this frequency. From Barone and Lele [360].

applied streamwise body force is plotted on a logarithmic scale. Evidently, the shear layer is highly sensitive to forcing in the near splitter tip region and within the upstream supersonic boundary layer. The figure also reveals other modes of receptivity that result from the interference between different physical responses. This type of global mapping of flow- and noise-sensitivity can potentially be very useful in the search for effective flow control methods. Wei and Freund [412,413] have applied the control-theory for PDE to the problem of minimizing the noise radiated by an unsteady two-dimensional shear-layer toward the low-speed stream. Control is manifested in external forcing to the governing equations in a region near the origin of the flow and the objective function is the integral of pressure variance on a surface in the low-speed free-stream. As shown in Fig. 30, a dramatic reduction of the radiated noise can be achieved even though the flow is only mildly perturbed! While this study considers a highly idealized problem, the mechanism by which noise-control is achieved in a targeted region can have widespread use. Another example of aeroacoustic optimization is shown by Marsden et al. [414] who apply modern optimization tools designed for use with very costly function evaluations. They show via un-
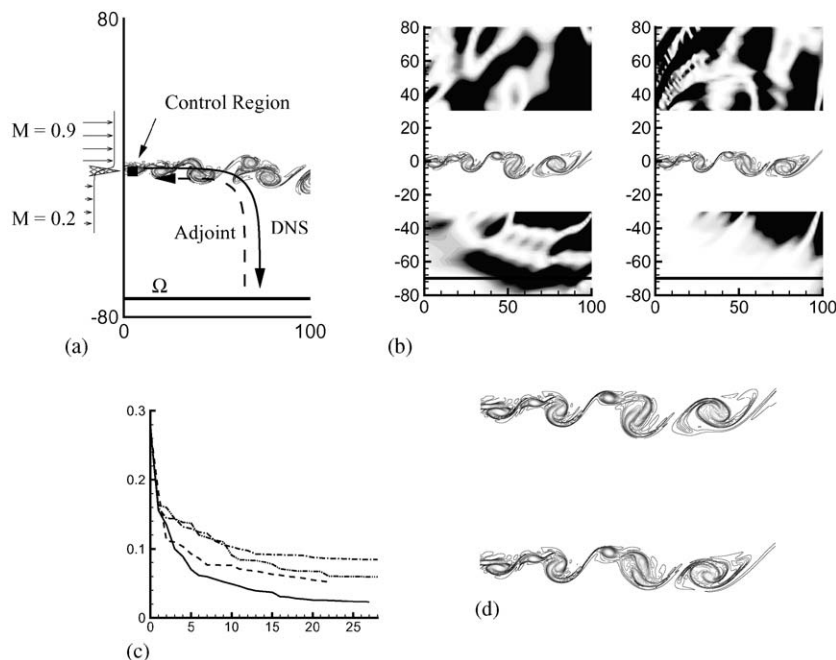

Fig. 30. The noise from a mixing layer is reduced by adjoint-based optimization by Wei and Freund [412,413]. (a) The flow and sound are solved by direct numerical simulation. The DNS solution allows the corresponding adjoint of the linearized perturbed equations to be solved. This gives the sensitivity of the far-field (Ω) noise to the control. (b) The flow and sound field before (left) and after (right) control. (c) The reduction of the cost function $\mathscr{I}(\phi) = \int_{t_0}^{t_1} \int_\Omega (p - p_0)^2 \, d\Omega \, dt$ by different controls: — internal energy control; - - - - streamwise direction bodyforce; ·-·-· cross-stream direction bodyforce; ······ mass source. (d) The flow structure (indicated by vorticity contour) before (above) and after (below) control qualitatively the same despite the huge reduction in the noise.
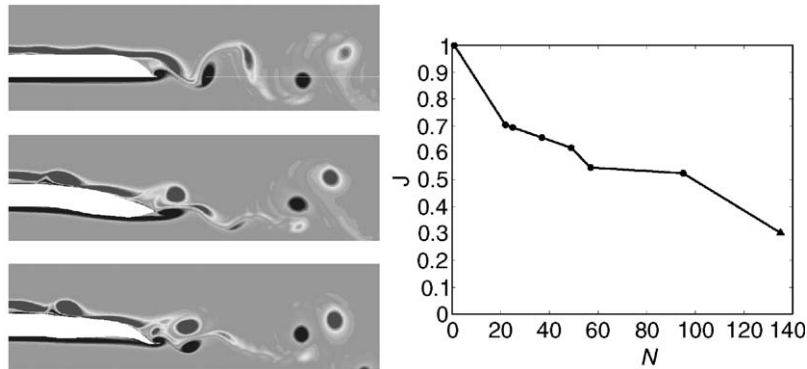
Fig. 31. Suppression of trailing-edge vortex shedding noise using derivative-free shape optimization by Marsden et al. [414]. Left: comparison of instantaneous vorticity contours (−25, maximum 25, 20 contour levels). Original shape (upper), optimal shape achieving 48% cost function reduction with lift and drag constraints satisfied (middle) and optimal shape achieving 70% cost function reduction, 1.5% drag increase (lower). Right: normalized cost function reduction vs. number of function evaluations. Circles are values which exactly satisfy lift and drag constraints. Triangle shows greater cost function reduction with slight relaxation of drag constraint.

steady calculations of a trailing-edge flow (Fig. 31) that the aerodynamic performance can be maintained or even improved along with aeroacoustic optimization. Use of CAA methods for simultaneous aerodynamic and aeroacoustic design is projected to grow in the future.[18]

Although this review has focused on the advances from a computational perspective, the contributions from advanced experimental diagnostics such as quantitative whole field imaging, microphone array processing and acoustic holography etc. are equally impressive. As the capability of the new tools advances, progress will hinge critically on the engineer/scientist's ability to distill the vital information from the massive volumes of data. Theoretical efforts, and models will continue to play a central role in advancing the science of aeroacoustics.

Acknowledgements

[18]A related problem of aerodynamic design for sonic-boom minimization has received considerable recent attention, see for example [415]. Steady flow CFD techniques are being applied to realistic airframe configurations and the near-field computed using a nonlinear solver. Its extrapolation to obtain the ground boom signature exploits far-field propagation techniques developed for sonic-booms. This is an example of a hybrid-technique. Other noise generation problems require unsteady flow calculations and thus the cost of the direct and/or adjoint solutions increases by more than an order of magnitude. However the projected increase in the computational capabilities over the next 10 years should allow a scientific study of aeroacoustic optimization problems.

References

[1] Crighton DG. Basic principles of aerodynamic noise generation. Progr Aerospace Sci 1975;16(1):31–96.

[2] Smith MJT. Aircraft noise. Cambridge: Cambridge University Press; 1989.

[3] Goldstein M. Aeroacoustics. New York: McGraw-Hill; 1976.

[4] Blake WK. Mechanics of flow-induced sound and vibration, vols. I and II. New York: Academic Press; 1986.

[5] Wang M, Moin P. Computation of trailing-edge flow and noise using large-eddy simulation. AIAA J 2000;38: 2201–9.

[6] Költzsch P, Kalitzin N, editors. Proceedings of the Aeroacoustics Workshop SWING, Technische Universitat Dresden, October 1999.

[7] Körner H, Delfs J, editors. Proceedings of the Aeroacoustics Workshop SWING II, Technische Universitat Dresden, November 2000.

[8] Manoha E, Herraero C. Numerical prediction of airfoil aerodynamic noise. AIAA Paper 2002-2573, 2002.

[9] Meyers MR, Kerschen EJ. Influence of incidence angle on sound generation by airfoils interacting with high-frequency gusts. J Fluid Mech 1995;292:271–304.

[10] Peake N, Kerschen EJ. Influence of mean loading on noise generated by the interaction of gusts with a flat-plate cascade: upstream radiation. J Fluid Mech 1997; 347:315–46.

[11] Howe MS. A review of the theory of trailing edge noise. J Sound Vib 1978;62:437–65.

[12] Howe MS. Trailing edge noise at low Mach number. J Sound Vib 1999;225(2):211–38.

[13] Brooks TF, Hodgson TH. Trailing edge noise prediction from measured surface pressures. J Sound Vib 1981; 78:69–117.

[14] Ffowcs Williams JE, Hall LH. Aerodynamic sound generation by turbulent flow in the vicinity of a scattering half plane. J Fluid Mech 1970;40:657–70.

[15] Tam CKW, Dong Z. Radiation and outflow boundary conditions for direct computation of acoustic and flow disturbances in a nonuniform mean flow. CEAS/AIAA Paper 95-007, 1995.

[16] Brown GL, Roshko A. On density effects and large structure in turbulent mixing layers. J Fluid Mech 1974; 64:775–816.

[17] Liepmann HW, Laufer J. Investigation of free turbulent mixing. Technical Report TN-1257, NACA, 1947.

[18] Wygnanski I, Fiedler H. Some measurements in self-preserving jet. J Fluid Mech 1969;38:577–612.

[19] Davies POAL, Fisher MJ, Barratt MJ. The characteristics of the turbulence in the mixing region of a round jet. J Fluid Mech 1963;15:337–67
Also Corrigendum, J Fluid Mech 1963;15:559.

[20] Hussain AKMF, Husain ZD. Turbulence structure in the axisymmetric free mixing layer. AIAA J 1980;18:1462–9.

[21] Bell JH, Mehta RD. Development of a two-stream mixing layer from tripped and untripped boundary layers. AIAA J 1990;28(12):2034–42.

[22] Bogey C, Bailly C, Juve D. Noise investigation of a high subsonic, moderate Reynolds number jet using a compressible large eddy simulation. Theor Comput Fluid Dyn 2003;16:273–97.

[23] Zaman KBMQ. Flow field and near and far sound field of a subsonic jet. J Sound Vib 1986;106:1–16.

[24] Lau JC, Morris PJ, Fisher MJ. Measurements in subsonic and supersonic free jets using a laser velocimeter. J Fluid Mech 1979;93:1–27.

[25] Hussein HJ, Capp SP, George WK. Velocity measurements in a high-Reynolds-number, momentum-conserving, axisymmetric, turbulent jet. J Fluid Mech 1994; 258:31–75.

[26] Lush PA. Measurements of subsonic jet noise and comparison with theory. J Fluid Mech 1971;46:477–500.

[27] Ahuja KK. Correlation and prediction of jet noise. J Sound Vib 1974;29:155–68.

[28] Tanna HK, Dean PD, Fisher MJ. The influence of temperature on shock-free supersonic jet noise. J Sound Vib 1975;39:429–60.

[29] Ffowcs Williams JE. The noise from turbulence convected at high speed. Philos Trans Soc A 1963;255:469–503.

[30] Lighthill MJ. On sound generated aerodynamically: I. General theory. Proc R Soc London A 1952;211:564–87.

[31] Lighthill MJ. On sound generated aerodynamically: II. Turbulence as a source of sound. Proc R Soc London A 1954;222:1–32.

[32] Tam CKW, Burton DE. Sound generated by instability waves of supersonic flows. Part 1. Two-dimensional mixing layers. J Fluid Mech 1984;138:249–71.

[33] Mitchell BE, Lele SK, Moin P. Direct computation of the sound from a compressible co-rotating vortex pair. J Fluid Mech 1995;285:181–202.

[34] Colonius T, Lele SK, Moin P. Sound generation in a mixing layer. J Fluid Mech 1997;330:375–409.

[35] Freund JB, Lele SK, Moin P. Direct numerical simulation of a Mach 1.92 turbulent jet and its sound field. AIAA J 2000;38(11):2023–31.

[36] Freund JB. Noise sources in a low-Reynolds-number turbulent jet at Mach 0.9. J Fluid Mech 2001;438: 277–305.

[37] Ran H, Colonius T. Numerical simulation of sound radiated by a turbulent vortex ring. AIAA Paper 2004-2918, 2004.

[38] Rowley CW, Colonius T, Basu AJ. On self-sustained oscillations in two-dimensional compressible flow over rectangular cavities. J Fluid Mech 2002;455:315–46.

[39] Lui C, Lele SK. A numerical study of broadband shock noise. AIAA Paper 2002-2530, 2002.

[40] Lui C, Lele SK. Sound generation mechanism of shock-associated noise. AIAA Paper 2003-3315, 2003.

[41] Barone MF, Lele SK. A numerical technique for trailing edge acoustic scattering problems. AIAA Paper 2002-0026, 2003.

[42] Manning T, Lele SK. Numerical investigation of sound generation in supersonic jet screech. AIAA/CEAS Paper 2000-2081, 2000.

[43] Freund JB, Lele SK, Moin P. Matching of near/far-field equation sets for direct computation of aerodynamic sound. AIAA Paper 93-4326, Long Beach, 1993.

[44] Brentner KS. Numerical algorithms for acoustic integrals with examples for rotor noise prediction. AIAA J 1997;35:625–30.

[45] Freund JB, Lele SK, Moin P. Calculation of the radiated sound field using an open Kirchhoff surface. AIAA J 1996;34(5):909–16.

[46] Ffowcs Williams JE, Hawkings DL. Sound generation by turbulence and surfaces in arbitrary motion. Proc R Soc London A 1969;264:321–42.

[47] Wang M, Lele SK, Moin P. Computation of quadrupole noise using acoustic analogy. AIAA J November 1996;34(11):2247–4344.

[48] Curle N. The influence of solid boundaries upon aerodynamic sound. Proc R Soc London A 1955;231:505–14.

[49] Oberai AA, Wang M. Computation of trailing edge noise from an incompressible flow calculation. In: Proceedings of the 2000 Summer Program. Center for Turbulence Research, Stanford University, November 2000. p. 343–52.

[50] Goldstein ME. Aeroacoustics of turbulent shear flows. Annu Rev Fluid Mech 1984;16:263–85.

[51] Goldstein ME. An exact form of Lilley's equation with a velocity quadrupole/temperature dipole source term. J Fluid Mech 2001;443:231–6.

[52] Brentner KS, Farassat F. An analytical comparison of the acoustic analogy and Kirchhoff formulations for moving surfaces. AIAA J 1998;36:1379–86.

[53] Crighton DG, Dowling AP, Ffowcs Williams JE, Heckl M, Leppington FG. Modern methods in analytical acoustics—Lecture Notes, Berlin: Springer; 1992.

[54] Lyrintzis AS. Integral methods in computational aeroacoustics. In: Proceedings of CEAS Workshop 'From CFD to CAA', Athens, Greece, 2002.

[55] Pilon AR, Lyintzis AS. Development of an improved Kirchhoff method for jet aeroacoustics. AIAA J. 1998;36(5):783–90.

[56] Lockard DP, Singer BA, Brentner KS, Lilley GM. Simulation of acoustic scattering from a trailing edge. J Sound Vib 2000;230(3):541–60.

[57] Lockard D. An efficient, two-dimensional implementation of the two-dimensional Ffowcs Williams Hawkings equation. J Sound Vib 2000;229:897–911.

[58] Brentner KS, Farassat F. Modeling aerodynamically generated sound of helicopter rotors. Progr Aerospace Sci 2003;39:83–120.

[59] Wang M, Lele SK, Moin P. Computation of quadrupole noise using acoustic analogy. AIAA J 1996;34(11):2247–54.

[60] Mitchell BE, Lele SK, Moin P. Direct computation of the sound generated by vortex pairing in an axisymmetric jet. J Fluid Mech 1999;383:113–42.

[61] Gloerfelt X, Bailly C, Juve D. Direct computation of the noise radiated by a subsonic cavity flow and application of integral methods. J Sound Vib 2003;266:119–46.

[62] Leonard A. Computing three-dimensional incompressible flows with vortex elements. Ann Rev Fluid Mech 1985;17:523–59.

[63] Cottet GH, Koumoutsakos P. Vortex methods: theory and practice. Cambridge: Cambridge University Press; 2000.

[64] Guo Y. Application of Ffowcs Williams–Hawkings equation to two dimensional problems. J Fluid Mech 2000;403:201–21.

[65] Guo Y. Prediction of flap edge noise. AIAA Paper 1999-1804, 1999.

[66] Howe MS. The theory of vortex sound. Cambridge: Cambridge University Press; 2003.

[67] Narayanan S, Noack BR, Meiburg E. Reduced-order dynamical modeling of sound generation from a jet. AIAA Paper 2002-0073, 2002.

[68] Eldredge JD, Colonius T, Leonard A. A vortex particle method for two-dimensional compressible flow. J Comput Phys 2002;179(2):371–99.

[69] Hardin JC, Pope DS. An acoustic/viscous splitting technique for computational aeroacoustics. Theor Comput Fluid Dyn 1994;6:323–40.

[70] Crow SC. Aerodynamic sound emission as a singular perturbation problem. Stud Appl Math 1970;49:355–68.

[71] Lele SK. Computational aeroacoustics—a review. AIAA paper 97-0018, 1997.

[72] Lele SK. Direct numerical simulations of compressible turbulent flows. In: Alfredsson H, Johansson A, Henningson D, Hanifi A, editors. 2nd ERCOFTAC Summer School on Transition and Turbulence Modeling, Dordrecht: Kluwer Academic Publishers; 1999. p. 421–28 [chapter 7].

[73] Shen WZ, Sorensen JN. Comment on the aeroacoustic formulation of hardin and pope. AIAA J 1999;37:141–3.

[74] Goldstein ME. A generalized acoustic analogy. J Fluid Mech 2003;488:315–33.

[75] Bogey C, Bailly C, Juve D. Computation of flow noise using source terms in linearized Euler's equation. AIAA J 2002;40:235–43.

[76] Ewert R, Meinke M, Schröder W. Comparison of source term formulations for a hybrid CFD/CAA method. AIAA Paper 2001-2200, 2001.

[77] Möhring W, Müller EA, Obermeier F. Problems in flow acoustics. Rev Mod Phys 1983;55(3):707–24.

[78] Dowling AP, Ffowcs Williams JP, Goldstein ME. Sound propagation in a moving stream. Philos Trans R Soc London A 1978;288(1353):321–49.

[79] Ewert R, Meinke M, Schröder W. Acoustic perturbation equations based on flow decomposition via source filtering. J Comput Phys 2003;188(2):365–98.

[80] Möhring W. Modeling low Mach number noise. In: Proceedings of the Symposium on the Mechanics of Sound Generation in Flows. Berlin: Springer; 1979. p. 85–96.

[81] Pierce AD. Wave equation for sound in fluids with unsteady inhomogeneous flow. J Acoust Soc Amer 1990; 111(2):2292–9.

[82] Ehrenfried K, Meyer C, Dillmann A. Simulation of sound propagation in boundary layers based on Möhring's acoustic analogy. AIAA Paper 2003-3272, 2003.

[83] Suzuki T, Lele SK. Green's functions for a source in a boundary layer: direct waves, channelled waves, & diffracted waves. J Fluid Mech 2003;477:129–73.

[84] Goldstein ME, Handler LM. The role of instability waves in predicting jet noise. AIAA Paper 2003-3256, 2003.

[85] Tam CKW, Auriault L. Jet mixing noise from fine-scale turbulence. AIAA J 1999;37(2):145–53.

[86] Meneveau C, Katz J. Scale-invariance and turbulence models for large-eddy simulation. Ann Rev Fluid Mech 2000;32:1–32.

[87] Lesieur M, Métais O. New trends in large-eddy simulation of turbulence. Ann Rev Fluid Mech 1996;28:45–82.

[88] Jimenez J, Moser RD. Large-eddy simulations: where are we and what can we expect? AIAA J 2000;38:605–12.

[89] Piomelli U, Balaras E. Wall-layer models for large-eddy simulations. Ann Rev Fluid Mech 2002;34:349–74.

[90] Moin P. Advances in large eddy simulation methodology for complex flows. Int J Heat and Fluid Flow 2002;23(5):710–20.

[91] Rogallo RS, Moin P. Numerical simulation of turbulent flows. Ann Rev Fluid Mech 1984;16:99–137.

[92] Pope SB. Turbulent flows. Cambridge: Cambridge University Press; 2000.

[93] Moin P, Squires K, Cabot W, Lee S. A dynamic subgrid-scale model for compressible turbulence and scalar transport. Phys Fluids 1991;3:2746–57.

[94] Erlebacher G, Hussaini MY, Speziale CG, Zang TA. Toward the large-eddy simulation of compressible turbulent flows. J Fluid Mech 1992;238:155–85.

[95] Vreman B, Geurts B, Kuerten H. Subgrid-modeling in les of compressible flow. Appl Sci Res 1995;54:191–203.

[96] Boersma BJ, Lele SK. Large eddy simulation of compressible turbulent jets. In: Annual Research Briefs.

Center for Turbulence Research, Stanford University, 1999. p. 365–77.

[97] Lilly DK. A proposed modification of the germano subgrid-scale closure method. Phys Fluids 1992;4:633–5.

[98] Constantenescu G, Lele SK. Large eddy simulation of a near-sonic turbulent jet and its radiated noise. AIAA Paper 2001-0376, 2001.

[99] Blaisdell GA, Spyropoulos ET, Qin JH. The effect of the formulation of nonlinear terms on aliasing errors in spectral methods. Appl Num Math 1996;21(3):207–19.

[100] Spyropoulos ET, Blaisdell GA. Evaluation of the dynamic model for simulations of compressible decaying isotropic turbulence. AIAA J 1996;34:990–8.

[101] Stanley SA, Sarkar S, Mellado JP. A study of the flow-field evolution and mixing in a planar turbulent jet using direct numerical simulation. J Fluid Mech 2002;450: 377–407.

[102] Tam CKW, Webb JC. Dispersion-relation-preserving finite-difference schemes for computational acoustics. J Comput Phys 1993;107(2):262–81.

[103] Nagarajan S, Lele SK, Ferziger JH. A robust high-order compact method for large eddy simulation. J Comput Phys 2003;191:392–419.

[104] Honein A, Moin P. Higher entropy conservation and stability of compressible turbulence simulations. J Comput Phys 2004;201(2):531–45.

[105] Mahesh K, Constantinescu G, Moin P. A numerical method for large-eddy simulation in complex geometries. J Comput Phys 2004;197(1):215–40.

[106] Chapman DR. Computational aerodynamics: development and outlook. AIAA J 1979;17:1293–313.

[107] Wang M, Moin P. Dynamic wall modeling for large-eddy simulation of complex turbulent flows. Phys Fluids 2002;14(7):2043–51.

[108] Vasilyev O, Lund T, Moin P. A general class of commutative filters for LES in complex geometries. J Comput Phys 1998;146(1):82–104.

[109] Bardina J, Ferziger JH, Reynolds WC. Improved subgrid scale models for large eddy simulation. AIAA Paper 80-1357, 1980.

[110] Stolz S, Adams NA, Kleiser L. An approximate deconvolution model for large-eddy simulation with application to incompressible wall-bounded flows. Phys Fluids 2001;13(5):997–1015.

[111] Stolz S, Adams NA, Kleiser L. The approximate deconvolution model for les of compressible flows and its application to shock-turbulent-boundary-layer interaction. Phys Fluids 2001;13(10):2985–3001.

[112] Rembold B, Kleiser L. Noise prediction from rectangular jet flow using les. AIAA Paper 2003-3281, 2003.

[113] Hinze JO. Turbulence, second ed. New York: McGraw-Hill; 1975.

[114] Kraichnan RH. The structure of isotropic turbulence at very high Reynolds numbers. J Fluid Mech 1959;5: 453–97.

[115] Saddoughi SG, Veeravalli SV. Local isotropy in turbulent boundary layers at high Reynolds number. J Fluid Mech 1994;268:333–72.

[116] Saddoughi SG. Local isotropy in complex turbulent boundary layers at high Reynolds number. J Fluid Mech 1997;348:201–45.

[117] Sreenivasan KR. On the scaling of the turbulence energy-dissipation rate. Phys Fluids 1984;27(5):1048–51.

[118] Tennekes H, Lumley JL. A first course in turbulence. Cambridge, MA: MIT Press; 1972.

[119] Bodony D, Lele SK. Jet noise prediction of cold and hot subsonic jets using large-eddy simulation. AIAA Paper 2004-3022, 2004.

[120] Witkowska A, Juvé D, Brasseur JM. Numerical study of noise from isotropic turbulence. J Comput Acoust 1997; 5:317–36.

[121] He G-W, Rubinstein R, Wang L-P. Effects of subgrid scale modeling on time correlations in large eddy simulation. Phys Fluids 2002;14:2186–93.

[122] Piomelli U, Streett C, Sarkar S. On the computation of sound by large-eddy simulations. J Eng Math 1997;32: 217–36.

[123] Bodony DJ, Lele SK. Spatial scale decomposition of shear layer turbulence and the sound sources associated with the missing scales in a large-eddy simulation. AIAA Paper 2002-2454, 2002.

[124] Seror C, Sagaut P, Bailly C, Juve D. Subgrid scale contribution to noise production in decaying isotropic turbulence. AIAA J 2000;38(10):1795–803.

[125] Seror C, Sagaut P, Bailly C, Juve D. On the radiated noise computed by large-eddy simulation. Phys Fluids 2001;13(2):476–87.

[126] Bodony DJ, Lele SK. A statistical subgrid scale noise model: formulation. AIAA Paper 2003-3252, 2003.

[127] Rubinstein R, Zhou Y. The frequency spectrum of sound radiated by isotropic turbulence. Phys Lett A 2000;267: 379–83.

[128] Rubinstein R, Zhou Y. Characterization of sound radiation by unresolved scales of motion in computational aeroacoustics. Eur J Mech B: Fluids 2002;21: 105–11.

[129] He G-W, Wang M, Lele SK. On the computation of space-time correlations by large-eddy simulation. In: Annual Research Briefs. Center for Turbulence Research, Stanford University, Stanford, CA, 2003. p. 319–30.

[130] NASA/Ohio Aerospace Institute. Computational Aeroacoustics Workshop on Benchmark Problems, Cleveland, OH, 1995, 1996, 2000, 2003.

[131] Freund JB, Lele SK, Moin P. Direct simulation of a Mach 1.92 jet and its sound field. AIAA/CEAS Paper 98-2291, 1998.

[132] Sarkar S, Hussaini MY. Computation of the sound generated by isotropic turbulence. Technical Report 93-74, ICASE, 1993.

[133] Avital EJ, Sandham ND. Box-length requirements for simulation of sound from large structures in jets. AIAA J 1997;35(5):912–5.

[134] Avital EJ, Sandham ND, Luo KH. Mach wave radiation by mixing layers. Part I: analysis of the sound field. Theor Comput Fluid Dyn 1998;12(2):73–90.

[135] Cockburn B, Karniadakis G, Shu C-W, editors. Discontinuous Galerkin methods: theory, computational, and applications. Berlin: Springer; 2000.

[136] Kopriva DA. A staggered-grid multidomain spectral method for the compressible Navier–Stokes equations. J Comput Phys 1998;143(1):125–58.

[137] Stanescu D, Habashi WG. Validation of a 3d multi-domain spectral method for fan noise prediction. AIAA/CEAS Paper 98-2266, 1998.

[138] Lin WH, Hadid A, Ascoli E, Darian A. Computations of aeroacoustic solutions by a legendre spectral element method. AIAA/CEAS Paper 99-1944, 1999.

[139] Ait-Ali Yahia D, Robichaud MP, Stanescu D, Habashi WG. Spectral element grid generation and nonlinear computations for noise radiation from aircraft engines. AIAA/CEAS Paper 98-1832, 1999.

[140] Collis SS. Multiscale methods for turbulence simulation and control. In: 32nd Computational Fluid Dynamics Lecture Series, number 034. von Karman Institute, 2002.

[141] Atkins HL, Shu CW. Quadrature-free implementation of discontinuous Galerkin method for hyperbolic equations. AIAA J 1998;36:775–82.

[142] Blom CPA, Hagmeijer R, Biesheuvel A. Three-dimensional quadrature-free discontinuous Galerkin method for computational aeroacoustics. AIAA Paper 2001-2198.

[143] Collis SS, Ghayour K. Discontinuous Galerkin methods for compressible DNS. In: Proceedings of FEDSM'03, number 45632 in FEDSM2003, Honolulu, HI, New York: ASME; 2003.

[144] Hu FQ, Hussaini MY, Rasetarinera P. An analysis of the discontinuous Galerkin method for wave propagation problems. J Comput Phys 1999;151:921–46.

[145] Knio OM, Ting L. Vortical flow outside a sphere and sound generation. SIAM J Appl Math 1997;57(4):972–81.

[146] Knio OM, Collorec L, Juve D. Numerical study of sound emission by 2D regular and chaotic vortex configurations. J Comput Phys 1995;116(2):226–46.

[147] Trefethen LN. Group velocity in finite difference schemes. SIAM Rev 1982;24(2):113–36.

[148] Vichnevetsky R. Wave propagation analysis of difference schemes for hyperbolic equations: a review. Int J Numer Meth Fluids 1987;7:409–52.

[149] Lele SK. Compact finite-difference schemes with spectral-like resolution. J Comput Phys 1992;103(1):16–42.

[150] Lui C, Lele SK. Direct numerical simulation of spatially developing, compressible, turbulent mixing layers. AIAA Paper 2001-0291, 2001.

[151] Mahesh K. A family of high order finite difference schemes with good spectral resolution. J Comput Phys 1998;145(1):332–58.

[152] Hixon R. Prefactored small-stencil compact schemes. J Comput Phys 2000;165(2):522–41.

[153] Hixon R, Turkel E. Compact implicit MacCormack-type schemes with high accuracy. J Comput Phys 2000;158(1):51–70
See also J Comput Phys 163(2):547.

[154] Zhuang M, Chen RE. Optimized upwind dispersion-relation-preserving finite difference scheme for computational aeroacoustics. AIAA J 1998;36(11):2146–8.

[155] Ghosal S. An analysis of numerical errors in large-eddy simulations of turbulence. J Comput Phys 1996;125(1):187–206.

[156] Vichnevetsky R. Propagation through numerical mesh refinement for hyperbolic equations. Math Comput Simulation 1981;23:344–53.

[157] Vichnevetsky R, Pariser EC. High order numerical Sommerfeld boundary conditions: theory and experiments. Comput Math Appl 1985;11:67–78.

[158] Vichnevetsky R. Invariance theorems concerning reflection at numerical boundaries. J Comput Phys 1986;63:268–82.

[159] Tam CKW, Webb JC, Dong Z. A study of the short wave components in computational acoustics. J Comput Acoust 1993;1(1):1–30.

[160] Vichnevetsky R. Numerical filtering for partial differential equations. Technical Report NAM 156, Rutgers University, 1974.

[161] Alpert P. Implicit filtering in conjunction with explicit filtering. J Comput Phys 1981;44:212–9.

[162] Visbal MR, Gaitonde DV. High-order accurate methods for unsteady vortical flows on curvilinear meshes. AIAA Paper 98-0131, 1998.

[163] Gaitonde DV, Visbal MR. Further development of a Navier–Stokes solution procedure based on higher-order formulas. AIAA Paper 99-0557, 1999.

[164] Carpenter MH, Gottlieb D, Abarbanel S. The stability of numerical boundary treatments for compact high-order finite-difference schemes. J Comput Phys 1993;108(2):272–95.

[165] Gustafsson B, Kreiss H-O, Sundström A. Stability theory of difference approximations for mixed initial boundary-value problems. 2. Math Comput 1972;26(119):649.

[166] Carpenter MH, Gottlieb D, Abarbanel S. Time-stable boundary-conditions for finite-difference schemes solving hyperbolic systems-methodology and application to high-order compact schemes. J Comput Phys 1994;111(2):220–36.

[167] Abarbanel SS, Chertock AE. Strict stability of high-order compact implicit finite-difference schemes: the role of boundary conditions for hyperbolic PDEs, I. J Comput Phys 2000;160(1):42–66.

[168] Abarbanel SS, Chertock AE, Yefet A. Strict stability of high-order compact implicit finite-difference schemes: the role of boundary conditions for hyperbolic PDEs, II. J Comput Phys 2000;160(1):67–87.

[169] Carpenter MH, Nordström J, Gottlieb D. A stable and conservative interface treatment of arbitrary spatial accuracy. J Comput Phys 1999;148:341–65.

[170] Nordström J, Carpenter MH. Boundary and interface conditions for high-order finite-difference methods applied to the Euler and Navier–Stokes equations. J Comput Phys 1999;148:621–45.

[171] Nordström J, Carpenter MH. High-order finite-difference methods multidimensional linear problems, and curvilinear coordinates. J Comput Phys 2001;173:149–74.

[172] Hagstrom T. Experiments with stable high-order difference approximations to hyperbolic initial-boundary value problems. In: Bermudez A, Gomez D, Hazard C, Joly P, Roberts J, editors. Proceedings of the Fifth International Conference on Mathematical and Numerical Aspects of Wave Propagation Phenomena. Philadelphia: SIAM; 2000.

[173] Alpert B. Hybrid Gauss–trapezoidal rules. SIAM J Sci Comput 1999;20:1551–84.

[174] Zingg DW. Comparison of high-accuracy finite-difference methods for linear wave propagation. SIAM J Sci Comput 2000;22(2):476–502.

[175] Fletcher CAJ. Computational techniques for fluid dynamics, vol. 2, second ed. Berlin: Springer; 1991.

[176] Steger JL. Implicit finite-difference simulation of flow about arbitrary two-dimensional geometries. AIAA J 1978;16(7):679–86.

[177] Pulliam TH, Steger JL. Implicit finite-difference simulations of three-dimensional compressible flow. AIAA J 1980;18(2):159–67.

[178] Hindman RG. Generalized coordinate forms of governing fluid equations and associated geometrically induced errors. AIAA J 1982;20(10):1359–67.

[179] Thomas PD, Lombard CK. Geometric conservation law and its application to flow computations on moving grids. AIAA J 1979;17(10):1030–7.

[180] Lighthill J. Waves in fluids. Cambridge: Cambridge University Press; 1978.

[181] Wall C, Pierce CD, Moin P. A semi-implicit method for resolution of acoustic waves in low Mach number flows. J Comput Phys 2002;181(2):545–63.

[182] Collis SS, Lele SK. A computational investigation of receptivity in high-speed flow near a swept leading edge. Technical Report TF-71, Department of Mechanical Engineering, Stanford University, 1997.

[183] Moin P, Mahesh K. Direct numerical simulation: a tool in turbulence research. Annual Rev Fluid Mech 1998;30:539–78.

[184] Hairer E, Wanner G. Solving ordinary differential equations I, rev ed. Berlin: Springer; 1996.

[185] Zingg DW, Lomax H, Jurgens HM. Optimized finite-difference schemes for wave propagation. AIAA Paper 93-0459, 1993.

[186] Hu FQ, Hussaini MY, Manthey J. Low-dissipation and low-dispersion Runge–Kutta schemes for computational acoustics. J Comput Phys 1996;124:177–91.

[187] Carpenter MH, Kennedy CA. A fourth-order 2N-storage Runge–Kutta scheme. Technical Report TM109112, NASA, 1994.

[188] Stanescu D, Habashi WG. 2N-storage Runge–Kutta schemes for acoustics. J Comput Phys 1998;143:674–81.

[189] Givoli D. Non-reflecting boundary conditions. J Comput Phys 1991;94:1–29.

[190] Tsynkov SV. Numerical solution of problems on unbounded domains. Appl Numer Math 1998;27(4):465–532.

[191] Hagstrom T. Radiation boundary conditions for the numerical simulation of waves. Acta Numerica 1999;8:47–106.

[192] Colonius T. Modeling artificial boundary conditions for compressible flow. Ann Rev Fluid Mech 2004;36:315–45.

[193] Tam CKW. Advances in numerical boundary conditions for computational aeroacoustics. AIAA Paper 97-1774, 1997.

[194] Colonius T, Lele SK, Moin P. Boundary conditions for direct computation of aerodynamic sound generation. AIAA J 1993;31(9):1574–82.

[195] Engquist B, Majda A. Absorbing boundary conditions for the numerical simulation of waves. Math Comput 1977;31(139):629–51.

[196] Engquist B, Majda A. Radiation boundary conditions for acoustic and elastic wave calculations. Comm Pure Appl Math 1979;32:313–57.

[197] Giles MB. Nonreflecting boundary-conditions for Euler equation calculations. AIAA J 1990;28(12):2050–8.

[198] Tsynkov S, Abarbanel S, Nordström J, Ryaben'kii V, Vatsa V. Global artificial boundary conditions for computation of external flows with jets. AIAA J 2000;38(11):2014–22.

[199] Sofronov IL. Non-reflecting inflow and outflow in a wind tunnel for transonic time-accurate simulation. J Math Anal Appl 1998;221:92–115.

[200] Trefethen LN, Halpern L. Well-posedness of one-way wave equations and absorbing boundary conditions. Math Comput 1986;47(176):421–35.

[201] Rowley CW, Colonius T. Discretely nonreflecting boundary conditions for linear hyperbolic systems. J Comput Phys 2000;157(2):500–38.

[202] Hagstrom T, Goodrich J. Accurate radiation boundary conditions for the linearized Euler equations in Cartesian domains. SIAM J Sci Comput 2002;24(3):770–95.

[203] Bayliss A, Turkel E. Radiation boundary conditions for wave-like equations. Commun Pure Appl Math 1980;33(6):707–25.

[204] Bayliss A, Turkel E. Far field boundary conditions for compressible flows. J Comput Phys 1982;48(2):182–99.

[205] Hagstrom T, Hariharan SI. High-order radiation boundary conditions for the convective wave equation in exterior domains. SIAM J Sci Comput 2003;25(3):1088–101.

[206] Tam CKW, Dong Z. Radiation and outflow boundary conditions for direct computation of acoustic and flow disturbances in a nonuniform mean flow. J Comput Acoust 1996;4(2):175–201.

[207] Berenger JP. A perfectly matched layer for the absorption of electromagnetic waves. J Comput Phys 1994;114(2):185–200.

[208] Hu FQ. On absorbing boundary conditions for linearized Euler equations by a perfectly matched layer. J Comput Phys 1996;129(1):201–19.

[209] Abarbanel S, Gottlieb D, Hesthaven JS. Well-posed perfectly matched layers for advective acoustics. J Comput Phys 1999;154(2):266–83.

[210] Tam CKW. Advances in numerical boundary conditions for computational aeroacoustics. AIAA Paper 97-1774, 1997.

[211] Abarbanel S, Gottlieb D. A mathematical analysis of the PML method. J Comput Phys 1997;134(2):357–63.

[212] Hu FQ. A stable, perfectly matched layer for linearized Euler equations in unsplit physical variables. J Comput Phys 2001;173:455–80.

[213] Hagstrom T. New results on absorbing layers and radiation boundary conditions. In: Ainsworth M, Duncan D, Davies P, Martin P, Rynne B, editors. Topics in computational wave propagation. Berlin: Springer; 2003. p. 1–42.

[214] Hagstrom T, Nazarov I. Absorbing layers and radiation boundary conditions for jet flow simulations. AIAA Paper 2002-2606, 2002.

[215] Hagstrom T, Nazarov I. Solutions of category 1 problems using high-order difference methods and perfectly

matched layers. In: Proceedings of the 4th Computational Aeroacoustics Workshop on Benchmark Problems. NASA CP-2004-212954, September 2004, p. 355–70.

[216] Hixon R, Shih S-H, Mankbadi R. Evaluation of boundary conditions for computational aeroacoustics. AIAA J 1995;33(11):2006–12.

[217] Colonius T. Numerically nonreflecting boundary and interface conditions for compressible flow and aeroacoustic computations. AIAA J 1997;35(7):1126–33.

[218] Tam CKW, Dong Z. Wall boundary conditions for high-order finite-difference schemes in computational aeroacoustics. Theor Comput Fluid Dyn 1996;6(5–6): 303–22.

[219] Colonius T, Ran H. A super-grid-scale model for simulating compressible flow on unbounded domains. J Comput Phys 2002;182(1):191–212.

[220] Hedstrom GW. Nonreflecting boundary conditions for nonlinear hyperbolic systems. J Comput Phys 1979;30: 222–37.

[221] Thompson KW. Time dependent boundary conditions for hyperbolic systems. J Comput Phys 1987;68:1–24.

[222] Thompson KW. Time dependent boundary conditions for hyperbolic systems ii. J Comput Phys 1990;89(2): 439–61.

[223] Poinsot T, Lele SK. Boundary conditions for direct simulation of compressible viscous flows. J Comput Phys 1992;101:104–29.

[224] Colonius T, Lele SK, Moin P. The scattering of sound waves by a vortex-numerical simulations and analytical solutions. J Fluid Mech 1994;260:271–98.

[225] Rudy DH, Strikwerda JC. A nonreflecting outflow boundary condition for subsonic Navier–Stokes calculations. J Comput Phys 1980;36:55–70.

[226] Strikwerda JC. Initial boundary value problems for incompletely parabolic systems. Comm Pure Appl Math 1977;30:797–822.

[227] Oliger J, Sundström A. Theoretical and practical aspects of some initial boundary-value problems in fluid-dynamics. SIAM J Appl Math 1978;35(3):419–46.

[228] Dutt P. Stable boundary conditions and difference schemes for Navier–Stokes equations. SIAM J Numer Anal 1988;25(2):245–67.

[229] Nordström J. The use of characteristic boundary-conditions for the Navier–Stokes equations. Comput Fluids 1995;24(5):609–23.

[230] Papanastasiou TC, Malamataris N, Ellwood K. A new outflow boundary condition. Int J Numer Meth Fluids 1992;14:587–608.

[231] Nordström J. Accurate solutions of the Navier–Stokes equations despite unknown outflow boundary data. J Comput Phys 1995;120:184–205.

[232] Renardy M. Imposing 'no' boundary condition at outflow: why does it work? Int J Numer Meth Fluids 1997;24:413–7.

[233] Nordström J. On flux-extrapolation at supersonic outflow boundaries. Appl Numer Math 1999;30(4):447–57.

[234] Israeli M, Orszag SA. Approximation of radiation boundary conditions. J Comput Phys 1981;41:115–35.

[235] Freund JB. Proposed inflow/outflow boundary condition for direct computation of aerodynamic sound. AIAA J 1997;35(4):740–2.

[236] Ta'asan S, Nark DM. An absorbing buffer zone technique for acoustic wave propagation. AIAA Paper 95-0146, 1995.

[237] Karni S. Far-field filtering operators for suppression of reflections from artificial boundaries. SIAM J Numer Anal 1996;33(3):1014–47.

[238] Rai M, Moin P. Direct simulations of turbulent flow using finite-difference schemes. J Comput Phys 1991;96: 15–53.

[239] Spalart PR. Direct numerical study of leading edge contamination. In: Fluid dynamics of three-dimensional turbulent shear flows and transition, vol. AGARD-CP-438, 1988. p. 5.1–5.13.

[240] Nordström J, Nordin N, Henningson D. The fringe region technique and the Fourier method used in the direct numerical simulation of spatially evolving viscous flows. SIAM J Sci Comput 1999;20(4):1365–93.

[241] Guo Y, Adams NA, Kleiser L. Direct numerical simulation of transition in a spatially growing compressible boundary layer using a new Fourier method. In: Voke PR, Kleiser L, Chollet J-P, editors. Direct and large–Eddy simulation, vol. I, Dordrecht: Kluwer Academic Publishers; 1994. p. 249–59.

[242] Schlatter P, Adams NA, Kleiser L. Periodic boundary treatment for non-periodic flow geometries. J Comput Phys, 2003; submitted for publication.

[243] Leonard A. Energy cascade in large-Eddy simulations of turbulent fluid flows. Adv Geophys 1974;18:237.

[244] Leonard A, Winckelmans GS. A tensor-diffusivity subgrid model for large-Eddy simulation. In: Voke PR, Sandham ND, Kleiser L, editors. Direct and large–Eddy simulation III. Dordrecht: Kluwer; 1999. p. 147–62.

[245] Colonius T. Accuracy of supergrid boundary conditions for incident disturbances with a range of incidence angles in uniform and sheared flows. In: Proceedings of the 4th Computational Aeroacoustics Workshop on Benchmark Problems, NASA CP, October 2003. in press.

[246] Kim JW, Lee DJ. Generalized characteristic boundary conditions for computational aeroacoustics. AIAA J 2000;38(11):2040–9.

[247] Kim JW, Lee DJ. Generalized characteristic boundary conditions for computational aeroacoustics. Part 2. AIAA J 2004;42(1):47–55.

[248] Tam CKW, Dong Z. Wall boundary-conditions for high-order finite-difference schemes in computational aeroacoustics. Theor Comput Fluid Dyn 1994;6(5–6): 303–22.

[249] Hixon R. Curvilinear wall boundary conditions for computational aeroacoustics. AIAA Paper 99-2395, 1999.

[250] Barone MF, Lele SK. Receptivity of the compressible mixing layer. J Fluid Mech 2004; submitted for publication.

[251] Kurbatskii KA, Tam CKW. Cartesian boundary treatment of curved walls for high-order computational aeroacoustics schemes. AIAA J 1997;35(1):133–40.

[252] Chung C, Morris PJ. Acoustic scattering from two- and three-dimensional bodies. J Comput Acoustics 1998;6(3): 357–75.

[253] Laik OA, Morris PJ. Direct simulation of acoustic scattering by two- and three-dimensional bodies. J Aircraft 2000;37(1):68–75.

[254] Mahesh K, Lee SS, Lele SK, Moin P. The interaction of an isotropic field of acoustic waves with a shock-wave. J Fluid Mech 1995;300:383–407.

[255] Harten A, Osher S. Uniformly high-order accurate nonoscillatory schemes. 1. SIAM J Numer Anal 1987; 24(2):279–309.

[256] Harten A, Engquist B, Osher S, Chakravarthy SR. Uniformly high order accurate essentially non-oscillatory schemes. 3. J Comput Phys 1987;71:231–75.

[257] Shu CW, Osher S. Efficient implementation of essentially non-oscillatory shock-capturing schemes. J Comput Phys 1988;77(2):439–71.

[258] Shu CW, Osher S. Efficient implementation of essentially non-oscillatory shock-capturing schemes. 2. J Comput Phys 1989;83(1):32–78.

[259] Liu XD, Osher S, Chan T. Weighted essentially nonoscillatory schemes. J Comput Phys 1994;115(1): 200–12.

[260] Jiang GS, Shu CW. Efficient implementation of weighted eno schemes. J Comput Phys 1996;126(1):202–28.

[261] Balsara DS, Shu CW. Monotonicity preserving weighted essentially non-oscillatory with increasingly high order of accuracy. J Comput Phys 2000;160(2):405–52.

[262] Pirozzoli S. Conservative hybrid compact-weno schemes for shock-turbulence interaction. J Comput Phys 2002; 178(1):81–117.

[263] Deng XG, Maekawa H. Compact high-order accurate nonlinear schemes. J Comput Phys 1997;130(1):77–91.

[264] Deng XG, Zhang HX. Developing high-order weighted compact nonlinear schemes. J Comput Phys 2000;165(1): 22–44.

[265] Weirs VG, Candler GV. Optimization of weighted ENO schemes for DNS of compressible turbulence. AIAA Paper 97-1940, 1997.

[266] Wang ZJ, Chen RF. Optimized weighted essentially non-oscillatory schemes for computational aeroacoustics. AIAA Paper 2001-1101, 2001.

[267] Lee SS, Lele SK, Moin P. Direct numerical simulation of isotropic turbulence interacting with a weak shock wave. J Fluid Mech 1993;251:533–62.

[268] Adams NA, Shariff K. A high-resolution hybrid compact-eno scheme for shock-turbulence interaction problems. J Comput Phys 1996;127(1):27–51.

[269] Inoue O, Hattori Y, Sasaki T. Sound generation by coaxial collision of two vortex rings. J Fluid Mech 2000;424:327–65.

[270] Minota T, Kambe T. Observation of acoustic emission from head-on collision of two vortex rings. J Sound Vib 1986;111:51–9.

[271] Tang SK, Ko NWM. Sound sources in the interactions of two inviscid two-dimensional vortex pairs. J Fluid Mech 2000;419:177–201.

[272] Inoue O, Hattori Y. Sound generation by shock-vortex interactions. J Fluid Mech 1999;380:81–116.

[273] Meadows KR, Kumar A, Hussaini MY. Computational study on the interaction between a vortex and a shock wave. AIAA J 1991;29:174–9.

[274] Ellzey JL, Henneke MR, Picone JM, Oran ES. The interaction of a shock with a vortex: shock distortion and the production of acoustic waves. Phys Fluids 1995; 7:172–84.

[275] Meadows KR, Caughey DA. The role of shock motion and deformation in the generation of shock noise. AIAA Paper 96-1777, 1996.

[276] Grasso F, Pirozzoli S. Shock-wave-vortex interactions: shock and vortex deformations and sound production. Theor Comput Fluid Dyn 2000;13(6):421–56.

[277] Lee S, Lele SK, Moin P. Direct numerical simulation of isotropic turbulence interacting with a weak shock wave. J Fluid Mech 1993;251:533–62.

[278] Lele SK. Shock jump relations in a turbulent flow. Phys Fluids 1992;4(12):2900–5.

[279] Zank GP, Zhou Y, Matthaeus WH, Rice WKM. The interaction of turbulence with shock waves: a basic model. Phys Fluids 2002;14(11):3766–74.

[280] Grasso F, Pirozzoli S. Simulations and analysis of the coupling process of compressible vortex pairs: free evolution and shock induced coupling. Phys Fluids 2001;13(5):1343–66.

[281] Ribner HS. Cylindrical sound wave generated by shock-vortex interaction. AIAA J 1985;23:1708–15.

[282] Inoue O, Takahashi Y. Successive generation of sounds by shock-strong vortex interaction. Phys Fluids 2000;12(12):3229–34.

[283] Ding Z, Hussaini MY, Erlebacher G. Computational study of shock interaction with a vortex ring. Phys Fluids 2001;13(10):3033–48.

[284] Kevlahan NK-R. The propagation of weak shocks in non-uniform flows. J Fluid Mech 1996;327:161–97.

[285] Kevlahan NK-R. The vorticity jump across a shock in a non-uniform flow. J Fluid Mech 1997;341:371–84.

[286] Ribner HS. Shock-turbulence interaction and the generation of noise. Technical Report Rep. 1233, NACA, 1955. NACA Rep. 1233; see also NACA 3255 (1954).

[287] Moore FK. Unsteady oblique interaction of a shock wave with plane disturbances. Technical Report TN 2879, NACA, 1954. Also as NACA Report 1165.

[288] Lee S, Lele SK, Moin P. Interaction of isotropic turbulence with shock waves: effect of shock strength. J Fluid Mech 1997;340:225–47.

[289] Mahesh K, Lele SK, Moin P. The influence of entropy fluctuations on the interaction of turbulence with a shock wave. J Fluid Mech 1997;334:353–79.

[290] Lilley GM. Jet noise: classical theory and experiments. In: Hubbard H, editor. Aeroacoustics of flight vehicles. NASA RP 1258, 1991.

[291] Tam CKW. Jet noise generated by large-scale coherent motion. In: Hubbard H, editor. Aeroacoustics of flight vehicles. NASA RP-1258, August 1991.

[292] Goldstein ME. Noise from turbulent shear flows. In: Hubbard H, editor. Aeroacoustics of flight vehicles. NASA RP 1258, 1991.

[293] NASA. Proceedings of the Jet Noise Workshop, number 2001-211152 in CP, November 2001.

[294] Farge M. Wavelet transforms and their applications to turbulence. Ann Rev Fluid Mech 1992;24:395–457.

[295] Holmes P, Lumley JL, Berkooz G. Turbulence. Turbulence, coherent structures, dynamical systems and symmetry. Cambridge: Cambridge University Press; 1996.

[296] Freund JB, Colonius T. POD analysis of sound generation by a turbulent jet. AIAA Paper 2002-0072, 2002.

[297] Citriniti JH, George WK. Reconstruction of the global velocity field in the axisymmetric mixing layer utilizing the proper orthogonal decomposition. J Fluid Mech 2000;418:137–66.

[298] Arndt REA, Long DF, Glauser MN. The proper orthogonal decomposition of pressure fluctuations surrounding a turbulent jet. J Fluid Mech 1997;340:1–33.

[299] Gordeyev SV, Thomas FO. Coherent structure in the turbulent planar jet. Part 1. Extraction of proper orthogonal decomposition eigenmodes and their self-similarity. J Fluid Mech 2000;414:145–94.

[300] Liu JTC. Developing large-scale wavelike eddies and the near jet noise field. J Fluid Mech 1974;62(3):437–64.

[301] Michalke A, Fuchs HV. On turbulence and noise of an axisymmetric shear flow. J Fluid Mech 1975;70:179–205.

[302] Bradshaw P, Ferriss DH, Johnson RF. Turbulence in the noise-producing region of a circular jet. J Fluid Mech 1964;591–624.

[303] Panchapakesan NR, Lumley JL. Turbulence measurements in axisymmetric jets of air and helium. Part 1. Air jets. J Fluid Mech 1993;246:197–223.

[304] Plaschko P. Stochastic-model theory for coherent turbulent structures in circular jets. Phys Fluids 1981;24:187–93.

[305] Plaschko P. Axial coherence functions of circular turbulent jets based on an inviscid calculation of damped modes. Phys Fluids 1983;26:2368–72.

[306] Tam CKW, Chen KC. A statistical model of turbulence in two-dimensional mixing layers. J Fluid Mech 1979;92:303–26.

[307] Tam CKW. Stochastic model theory of broadband shock associated noise from supersonic jets. J Sound Vib 1987;116:265–302.

[308] Morris PJ, Giridharan MG, Lilley GM. On the turbulent mixing of compressible free shear layers. Proc R Soc London A 1990;431:219–43.

[309] Lighthill MJ. Sound generated aerodynamically. Proc R Soc London A 1962;267:147–82.

[310] Lighthill MJ. Jet noise. AIAA J 1963;1:1507–17.

[311] Lilley GM. On the noise from jets. Technical Report CP-131, AGARD, 1974.

[312] Goldstein ME. Aeroacoustics. New York: McGraw-Hill Book Co.; 1976.

[313] Bailly C, Lafon P, Candel S. Subsonic and supersonic jet noise predictions from statistical source models. AIAA J 1997;35(11):1688–96.

[314] Khavaran A. Role of anisotropy in turbulent mixing noise. AIAA J 1999;37(7):832–41.

[315] Morris PJ, Farrasat F. Acoustic analogy and alternative theories of jet noise prediction. AIAA J 2002;40:671–80.

[316] Gaster M, Kit E, Wygnanski I. Large-scale structures in a forced turbulent mixing layer. J Fluid Mech 1985;150:23–39.

[317] Crighton DG, Gaster M. Stability of slowly diverging jet flow. J Fluid Mech 1976;88(2):397–413.

[318] Tam CKW, Morris PJ. The radiation of sound by the instability waves of a compressible plane turbulent shear layer. J Fluid Mech 1980;98:349–81.

[319] Crighton DG, Huerre P. Shear-layer pressure fluctuations and superdirective acoustic sources. J Fluid Mech 1990;220:355–68.

[320] Mankbadi R, Liu JTC. A study of the interactions between large-scale coherent structures and fine-grained turbulence in a round jet. Philos Trans R Soc A 1981;298(1443):541–602.

[321] Tam CKW, Morris PJ. Tone excited jets v: a theoretical model and comparison with experiment. J Sound Vib 1985;102:119–51.

[322] Morris PJ, Long LN, Scheidegger TE, Wang Q, Pilon AR. High-speed jet noise simulations. AIAA Paper 98-2290, 1998.

[323] Yen C, Messersmith N. Need title. AIAA Paper 99-1859, 1999.

[324] Bretolotti F, Colonius T. On the noise generated by shear-layer instabilities in turbulent jets. AIAA Paper 2003-1062, 2003.

[325] Day M, Reynolds WC, Mansour N. Nonlinear stability and structure of compressible reacting mixing layers. J Fluid Mech 2001;446:375–408.

[326] Cheung LC, Lele SK. Acoustic radiation from subsonic and supersonic mixing layers with nonlinear pse. AIAA Paper 2004-0363, 2004.

[327] Mohseni K, Colonius T, Freund JB. An evaluation of linear instability waves as sources of sound in a supersonic turbulent jet. Phys Fluids 2002;14(10):3593–600.

[328] Tam CKW, Golebiowski M, Seiner JM. On the two components of turbulent mixing noise from supersonic jets. AIAA Paper 96-1716, 1996.

[329] Tam CKW. Jet noise: since 1952. Theor Comput Fluid Dyn 1998;10(4):393–405.

[330] Lele SK. Noise radiation from high-speed jets: some insights from numerical simulations. In: Friedrich R, Métais O, editors. Proceedings of the DLES-5 Conference. Munich, Germany, Dordrecht: Kluwer Academic Publishers; 2003.

[331] Bogey C, Bailly C, Juvé D. Computation of the sound radiated by a 3-D jet using large eddy simulation. AIAA Paper 2000-2009, 2000.

[332] Zhao W, Frankel S, Mongeau L. Large eddy simulation of sound radiation from a subsonic turbulent jet. 6th AIAA/CEAS Aeroacoustics Conference, Lahaina, AIAA Paper 2000-2078, 2000.

[333] Powell A. On edge tones and associated phenomena. Acustica 1953;3:233–43.

[334] Powell A. Advances in understanding supersonic jet screech: review and perspective. Progr Aerospace Sci 1998;34:45–106.

[335] M. Harper-Bourne, MJ. Fisher. The noise from shock waves in supersonic jets. Technical Report CP 131, AGARD, 1974.

[336] Tam CKW, Tanna HK. Shock associated noise of supersonic jets from convergent-divergent nozzles. J Sound Vib 1982;81:337–58.

[337] Norum TD, Seiner JM. Measurements of mean static pressure and far-field acoustics of shock-containing supersonic jets. Technical Report TM 84521, NASA, 1982.

[338] Tam CKW. Broadband shock-associated noise of moderately imperfectly expanded supersonic jets. J Sound Vib 1990;140:55–71.

[339] Tam CKW. Broadband shock associated noise from supersonic jets measured by a ground observer. AIAA J 1992;30:2395–401.

[340] Lui C, Lele SK. A numerical investigation of broadband shock noise. AIAA Paper 2002-0074, 2002.

[341] Freund JB, Lele SK. Computer simulation and prediction of jet noise. In: Raman G, Mclaughlin D, Morris P, editors. High speed jet flows. London: Taylor & Francis; 2003.

[342] Seiner JM. Advances in high speed jet aeroacoustics. AIAA Paper 84-2275, 1984.

[343] Freund JB. Noise-source turbulence statistics and the noise from a Mach 0.9 jet. Phys Fluids 2003;15(6): 1788–99.

[344] Stromberg JL, McLaughlin DK, Troutt TR. Flow field and acoustic properties of a Mach number 0.9 jet at a low Reynolds number. J Sound Vib 1980;72(2): 159–76.

[345] Laufer J, Yen T-C. Noise generation by a low-Mach-number jet. J Fluid Mech 1983;134:1–31.

[346] Crow SC. Acoustic gain of a turbulent jet. Paper IE6, Meeting of the American Physical Society, Division of Fluid Dynamics, Colorado, 1972.

[347] Fuchs HV, Michalke A. Turbulence and noise of an axisymmetric shear-flow. J Fluid Mech 1975;70: 179–205.

[348] Freund JB, Bodony DJ, Lele SK. Turbulence interactions leading to far-field jet noise. In: Proceedings of the 2002 Summer Program, Center for Turbulence Research, Stanford University, December 2002. p. 15–26.

[349] Constantinescu G, Lele SK. A highly accurate technique for the treatment of flow equations at the polar axis in cylindrical coordinates using series expansions. J Comput Phys 2002;183:165–86.

[350] Bogey C, Bailly C. Direct computation of the sound radiated by a high-Reynolds number, subsonic jet. In: Proceedings of CEAS Workshop 'From CFD to CAA', November 2002, Athens, Greece, 2002.

[351] Bodony DJ, Lele SK. Large Eddy simulation of turbulent jets and progress towards a subgrid scale turbulence model. In: International Workshop on LES for Acoustics, 2002. DGLR-Report-2002-03, October 7–8, 2002, Göttingen, Germany, DLR Göttingen, Göttingen, Germany, 2002. p. 1–9.

[352] Bodony DJ, Lele SK. Applications and results: jet noise. In: Wagner C, Hüttl T, Sagaut P, editors. LES for acoustics. Cambridge: Cambridge University Press; 2004.

[353] Bogey C, Bailly C, Juvé D. Numerical simulation of sound generated by vortex pairing in a mixing layer. AIAA J 2000;38(12):2210–8.

[354] Bridges J, Hussain F. Direct evaluation of aeroacoustic theory in a jet. J Fluid Mech 1992;240:469–501.

[355] Mitchell BE, Lele SK, Moin P. Direct computation of Mach wave radiation in an axisymmetric supersonic jet. AIAA J 1997;35(10):1574–80.

[356] Mankbadi R, Hixon R, Shih SH, Povinelli LA. Use of linearized Euler equations for supersonic jet noise prediction. AIAA J 1998;36(2):140–7.

[357] Tam CKW, Chen P, Seiner JM. Relationship between instability waves and noise of high-speed jets. AIAA J 1992;30:1747–52.

[358] Seiner JM, Bhat TRS, Ponton MK. Mach wave emission from a high-temperature supersonic jet. AIAA J 1994; 32:2345–50.

[359] Troutt TR, McLaughlin DK. Experiments on the flow and acoustic properties of a moderate-Reynolds-number supersonic jet. J Fluid Mech 1982;116:123–56.

[360] Barone MF, Lele SK. Application of adjoint solutions to the receptivity problem in compressible mixing layers. AIAA Paper 2003-3219, 2003.

[361] Shen H, Tam CKW. Numerical simulation of the generation of axisymmetric mode jet screech tones. AIAA J 1998;36(10):1801–9.

[362] Thies AT, Tam CKW. Computation of turbulent axisymmetric and nonaxisymmetric jet flows using the k-epsilon model. AIAA J 1996;34(2):309–16.

[363] Zhang X, Edwards JA. Computational analysis of unsteady cavity flows driven by thick shear layers. The Aeronautical J 1988;94(940):355–64.

[364] Zhang X, Rona A, Edwards JA. The effect of trailing edge geometry on cavity flow oscillation driven by a supersonic shear layer. The Aeronautical J 1998; 129–36.

[365] Shen H, Tam CKW. Three-dimensional numerical simulation of the jet screech phenomenon. AIAA J 2002; 40(1):33–41.

[366] Walker S, Thomas FO. Experiments characterizing non-linear shear layer dynamics in a supersonic rectangular jet undergoing screech. Phys Fluids 1997;9:2562–79.

[367] Manning T, Lele SK. Numerical simulation of shock-vortex interaction in supersonic jet screech. AIAA/CEAS Paper 98-0282, 1998.

[368] Stuart JT. On finite amplitude oscillations in laminar mixing layers. J Fluid Mech 1967;29:417–40.

[369] Suzuki T, Lele SK. Shock leakage through an unsteady vortex-laden mixing layer: application to jet screech. J Fluid Mech 2003;490:139–67.

[370] Alkislar MB, Krothapalli A, Lourenco LM. Structure of a screeching rectangular jet: a stereoscopic particle image velocimetry study. J Fluid Mech 2003;489:121–54.

[371] Lele SK. A reformulation of shock-cell noise sources. Phys Fluids 2003; submitted for publication.

[372] Kerschen EJ, Cain A. Modeling supersonic jet screech. Part 2. Acoustic radiation from the shock-vortex inter-action. AIAA Paper 95-0507, 1995. AIAA Aerospace Sciences Meeting, Reno.

[373] Kopiev VF, Chernyshev SA. Vortex ring eigen-oscillations as a source of sound. J Fluid Mech 1997;341:19–57.

[374] Zaitsev MY, Kopiev VF, Kotova AN. Representation of the sound field of a turbulent vortex ring as a super-position of quadrupoles. Acoustical Phys 2001;47(6): 793–801.

[375] Widnall SE, Tsai CY. The instability of the thin vortex rings. Philos Trans R Soc London A 1977;287:273–305.

[376] Glezer A, Coles D. An experimental study of a turbulent vortex ring. J Fluid Mech 1990;211:243–83.

[377] Zaitsev MY, Kopiev VF, Munin AG, Potokin AA. Sound radiation by a turbulent vortex ring. Sov Phys Dolk 1990;35:488–9.

[378] Shaw L. Active control for cavity acoustics. AIAA Paper 98-2347, 1998.

[379] Shaw L, Northcraft S. Closed loop active control for cavity acoustics. AIAA Paper 99-1902, 1999.

[380] Rockwell D, Naudascher E. Review-self-sustaining oscil-lations of flow past cavities. J Fluids Eng 1978;100: 152–65.

[381] Colonius T. An overview of simulation, modeling, and active control of flow/acoustic resonance in open cavities. AIAA Paper 2001-0076, 2001.

[382] Powell A. On the edgetone. J Acoust Soc Amer 1961;33(4):395–409.

[383] Krishnamurty K. Sound radiation from surface cutouts in high speed flow. PhD thesis, California Institute of Technology, 1956.

[384] Rossiter JE. Wind-tunnel experiments on the flow over rectangular cavities at subsonic and transonic speeds. Aeronautical Research Council Reports and Memoranda, No. 3438, October 1964.

[385] Tam CKW, Block PJW. On the tones and pressure oscillations induced by flow over rectangular cavities. J Fluid Mech 1978;89(2):373–99.

[386] Cattafesta III, LN, Garg S, Choudhari M, Li F. Active control of flow-induced cavity resonance. AIAA Paper 97-1804, June 1997.

[387] Williams DR, Fabris D. Experiments on controlling multiple acoustic modes in cavities. AIAA Paper 2000-1903, 2000.

[388] Hankey WL, Shang JS. Analysis of pressure oscillation in an open cavity. AIAA J 1980;18(8):892–8.

[389] Fuglsang DF, Cain AB. Evaluation of shear layer cavity resonance mechanisms by numerical simulation. AIAA Paper 92-0555, 1992.

[390] Shieh CM, Morris PJ. Parallel computational aeroacoustic simulation of turbulent subsonic cavity flow. AIAA Paper 2000-1914, 2000.

[391] Henderson J, Badcock K, Richards BE. Subsonic and transonic transitional cavity flows. AIAA Paper 2000-1966, 2000.

[392] Cain A, Rubio AD, Bortz DM, Banks HT, Smith RC. Optimizing control of open bay acoustics. AIAA Paper 2000-1928, 2000.

[393] Shih SH, Hamed A, Yeuan JJ. Unsteady supersonic cavity flow simulations using coupled $k - \varepsilon$ and Navier–Stokes equations. AIAA J 1994;32(10):2015–21.

[394] Lamp AM, Chokani N. Computation of cavity flows with suppression using jet blowing. J Aircraft 1997;34(4):545–51.

[395] Sinha N, Arunajatesan S, Ukeiley LS. High fidelity simulation of weapons bay aeroacoustics and active flow control. AIAA Paper 2000-1968, 2000.

[396] Rona A, Dieudonne W. A flow-resonant model of transonic laminar open cavity instability. AIAA Paper 2000-1967, 2000.

[397] Chokani N. Prediction of hypersonic cavity flow dynamics. AIAA Paper 99-0171, 1999.

[398] Squires KD, Forsythe JR, Morton SA, Strang WZ, Wurtzler KE, Tomaro RF, Grismer MJ, Spalart PR. Progress on detached-eddy simulation of massively separated flows. AIAA Paper 2002-1021, 2002.

[399] Shieh CM, Morris PJ. Comparison of two- and three-dimensional turbulent cavity flows. AIAA Paper 2001-0511, 2001.

[400] Smith BR, Jordan JR, Bender EE, Rizk SN, Shaw LL. Computational simulation of active control of cavity acoustics. AIAA Paper 200-1927, 2000.

[401] Shaw L. High speed application of active flow control for cavity acoustics. AIAA Paper 2000-1926, 2000.

[402] Rizzetta DP, Visbal MR. Large-eddy simulation of supersonic cavity flowfields including flow control. AIAA Paper 2002-2853, 2002.

[403] Larchevêque L, Sagaut P, Mary I, Labbe O, Comte P. Large-eddy simulation of a compressible flow past a deep cavity. Phys Fluids 2003;15(1):193–210.

[404] Forestier N, Jacquin L, Geffroy P. The mixing layer over a deep cavity at high-subsonic speed. J Fluid Mech 2003;475:101–45.

[405] Lenormand E, Sagaut P, Phuoc LT, Comte P. Subgrid-scale models for large-eddy simulations of compressible wall bounded flows. AIAA J 2000;38(8):1340–50.

[406] Boris JP, Grinstein FF, Oran ES, Kolbe RL. New insights into large eddy simulations. Fluid Dynamics Res 1992;10(4–6):199–228.

[407] Colonius T, Basu AJ, Rowley CW. Numerical investigation of the flow past a cavity. AIAA Paper 99-1912, 1999.

[408] Shieh CM, Morris PJ. Parallel numerical simulation of subsonic cavity noise. AIAA Paper 99-1891, 1999.

[409] Gharib M, Roshko A. The effect of flow oscillations on cavity drag. J Fluid Mech 1987;177:501–30.

[410] Najm HN, Ghoniem AF. Numerical simulation of the convective instability in a dump combustor. AIAA J 1991;29(6):911–9.

[411] Lighthill J. Report on the final panel discussion, In: Proceedings of ICASE-NASA Langley workshop on Computational Aeroacoustics, 1993.

[412] Wei M, Freund JB. Noise control using adjoint-based optimization. 8th AIAA/CEAS Aeroacoustics Conference, Breckenridge, CO, AIAA Paper 2002-2524, June 2002.

[413] Wei M, Freund JB. A quiet free shear flow. J Fluid Mech; 2004, submitted for publication.

[414] Marsden AL, Wang M, Dennis Jr JE, Moin P. Suppression of vortex-shedding noise via derivative-free shape optimization. Phys Fluids 2004;16(10):83–6.

[415] Choi S, Alonso JJ, Van der Weide E. Numerical and mesh resolution requirements for accurate sonic boom prediction of complete aircraft configurations. AIAA Paper 2004-1060, 2004.

[416] Tanna HK. Experimental study of jet noise. 1. Turbulent mixing noise. J Sound Vib 1977;50(3):405–28.

[417] Mollo-Christensen E, Kolpin MA, Martucelli JR. Experiments on jet flows and jet noise far-field spectra and directivity patterns. J Fluid Mech 1964;18:285–301.